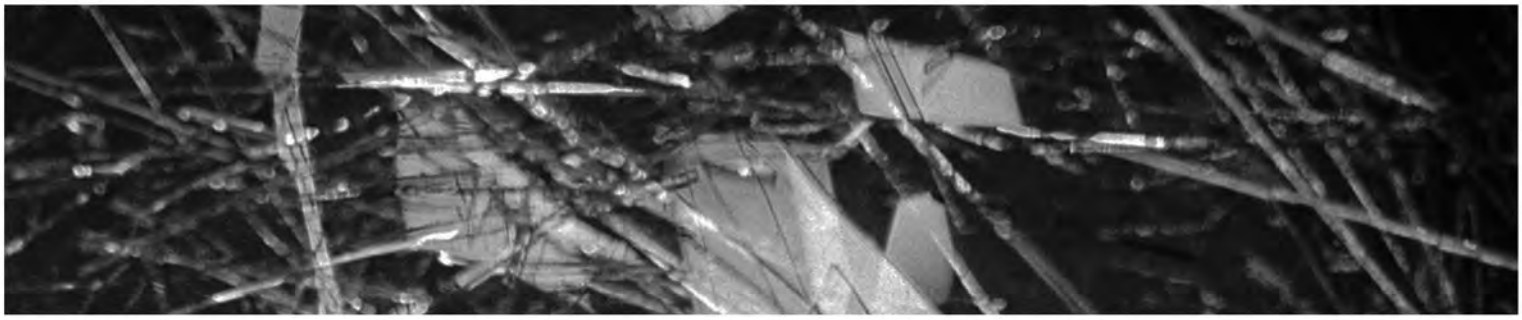

Investigations on the Cold Bending Behaviour of a Cold-Bent Double Glazing Unit with a Rigid Edge-Spacer Frame

Tim van Driel

October 2021

Delft University of Technology
Faculty of Civil Engineering and Geosciences

TU Delft abt AGC SI-X FIBERLINE BUILDING PROFILES

Investigations on the Cold Bending Behaviour of a Cold-Bent Double Glazing Unit with a Rigid Edge-Spacer Frame

by

T.C. van Driel

to obtain the degree of

Master of Science
in Civil Engineering, track Building Engineering

at the Delft University of Technology,
to be defended publicly on Friday October 22nd, 2021.

Student number:	4319672	
Thesis committee:	Prof.ir. M. Overend,	TU Delft
	Ir. C. Noteboom,	TU Delft
	Ir. E. ten Brincke,	ABT
	Dr.ir F.P. van der Meer	TU Delft

Contact Information

Student

Name:	Tim van Driel
Student no.:	4319672
Faculty:	Civil Engineering and Geosciences
Track:	Building Engineering
Specialisation:	Structural Design

Graduation Committee

Name:	Prof.ir. Mauro Overend (chairman)
Organisation:	Delft University of Technology
Faculty:	Architecture and the Built Environment
Section:	Department of Architectural Engineering + Technology

Name:	Ir. Chris Noteboom (daily supervisor)
Organisation:	Delft University of Technology
Faculty:	Civil Engineering and Geosciences
Section:	Applied Mechanics

Name:	Ir. Erwin ten Brincke
Organisation:	ABT

Name:	Dr.ir. Frans van der Meer
Organisation:	Delft University of Technology
Faculty:	Civil Engineering and Geosciences
Section:	Applied Mechanics

Preface

This thesis report is the result of my graduation research about cold bending glass. It is intended as the final requirement for graduating from the Master of Science in Civil Engineering (Building Engineering track) at Delft University of Technology. Doing this research has been an interesting experience that was rich in lessons, partly because it has taken place during the global COVID-19 pandemic. Doing almost everything from home has been a challenge, but the overall process has taught me a lot. Several people have played a key role in completing my thesis, so I would like to take a moment to thank them.

My graduation committee has been instrumental to my progress, so therefore I would like to thank Mauro Overend, Erwin ten Brincke, Frans van der Meer and Chris Noteboom. Thank all of you for your enthusiasm about the project, your insightful comments and questions, and the interesting discussions during our meetings.

In particular I want to thank Mauro Overend for acting as the chair of the committee. This research is the continuation of your larger project that started back in Cambridge. I am grateful for the opportunity to work on this amazing and interesting topic, and I hope future research can build on my work.

I also want to express my special gratitude to Chris Noteboom. Thank you for your guidance, and for always being open to questions, comments and meetings, the latter sometimes on short notice or in the evening. I enjoyed our talks and discussions greatly, and your critical questions, suggestions, out-of-the-box ideas and insights were immensely helpful in making progress.

Outside of the committee, there have also been people and organisations that were important in the research.

Thank you to Marco Zaccaria and AGC. The glass that you provided for the experiments elevated the research to the next level, and it would not have been the same without you. Thank you for your generosity, and I hope my findings can be of use to you.

Wout Hoogendoorn of Si-X. Thank you for providing the space, labour and materials required to assemble the panels. Without you it would not have been possible to fabricate them as designed, and compromises would have to be made. Your contribution was invaluable, which I greatly appreciate.

Tage Frank Namnuad Jensen and Fiberline. You provided the GFRP profiles that were an integral part of the design of the panels. Thank you for making this research possible.

Peter de Vries, Louis den Breejen and Giorgos Stamoulis. Thank you for having me as a guest in the Stevinlab. Thank you Peter for creating some space in the busy lab, and for helping me at several points during the process of testing. Thank you Louis and Giorgos, not only for your contributions in the design and execution of the experiments, but also for being good company, making the tests even more fun than they already were.

Lastly, I want to thank several individuals who have supported me throughout my thesis.

Charlotte, for always being my main support. You were there to brainstorm when I was stuck, to give tips about writing, to accommodate me in tough times, and to celebrate my victories. Thank you for always being there for me.

My parents, for their never-ending enthusiasm, interest, and trust. I am lucky to have such amazing and supportive parents.

My friends and family, for their support, as well as their companionship. Goda, José, Kostas, Luc, Nicolas and everyone else, you have made my time in Delft an experience to never forget.

Tim van Driel
Leiden, October 7, 2021

Abstract

Free-form façades with bent glass have become increasingly popular in recent times. As bent glass is stiffer against out-of-plane loads, it can result in thinner glass and lower embodied carbon. A promising new technique is to cold bend thin glass plates with a stiff structural edge into a hyperbolic paraboloid (hypar), and to subsequently lock the corners to create a self-contained, self-stressed system. In this research, the physical bending process of IGUs with a particular local instability phenomenon is investigated. This instability is hypothesised to be delayed by stiffening the edges of the plate, which is done here by using 30×30 mm GFRP profiles as spacers. These were bonded to the glass using Dow 993 silicone adhesive. Four IGUs of 1.5×1.5 m were produced, three with 4 mm fully toughened glass, and one with 1.1 mm chemically toughened glass. In a series of experiments, the panels were supported on two opposite corners, and pulled down on the others.

A numerical model was developed to predict the outcome of the experiments, as well as the behaviour of the panel under wind load, though the latter was not verified with experiments. In this finite element model, the glass plates were modelled as 2D flat shell elements. The spacers were also modelled with these elements, by using them as the walls of the square hollow profile. The silicone joints were modelled as 3D solids, using the Mooney-Rivlin material model. These parameters were tested by successfully modelling a similar panel that was tested at the University of Cambridge.

In both the model and the experiments, it was found that with the sizes used it was difficult or impossible to get close to a hypar. Due to the small thickness of the glass, one of the diagonals would always be straight or mostly straight throughout the loading process, making the panel not resemble a hypar. The bottom plate of the 4 mm panels broke at a corner displacement of around 150 mm and a total load of 2.6 kN, and the top plate around 200 mm and 0.7 kN. The bottom plate of the 1.1 mm also broke first, at a corner displacement of 120mm and a total load of 1.4 kN. The top plate broke at a much higher corner displacement of almost 400mm, when the loaded diagonal was fully straight. This resulted in the top plate breaking into long, thin rods of over a meter long. It was also found that the top and bottom plates would make contact around 50 mm corner displacement in the 4 mm panels, and around 30 mm corner displacement in the 1.1 mm panel. The numerical model could predict this contact and the overall behaviour of the panel until a corner displacement of 60 mm. From the experiments and the model it was concluded that the glass was too thin for the size of the panels and the applied edge stiffening. Changing the parameters (e.g. thin glass in smaller sizes or higher edge stiffness) could result in a viable product.

Contents

1

Introduction

The popularity of glass as a construction material is evident. In many large cities there are multitudes of buildings with a glass exterior. Museums, apartment complexes, train stations or office buildings, glass covered buildings are everywhere. The early twentieth century saw the rise of this trend (Leslie, 2008), when more and more architects started to realise the potential of glass for its transparency. Initially, architectural glass was mostly flat, helped by the invention of the Pilkington process for float glass (Pilkington, 1969). With the invention of new technologies and techniques, such as the possibility to temper bent glass, and the increasing possibilities of using computers in the engineering process, the use of bent glass in buildings became more popular during the latter part of the twentieth century.

Bent glass has some advantageous properties. The most noticeable to the general public is the ability to accentuate shapes with reflections. The use of sweeping curves and rounded shapes is seen as futuristic, such as the design shown in Figure 1.1. Another advantage is that by bending the glass, it gains in stiffness against out-of-plane loads. When the façade is loaded, membrane forces are activated in the glass, which causes it to deflect less. Therefore, the glass and/or the substructure can be designed to be lighter.

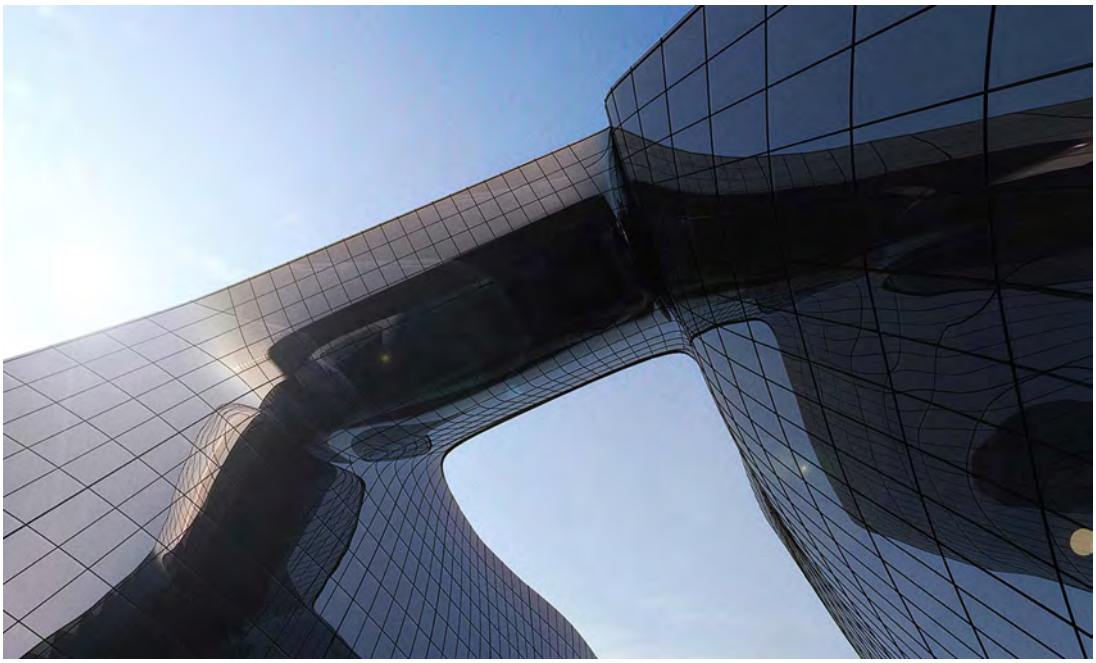

Figure 1.1: *Bent glass in the façade of The Opus by Zaha Hadid (Image taken from https://emag.archiexpo.com/dubai-zaha-hadids-opus-reworks-glass-facades/, accessed on 02-09-2021)*

Glass can be bent in several different ways. The most intuitive way is to heat up the glass until it softens, and then shape it using a mould. This process is called hot bending. The problem with hot bending is that it requires a lot of energy. It also by definition requires a mould, which increases the cost, especially when they have to be custom-made for a project. The alternative is cold bending. This does not require a mould, nor does it require heating, but it does mean the glass has to be properly secured to a substructure in order to keep its bent shape. Less

extreme curvatures can be achieved through curved bending, but when small bending radii are not desired, cold bending often preferred, as it is more cost effective than hot bending (Quaglini, 2020).

With the recent demand for glass touch screens for electronic devices such as smartphones and tablets, the technology for creating thin (< 2.1 mm), strong, scratch-resistant glass has quickly developed. As yet, there are no real architectural uses for these types of glass. Because they are so thin, they are very flexible and thus impractical for use in buildings. However, we may be able to use this to our advantage. Because of their flexibility, they may be attractive to use for cold bending. If this thin glass could be shaped with a small radius of curvature, not only would it be more interesting and impressive to look at, it would also result in a very lightweight structure, which helps in reducing the environmental impact.

A possibility would be to twist a sheet of thin glass into a hyperbolic paraboloid, or hypar. This double-curved type of surface is not only more interesting to look at, but also interesting topic of research, as it comes with some challenges. When bending a thin plate into a hypar, a local instability phenomenon occurs where one of the diagonals wants to 'buckle' and straighten. To combat this issue, a possible solution has been proposed by Galuppi (2014): by stiffening the edges of the plate, the buckling can be delayed, so the glass can be twisted further, achieving a more extreme curvature. This was tested by Young (2019) at the University of Cambridge. This research aims to build on their findings by creating a cold-bent insulated glazing unit with thin glass and stiffened edges, which can be seen in Figure 1.2.

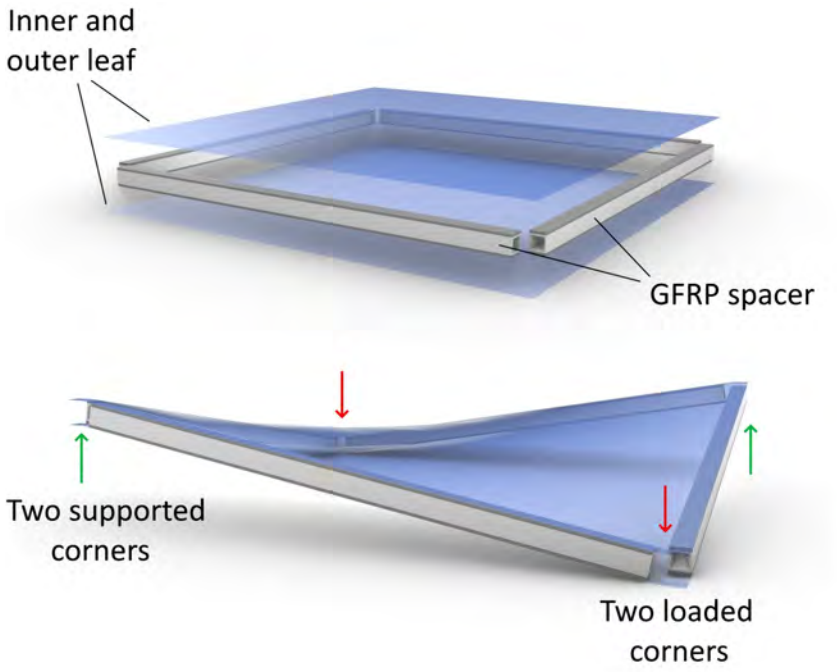

Figure 1.2: *3D visualisation of the panel that is researched in this thesis.*

1.1 Research outline

In this section, the research is given shape. First, the objectives are discussed. Then, research questions are formulated to help achieve the objectives. The relevance of the subject is discussed next, before ending with an explanation of the report structure.

1.1.1 Objectives

The main objective of the research is to improve the understanding of thin cold bent glass reinforced with stiff edges. More specifically, this research aims at trying to predict how an insulated glazing unit with stiff edge-spacers behaves when it is cold-twisted. This objective is formulated into a main research question, along with sub-questions to answer the main question. The main research question is as follows:

How can the structural behaviour of a cold-twisted insulated glazing unit with a rigid frame be predicted?

With the following sub-questions, stated in no particular order:

1. What materials (spacer, adhesive, glass type) should be used for the panel?
2. What aspects should be considered when making a finite element model of the panel?
3. How can we verify the predictions made?
4. How does the panel behave during the shaping process?
5. How does the panel behave under external load?
6. What are the parameters that need to be considered to achieve the desired cold-twisted shape?

1.1.2 Methodology

The methodology of how to answer the research question is discussed here. First, a literature study is performed, then the panels are simulated using numerical models, and finally experiments are done to validate the models.

Literature review

The first step in understanding the behaviour of the panel is performing a literature study. Part of this study is creating an overview of the studies that directly preceded this research, i.e. Fedoseeva (2017) and Young (2019). This will uncover some of the challenges that have come up before in similar projects. The next step is to dive into other forms of literature about cold bent glass, adhesives, IGUs and finite element modelling. The focus will be on the bent glass and adhesives, since their behaviour can be complex, and it is of great importance to understand their behaviour in order to have a solid foundation for the numerical model.

Numerical modelling

As mentioned before, one of the main goals of the research is to find the limits and design parameters of this specific type of IGU. One can go about this two ways. The first option is the empirical way: performing many experiments and taking the conclusion in the experimental outcomes. However, this method is very time-consuming and expensive. The second option is to use numerical models. Finite element modelling, if used correctly, can very accurately describe

the structural behaviour of a building product. This method is perhaps no less time-consuming, but it requires much less resources, changes can be made more easily and later in the process, and it's possible to explore more options. For these reasons, a numerical model will be used.

Experiments

A numerical model by itself does not guarantee that the results are correct. Therefore, the outcome of the model(s) must be validated somehow. A series of physical experiments will be conducted, the design of which will be based off of what is modelled in the previous part. The results will then be compared directly with the results of the numerical model(s) to determine their accuracy.

1.1.3 Relevance

This thesis aims to expand the knowledge about cold-bent glass. This way of creating façades is being used extensively in modern architecture around the world, but knowledge gaps still exist, especially when it comes to the hypar shape. With additional knowledge, it may become a viable addition to the toolbox of structural design.

Reducing environmental impact is becoming more and more important as time goes on, in every aspect of our lives. The aim of reducing material use and structural weight through the use of thinner glass is therefore an interesting and relevant path to take.

Finally, thin, chemically toughened glass has manifested itself in society through electronic devices. New techniques are always increasing the strength of this type of glass, yet there is no real way of using it in a structural building application. This thesis has the aim of bridging some of the knowledge gaps prevent this.

1.2 Report structure

The report of this thesis is structured according to the methodology.

- Chapter 1: Introduction
- Chapter 2: Literature study
- Chapter 3: Finite element modelling
- Chapter 4: Experiments
- Chapter 5: Discussion
- Chapter 6: Conclusions and recommendations

2

Literature study

In this literature study, we will take a look at the available literature that is relevant for the topic of this research. First we will find out more about the direct predecessor in this topic, in order to build on their work. Then, there will be a section about thin glass and how it's made. Then, the cold twisting of glass plates is explored. This is followed by a short section about thermal insulation, because this is an important aspect of a façade element. Finally, because it will become important later, we have a look at how to model silicone adhesives.

2.1 Previous work

At the University of Cambridge, Fedoseeva (2017) and Young (2019) have done initial development of a GFRP frame to bend flat glass panels with. The idea being that thin plates suffer from sensitivity to buckling when bent into an anticlastic shape (Datsiou, 2014), and a stiff frame around the edges could possibly help prevent buckling, or at least delay it to achieve larger deformations prior to buckling (Galuppi, 2014). To achieve this, a square glass plate is bonded to a rigid GFRP frame with articulated joints at the corners. It was then tested by placing it on supports at one diagonal, and applying a downward out-of-plane load at the other diagonal. In this way, the glass panel is deformed into an anticlastic shape, such as in Figure 2.1.

Some research has already been gone into developing the frame by Fedoseeva (2017) and Young (2019) in the form of finding the right adhesive and limited testing of the frame. Their findings are elaborated in the following paragraphs.

2.1.1 Adhesives

The research by Fedoseeva (2017) was mostly about finding the right adhesive to use for the joining of the glass to the frame. Three adhesives from three different manufacturers were considered, all with greatly differing strength and stiffness. The three adhesives considered were 3M Scotch-Weld Epoxy Adhesive DP490, KÖMMERLING Körapox EP 40619 & EP 42091, and SikaForce 7666 (from now on: DP490, Körapox, and SikaForce, respectively). Through tensile dumbbell tests (Figure 2.2), in compliance with BS EN ISO 527-1 (1996) and BS EN ISO 527-2 (1996), their basic stiffness properties were determined (Table 2.1).

It must be said that the Poisson's ratio results of Körapox and SikaForce were deemed incorrect, and were thus omitted. The value for DP490 in Table 2.1 was taken from Nhamoinesu (2015), the

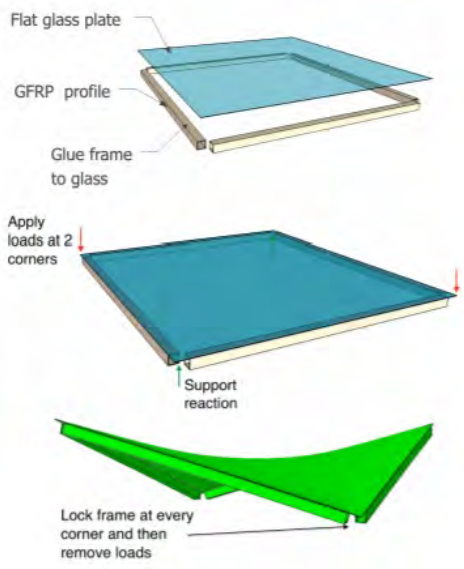

Figure 2.1: *An overview of the idea of the frame, image from Fedoseeva (2017)*

value for Körapox was assumed to be equal to that of DP490, and the value for SikaForce was likely taken from the manufacturers specifications.

Adhesive bulk properties	**DP490**	**Körapox**	**SikaForce**
ν	0.38	0.38	0.45
$E_{adh,bulk}$ **[MPa]**	1427	298	286
$G_{adh,bulk}$ **[MPa]**	517	108	98.6

Table 2.1: *The results of the tensile dumbbell tests done by Fedoseeva (2017).*

In addition to the dumbbell tests, a second set of tests was performed in the form of a double-lap shear test (Figure 2.3), with the aim of determining the shear stiffness and adhesion strength in shear. One specimen was tested for each adhesive, loaded until failure. It was found that DP490 was the strongest, with a failure load of 19.9 kN, but had a brittle failure of one of the glass plates. Körapox was the second strongest with a failure load of 7.3 kN, and failed partly due to peeling, and partly due to cracking in the adhesive. SikaForce proved the least strong, failing at 2.30 kN due to the adhesive peeling from the glass. Based on this test, it seems that DP490 and Körapox have the more favourable failure modes. However, it was mentioned in the report that the mixing was possibly not done thoroughly, so this may have influenced the results.

Figure 2.2: *The set-up of the tensile dumbbell test. Image from Fedoseeva (2017)*

Figure 2.3: *The set-up of the double-lap shear test. Image from Fedoseeva (2017).*

Finally, a creep test was also done, but not finished. The main point to be taken from the creep test is that the Körapox failed after about a week. However, this was most likely not because it is a bad adhesive, but due to other factors such as poor mixing of the adhesive or insufficient cleaning of the glass surfaces. A conclusion that Fedoseeva (2017) draws from the tests is that there should have been more of them, i.e. at least three specimens for each adhesive.

2.1.2 Numerical model - basics

In addition to analysing and testing different adhesives, Fedoseeva (2017) did numerical finite element analyses (FEA) of the frame and glass, as did Young (2019). A 3D-model was made in the FEA program Abaqus and both linear and non-linear analyses were performed.

Fedoseeva (2017) placed a 1m x 1m glass plate of 5mm thick on supports at one diagonal, and applied a displacement of 150mm at the other diagonal. To get an insight into the buckling behaviour of the plate, different support conditions were imposed. Three different support conditions were applied at the opposite corners: fixed-fixed, pin-pin, and pin-roller. The fixed-fixed support condition was modelled with both a linear analysis and a non-linear analysis, the rest were done using non-linear analysis. The results can be seen in Figure 2.4.

Initially, it may seem strange that the pin-roller supports show stiffer behaviour than the pin-pin and fixed-fixed supports. However, this can be explained by looking at Figure 2.5. According to Fedoseeva (2017), the shape that is presented in Figure 2.5 is representative for the behaviour during the entire loading process. This implies that the plate buckles almost instantly when using fixed-fixed or pin-pin supports, taking on a single-curved shape instead of the desired anticlastic shape.

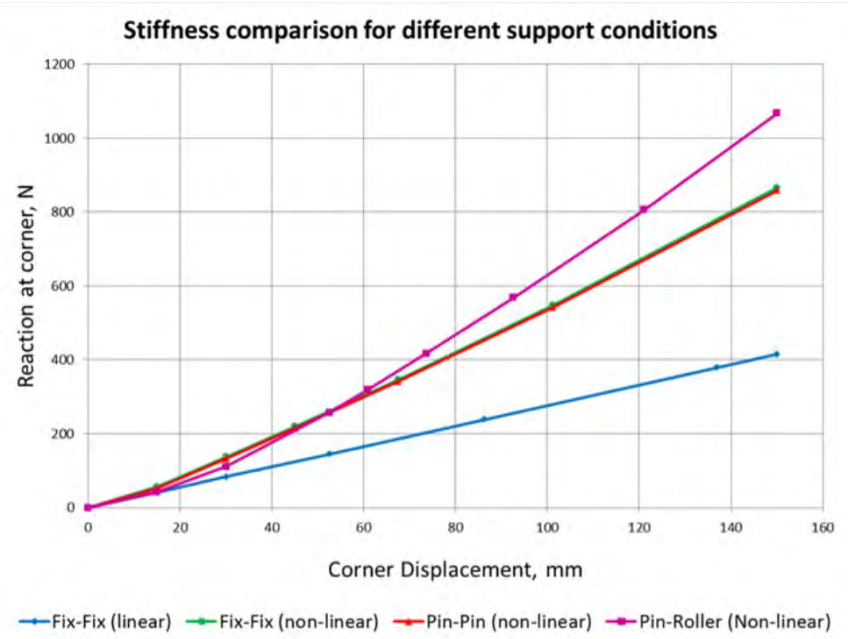

Figure 2.4: *The corner displacement versus support reaction for the finite element model of the glass plate using different support conditions. Image from Fedoseeva (2017)*

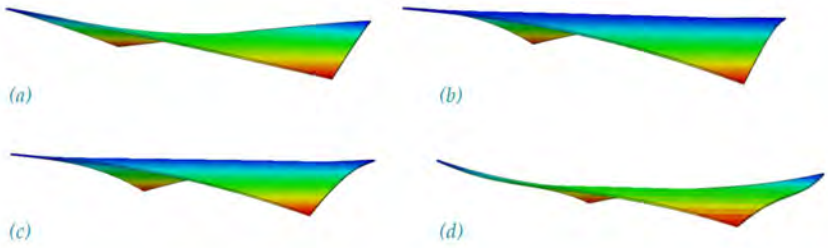

Figure 2.5: *The plate shape at maximum deflection (150mm) of the finite element model of the glass plate loaded in torsion. (a) fixed-fixed supports, linear analysis; (b) fixed-fixed supports, non-linear analysis; (c) pin-pin supports, non-linear analysis; (d) pin-roller supports, non-linear analysis. Image from Fedoseeva (2017).*

2.1.3 Numerical model - GFRP frame and glass panel

The glass used in the experimental prototypes was ultra thin Gorilla glass with dimensions 1×1 m and 1.5 mm thick. The GFRP tubes had a square hollow cross-section of 30×30 mm with 2 mm thick walls. These dimensions were used to model the frame using FEA. Pin-roller supports were used to achieve the anticlastic shape.

Fedoseeva (2017) found that at fairly low deformations, a snap-through deformation occurred, where the supported diagonal straightened. It was not possible to form a symmetric double-curved surface at large deformations. However, it was possible to create something approaching

a single curve.

Additionally, Young (2019) found that the buckling behaviour was different for the different support conditions. The plate with pin-roller supports straightens on the loaded diagonal, while the plates supported otherwise straighten on the supported diagonal. It was also found that the self weight of the glass panel was a major factor in the buckling, in that it determined the direction in which the panel would buckle.

A full sandwich panel, with two glass panes, one on either side of the GFRP frame, was also modelled. A major disadvantage to this type of sandwich panel is that the middle of the panels move towards each other (Figure 2.6. This means that at quite low corner deflections the panels touch. Exactly when they touch depends on the thickness of the glass and the type of adhesive used. In the FEA done by Young (2019) the panels started touching from 25mm corner deflection for some adhesives. Unfortunately, this is an inherent problem with the geometry of the sandwich panels. Despite this, it may still be worth investigating solutions for this problem, as the sandwich panel is significantly stiffer than a single panel on a frame, as can be seen in Figure 2.7.

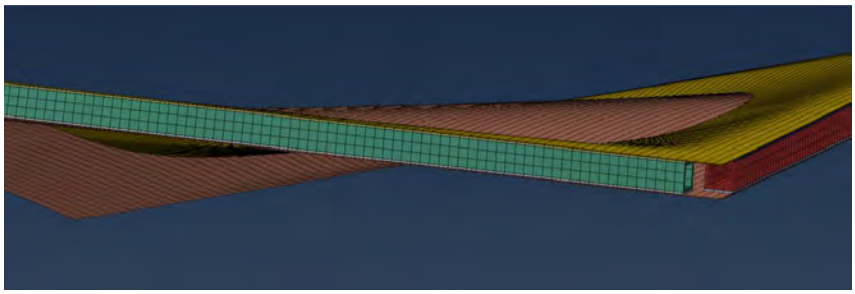

Figure 2.6: *At relatively low deformations, the glass panels touch in the middle. Image from Young (2019)*

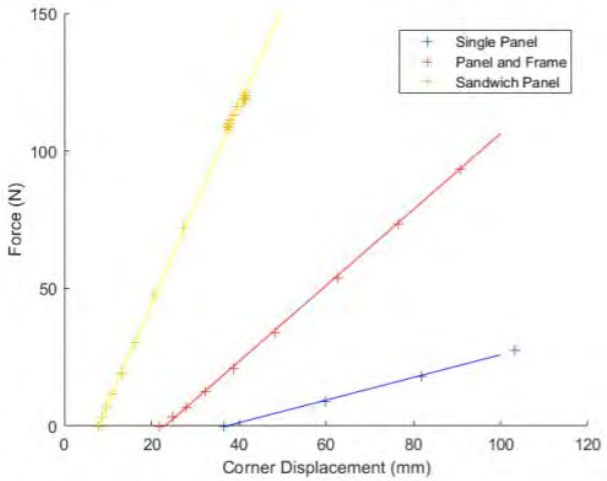

Figure 2.7: *Stiffness comparison of the single glass panel, the panel attached to the frame and the sandwich panel. Image from Young (2019)*

2.1.4 Testing

Young (2019) performed three separate tests on the GFRP frame with a single glass panel, using the set-up shown in Figure 2.9. One of the panels was made with Körapox and the other two with another adhesive, DOWSIL 795 (D795 from now on). D795 has a much lower stiffness than Körapox, so in theory would develop less stress in the adhesive at the cost of overall stiffness

of the panel. Körapox was applied in a layer of 2 mm thickness, using ball bearings as spacers. D795 was applied in a thicker layer of 5 mm to compensate for the lower stiffness, with 3D-printed spacers.

In the tests, multiple wire gauge transducers were placed on the panel to measure vertical displacement. The layout of the transducers is shown in Figure 2.8.

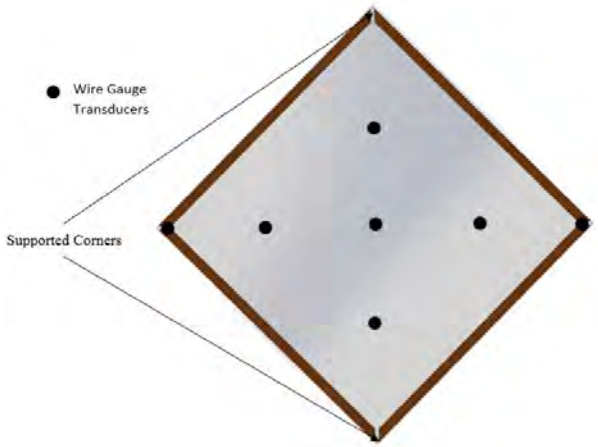

Figure 2.8: *The layout of transducers to measure vertical displacements on the panel during the test. Five transducers are placed on the panel, and one transducer is placed on each loaded corner. Image from Young (2019)*

Two of the tests lead to meaningful results. The first test (using Körapox) resulted in the adhesive peeling from the glass at a displacement of 60 mm. The peeling occurred at a position where the stress levels were not expected to cause this type of failure. This was likely due to poor mixing.

The second panel (using D795) did not lead to meaningful results due to the panel falling from the test setup and breaking. The third panel was also made with D795, and multiple tests were carried out with this panel, leading to usable data. A comparison of the experimental and numerical data of the panels from Young (2019) can be seen in Figure 2.10. The displacements (horizontal axis) do not start at the origin due to the self-weight of the panel and the measuring equipment.

Figure 2.9: *The experimental set-up used by Young (2019).*

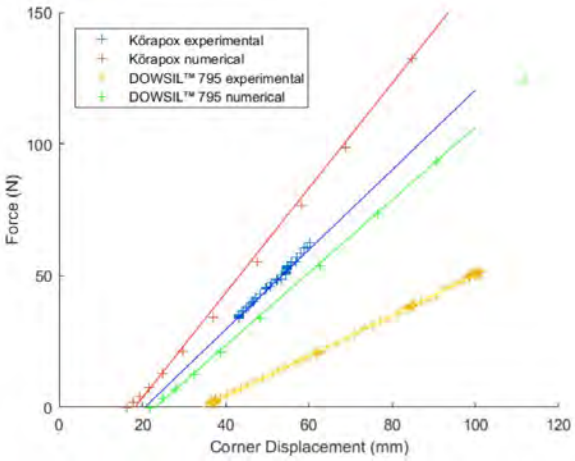

Figure 2.10: *Comparison of the numerical and experimental results of Körapox and D795. Image from Young (2019)*

2.2 Thin glass

In regular architectural applications, the thinner end of the standard glass range, i.e. 2-4 mm, are generally only used as sacrificial layers in laminated glass. These sacrificial layers are used on the outside of the glass to absorb an impact to the glass, in order to protect the thicker structural glass on the inside. This thin glass is typically the standard soda lime silica glass that is used throughout the building industry.

2.2.1 Creation and thermally toughening

The normal way of creating sheets of glass is through the standard float glass process (schematic overview in Figure 2.12). In short, the glass is heated to above its transformation temperature and placed on a molten tin bath. The tin has a high surface tension, ensuring that the glass becomes very flat. More can be read about this process in Pilkington (1969). After it has been formed on the tin bath, the glass can be annealed, heat strengthened or fully toughened by cooling it down in different ways. The highest bending strength can be achieved by fully (thermally) toughening the glass. In this process, the glass is rapidly cooled right after it has been formed, leaving residual compressive stresses in the outer parts of the glass, and tensile stresses on the inside (Pfaender (1996), Figure 2.11). The residual compressive stress acts as pre-stress when the glass is bent, and counteracts tensile stresses that result from bending. The use of toughened glass is especially beneficial for thinner glass sheets, as they are more flexible, and thus reach their ultimate strength through lower loads than thicker glass.

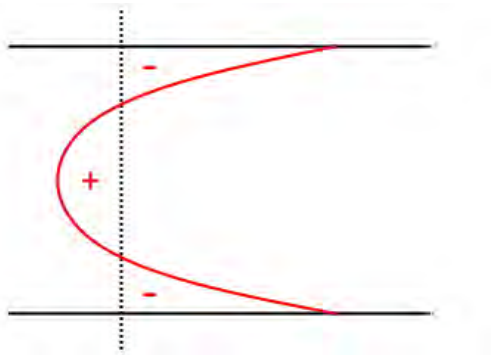

Figure 2.11: *Schematic representation of the stress profile inside a fully toughened glass sheet. As a result of rapid cooling, there are compressive stresses (-) on the outside, and tensile stresses (+) on the inside.*

Another technique to create flat glass exists, called the overflow downdraw process (Figure 2.12). Here, instead of the molten glass going onto a tin bath, it is poured into a V-shaped trough until it flows down the sides. When the glass meets on the bottom of the trough, a sheet is formed. This process, especially useful for creating very flat thin (< 3 mm) glass, was invented by Dockerty (1967), but wasn't used much for decades. In recent times, however, it has been used to create thin glass for electronics, such as touch screens for smartphones and tablets.

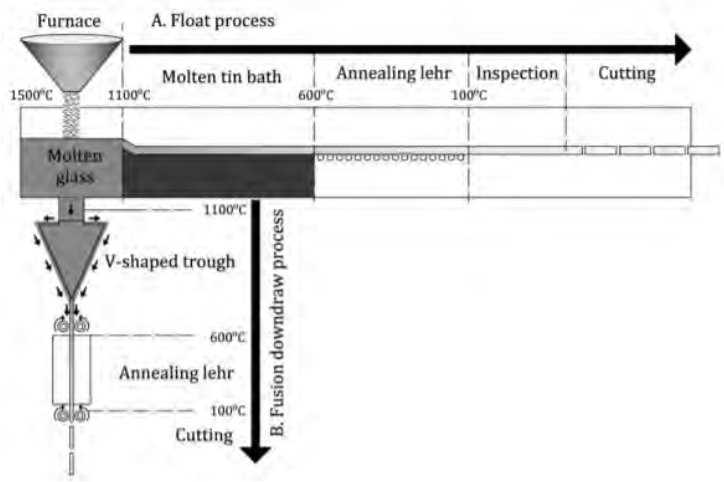

Figure 2.12: *Schematic overview of the float process and the overflow downdraw process for creating flat glass. The float process is shown on top, following the horizontal arrow, and the overflow downdraw process is shown on the bottom, following the vertical arrow. Image from Datsiou (2018).*

2.2.2 Glass types and chemically toughening

Traditionally, soda lime silica, or soda-lime, glass has been the most common glass used in the building industry. Whether annealed, heat strengthened or fully toughened glass is used for glazing, and whether it is flat or bent, soda lime silica glass is the standard. However, for thin glass, soda lime silica glass is not the most ideal. This is because thermal toughening is not effective in glass that is less than 3 mm thick. Therefore, chemically toughening is applied.

To chemically toughen a glass pane, it is placed in a bath of molten salt. An exchange occurs between the ions in the glass and the ions in the salt. Because larger ions are transferred from the salt to the glass and replace smaller ions, e.g. potassium (K) replacing sodium (Na), a compressive stress develops in the outer edges of the glass.

A very important aspect in the final strength of the glass is the case depth Figure 2.13) that is achieved through the toughening process. The case depth is the depth at which the prestress reaches zero. The larger the case depth, the more resistant the glass is to bending and to scratches. It is difficult to achieve a large case depth and large precompression in regular soda-lime glass. With aluminosilicate glass, a much higher precompression and larger case depth can be achieved (Figure 2.14). With aluminosilicate glass comes a difficulty: in order to create thin glass, it has to be done through the overflow downdraw process at high temperatures. Because of the high temperatures, the oven needs to be of higher quality or will have a lower service life, leading to higher prices.

Figure 2.13: *Schematic stress profile of chemically toughened glass. Case depth d (usually very small compared to the full glass thickness) is the depth at which the prestress reaches zero.*

A relatively new development by AGC is a relatively new glass type, called Falcon glass. This glass type has elements in its composition of both soda-lime glass and aluminosilicate glass. Due to its composition, it can be created using the float process, and is thus cheaper to produce than aluminosilicate glass. Despite this, it is still very usable in chemical toughening. The case depth and precompression are slightly lower than that of aluminosilicate glass (Figure 2.14), but much better than soda-lime glass. These characteristics make it an excellent and cheaper alternative to aluminosilicate glass for the creation of thin chemically toughened glass.

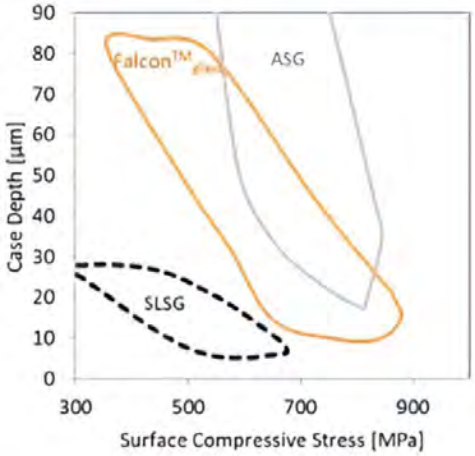

Figure 2.14: *Case depth and surface compressive stress for soda lime silica glass (SLSG), Falcon glass, and aluminosilicate glass (ASG). Image from Zaccaria and Gillon (2019).*

2.3 Cold twisting glass

Twisting a glass plate is a way of creating a more visually interesting shape, as well as giving the plate more resistance against out-of-plane loads. Due to the curvature, membrane forces are activated in the glass when it is loaded. There are of course limits to how far the glass can be bent. When the curvature is large enough, the outer parts of the glass will reach their ultimate strength, and the glass will break. However, for glass twisted into a hyperbolic paraboloid, or hypar, there is another type of limit. When the corners are deflected too far, one of the diagonals will straighten (Galuppi (2014), Figure 2.15). This form of elastic instability is a big factor in not being able to achieve large deformations with cold twisted glass. Since large deformations are exactly what is needed in order to be able to use thin(ner) glass in building applications, it would be useful to find a solution for this problem. In this paragraph, the problem and a possible solution are described.

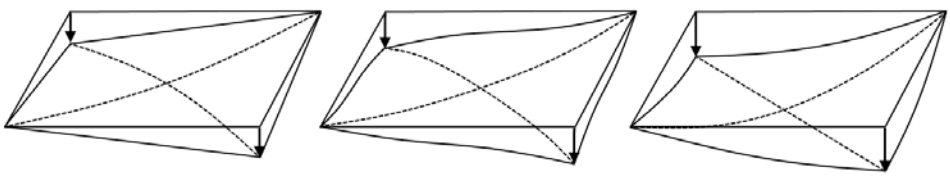

Figure 2.15: *Buckling of a twisted plate. From left to right: 1) two corners are pushed downwards, twisting the plate into a hypar shape, 2) the plate is deflected further and the edges start showing an s-curve, 3) one of the diagonals straightens. Image adapted from Galuppi (2014).*

2.3.1 Buckling phenomenon

The Kirchoff-Love theory of plates predicts a plate that is twisted by an out-of plane displacement of two corners to take on the shape of a hyperbolic paraboloid (Love, 1888). No matter how large the displacement is, the theory is linear, so it says that the edges will remain straight. However, multiple studies into cold twisting glass have revealed that in reality this is not the case.

At smaller deformations, the Kirchoff-Love theory is accurate. The edges remain straight, and the glass is formed into a nice saddle-shaped hypar (Figure 2.16a). When deformed further, we can see both from numerical simulations and experiments that the saddle-shape still exists, but the edges start curving, so it is not a true hypar anymore (Figure 2.16b). When this seemingly local instability starts occurring, the bending is still still symmetrical. That is, the two diagonals have the exact same shape, but have different orientations. At high deformations, one of the diagonals straightens (Figure 2.16a). Bending occurs mainly on the other diagonal, creating a cylinder-like deformation. Galuppi (2014) describes this phenomenon as "buckling caused by a bifurcation of the equations of static equilibrium", citing Bigoni (2012). We can call this type of elastic instability "buckling", as it is caused by a compression zone in the central region of the plate. This compression zone is caused by the horizontal components of the applied force. In Figure 2.17, this is visualised by showing the forces on one of the diagonals. When the force is applied normal to the glass plane, due to second-order effects, the force will develop a component in the direction of the glass, causing the diagonal to be compressed. When this component reaches a critical point (similar to the Euler critical load for columns), the diagonal buckles.

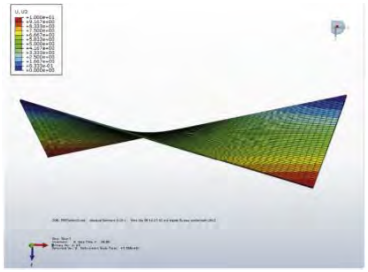

(a) *Prescribed corner displacement of 10 mm. The edges remain straight and the plate takes the shape of a perfect hyperbolic paraboloid.*

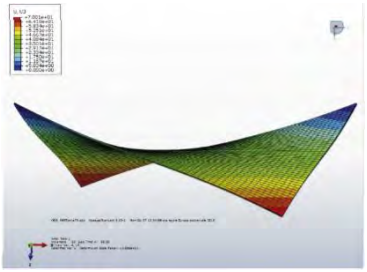

(b) *Prescribed corner displacement of 70 mm. The edges start to curve and the plate is no longer a perfect hypar, though it is still saddle-shaped.*

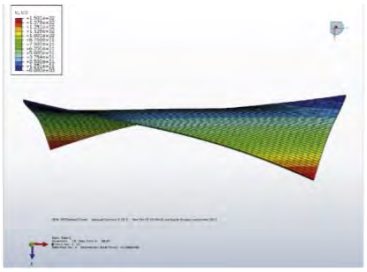

(c) *Prescribed corner displacement of 150 mm. One of the diagonals has straightened, and the panel has lost the saddle shape.*

Figure 2.16: *Numerical simulation of a cold twisted plate by Galuppi (2014), where two corners are given an out-of-plane prescribed deformation. The plate is* 2×2 *m, with a thickness of 10 mm. Note that the deflections are scaled by factors 50 for Figure (a), 10 for Figure (b), and 3 for Figure (c).*

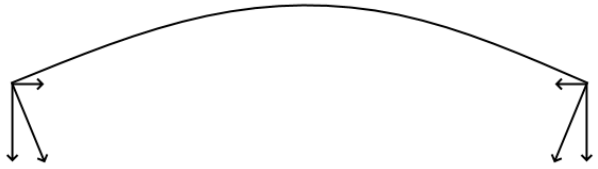

Figure 2.17: *Simple scheme of the applied load on one of the diagonals. Due to second-order effects, the applied force develops a horizontal component.*

The previously described buckling phenomenon has been shown in multiple experimental studies. Two of them are of particular interest. The first one is a study done by Staaks (2003), which is interesting, because it is one of the earlier studies in this specific topic. It also identifies

several key aspects in what causes this phenomenon. The second one is part of the PhD research by Datsiou (2018). This fairly recent study included experiments with square glass plates, so the results are very relevant for this thesis.

Staaks (2003) conducted experiments with cold twisting polycarbonate plates of 435×435 mm, 435×653 mm and 435×870 mm, plate types I, II and III respectively, all with a thickness of 5 mm. The latter two are not discussed here, since they are not square and therefore not entirely relevant. The plates were supported on all four corners. To twist the plates, two corners were pushed upward using threaded rods (Figure 2.18a), during which out-of-plane movement was possible around the supports.

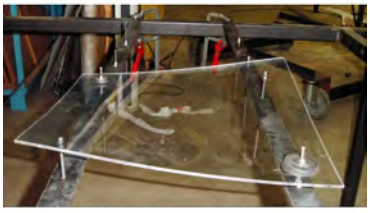

(a) *The setup consists of a polycarbonate plate supported at all four corners. Two corners are held in place, while the other two are pushed upward.*

(b) *At an upward displacement of 10 mm, the expected saddle shape (hyperbolic paraboloid) is achieved, but the edges have started curving.*

(c) *At a displacement of 30 mm, the supported diagonal has straightened. The plate goes from a double curved shape to a seemingly single curved shape.*

Figure 2.18: *Experiments done by Staaks (2003) with a polycarbonate plate of* 435×435 *mm and a thickness of 5 mm. Subfigures 2.18b and 2.18c have been vertically stretched by* 400% *to clearly show the deformations.*

An important observation in the Staaks (2003) experiments was that plate types II and III - the rectangular ones - had a 'very large' deformation due to self-weight, and therefore no useful conclusions could be drawn from the experiments that were performed with them. The square plate I, on the other hand, showed a very clear characteristic behaviour that was in line with the expectations.

The initial deformation phase (Figure 2.18b), there is very clearly a hypar-like shape. The edge is not perfectly straight, but it is very close. At a certain point, the hypar shape changes into a surface that looks almost like a single curved shape. According to Staaks (2003), it was not clear during the experiments if this happened gradually or abruptly. From the results of this experiment, we can conclude that the theorised buckling behaviour actually occurs in a physical plate.

Influence of thickness

The relative thickness, i.e. the ratio between the thickness and the size of the plate, affects the timing and nature of the diagonal straightening phenomenon of cold twisted glass. As well as the previously mentioned tests with polycarbonate plates, the research done by Staaks (2003) included a series of experiments where square and rectangular glass plates were cold-twisted (Figure 2.20). Three sizes, shown in Table 2.2, were used, two mostly square specimens (A and B), and one rectangular one (C). The relative thicknesses of the two square specimens differed from each other, with specimen A being somewhat thinner compared to its size. With plates that have a higher relative thickness, the straightening happens suddenly, causing a kind of snap-through buckling effect. With thinner plates, the diagonal will straighten with less corner deformation, and will happen more gently. This effect can be seen in Figure 2.19, where the

results of experiments done by Staaks (2003) are shown.

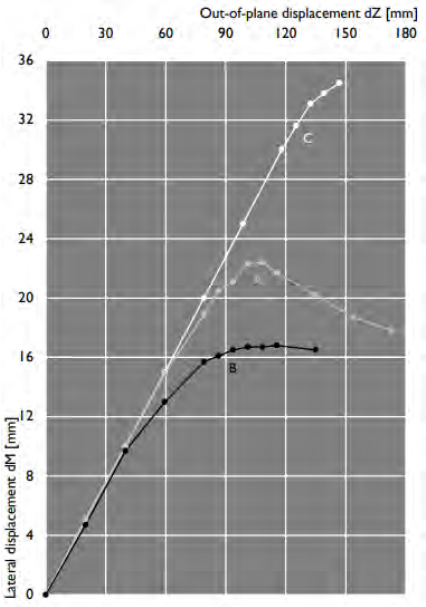

Figure 2.19: *Experimental results (Staaks, 2003) showing the elastic instability that happens when cold-twisting glass. For this experiment, one of the corners is moved upwards to twist the panel (Figure 2.20), which is plotted on the horizontal axis. The deflection of the midpoint is plotted on the vertical axis. Three panels are compared, with different dimensions, aspect ratios and thicknesses, shown in Table 2.2.*

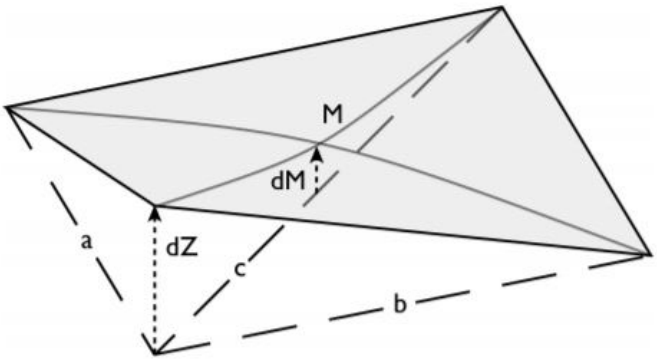

Figure 2.20: *Schematic representation of the experiments done by Staaks (2003). One corner is pushed upwards, twisting the panel and creating a hypar. This is equivalent to deflecting two opposite corners.*

Specimen	Dimensions	Thickness
A	1721 × 1688 mm	8 mm
B	1779 × 1800 mm	10 mm
C	2066 × 1088 mm	10 mm

Table 2.2: *Dimensions of the panels used for the experiments by Staaks (2003).*

2.4 Thermal insulation and air pressure

A façade element has one main goal: to keep the outside climate outside. In order for this to work, it must be insulated. A few issues specific to the type of Insulated Glazing Unit (IGU) used here are discussed in this section.

2.4.1 Thermal insulation

A very important aspect of a façade element is its thermal insulation. Thus, when designing such a building product it is necessary to consider it carefully. IGUs have been used in buildings for decades as a way to create a transparent, but still insulated, surface. The cavity filled with gas (e.g. air, argon or krypton) acts as an insulating layer, and stops the heat from being quickly conducted from outside to inside or vice versa. Nowadays, coatings are often applied to the glass, to significantly reduce radiation.

In terms of thermal insulation, the largest difference between a standard size IGU and the frame that is being designed here is the size of the cavity. In order to be able to use the frame in real-world applications, the thermal insulation must not be (significantly) lower than that of a standard size IGU. Therefore, a comparison is made here between the two.

There are three main factors in determining the heat resistance of a façade: conduction, radiation and convection. As cavity size increases, the heat has to pass through more of the gas, so the transmission through conduction decreases. At the same time, the gas gets more space to move around and form currents, so convection increases, resulting in decreased insulation. Heat transmission through radiation is not affected by the size of the cavity. The contributions of these effects can be seen in 2.21. For the new frame to comply with the requirements, the sum of the changes in conduction and convection must be approximately zero, or must result in less heat transmission than a standard IGU.

The contribution of each of the three transmission methods can be calculated separately and then added up. Heat transmission is measured in W/(m^2·K) and denoted with the letter α. Subscripts cd, r and cv are used for conduction, radiation and convection, respectively.

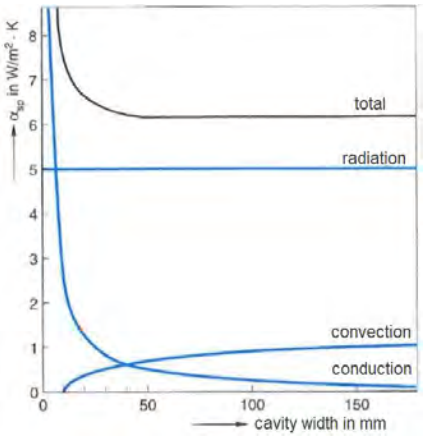

Figure 2.21: *The relation between cavity width of an insulated glazing unit and the heat transmission. Image taken from Van der Linden (2018), adjusted with English translations.*

Two IGUs are compared: one with two glass panes of 4 mm and a cavity of 12 mm (4-12-4), and one with a cavity of 40 mm (4-40-4). In order to make a complete comparison, the 4-12-4 unit is also displayed including argon and krypton, as these are often used in practice. Low-E coatings are also taken into consideration. Although they do not influence the comparison, since they can be used on both IGU types and has the exact same effect on both. Nevertheless it is interesting to show their influence on the heat resistance.

The heat transmission through radiation is constant for the purpose of this comparison. Without low-E coating it is $\alpha_r = 5$ W/(m^2·K), and with coating it is $\alpha_r = 0.3$ W/(m^2·K).

The effect of conduction depends on the thermal conductivity λ and the depth of the cavity d. Their relation defined as

$$\alpha_{cd} = \frac{\lambda}{d} \tag{2.1}$$

Finally, convection is governed by the cavity depth. Van der Linden (2018) gives a value of $\alpha cv = 0.25$ W/(m^2·K) for a cavity of 12 mm. It also states that for cavities >20 mm, the reduction of heat transport through conductivity is cancelled out by the increase of heat transport through convection. Together they are given as $\alpha_{cd} + \alpha_{cv} = 1$ W/(m^2·K), where it is assumed that $\alpha_{cd} = \alpha_{cv} = 0.5$ W/(m^2·K).

The heat resistance of the IGU R_c can be calculated as

$$R_c = \frac{1}{\alpha_{cd} + \alpha_r + \alpha_{cv}} \text{ [m}^2\text{K/W]} \tag{2.2}$$

The combined results are given in Table 2.3.

Unit	λ [W/mK]	α_{cd} [W/(m^2·K)]	α_r [W/(m^2·K)]	α_{cv} [W/(m^2·K)]	R_{sp} [m^{2}K/W]
4-12-4 air	0.025	2.08	5	0.25	0.14
4-12-4 argon	0.0177	1.48	5	0.25	0.15
4-12-4 krypton	0.0094	0.78	5	0.25	0.17
4-12-4 low-E air	0.0250	2.08	0.3	0.25	0.38
4-12-4 low-E argon	0.0177	1.48	0.3	0.25	0.49
4-12-4 low-E krypton	0.0094	0.78	0.3	0.25	0.75
4-40-4 air	0.025	0.5	5	0.5	0.17
4-40-4 low-E air	0.025	0.5	0.3	0.5	0.77

Table 2.3: *Comparison of insulation value of IGUs with different properties. The cavity size, gas in the cavity and type of coating are varied. Heat transport through conduction, radiation and convection are calculated separately, and added up to a single insulation value.*

2.4.2 Air pressure

For the frame to work as an IGU, it must be fully hermetically sealed, or very lightly ventilated. If air could freely flow in and out of the frame, the air currents inside would be much more severe, which would decrease the thermal insulation. Air entering the cavity can also cause issues with condensation. Therefore, it must be guaranteed that the frame is free of leaks.

However, making the cavity airtight comes with challenges. For the design, the challenges in terms of structural performance are the most relevant. Every movement that happens in the frame, whether that be due to bending/warping, wind load, impact load, or any other type of loading, will result in the glass deforming. The deformed glass causes a change in volume of the cavity. Boyle's Law states that the volume and pressure of a gas are inversely proportional (Boyle, 1660), and thus the change in volume will lead to a change in pressure. The change in air pressure will help the load distribute over the inner and outer pane. This behaviour is advantageous for the structural performance, but difficult to predict, so it needs to be carefully modelled in case of a structural finite element model.

The change of air pressure due to movement may also significantly impact the behaviour during the shaping process, i.e. the warping of the frame. During warping, the two glass panes move towards each other in the middle, which will decrease the volume of the cavity and thus increase the pressure, which could have an undesirable effect on the warping.

The final structural challenge is due to temperature differences. Gas expands with increasing temperature, and vice versa. Because the cavity is airtight, this results in a change in volume, and, once again, a change in pressure. Because of the broad range in temperatures a façade element is subject to, the change in pressure can be quite large. It depends on the stiffness of various elements of the frame if this leads to significant stresses, and this will need to be examined if this concept is to be used as a building product. Temperature differences can cause significant pressures, which is problematic when using thin glass as its stiffness is low. However, we can minimise the effect of temperature differences, by not hermetically sealing the cavity. Instead, the cavity can be made airtight, with a valve integrated somewhere in the spacer assembly. If the flow rate of the valve is chosen carefully (i.e. a low enough flow rate), it can allow the long term load due to pressure difference from temperature change to dissipate, while allowing the air in the cavity to spread short term loads from one glass pane to both panes. An important requirement is that any and all air entering the cavity through the valve is desiccated beforehand to avoid condensation issues.

2.5 Adhesive choice and modelling

The properties of the adhesive that is used to attach the glass to the spacer are very influential for the behaviour of the panel. Too stiff and it will create a clamped edge, inducing stresses in the glass. Too flexible and the adhesive will tear too soon due to high strains.

2.5.1 Adhesive choice

First, the choice is made for what type of adhesive should be used. Two types are considered: epoxy resin and structural silicone. Generally, epoxy resin is stiffer and stronger. The higher strength is a positive for cold-bending to high curvatures, as this may induce relatively large stresses in the adhesive. Structural silicone is often used in structural glazing, and its combination of flexibility and strength make it well suited for cold bending.

In the design and experiments by Fedoseeva (2017) and Young (2019), both epoxy resin and silicone were considered as well. From the research carried out by Fedoseeva (2017), it was found that the best option for the panel would be KÖMMERLING Körapox EP 40619 & EP 42091 (Körapox), which is an epoxy resin. It was concluded that Körapox had the right combination of strength and stiffness, which is why it was the final recommendation. However, during the experiments by Young (2019), Körapox proved to be too stiff. This became apparent due to the adhesive prematurely debonding and tearing at the glass interface. From these findings, it was obvious that something stronger and more flexible was required for this specific application.

In consultation with Dow, DOWSIL 993 (D993) Structural Glazing Sealant was chosen for the research in this thesis. This silicone adhesive is a widely used structural glazing adhesive. Its combination of strength and stiffness have made it a popular choice for use with cold-bending, so it has precedence in similar applications. The properties of this silicone are also in line with the findings from the research in Cambridge.

2.5.2 Silicone modelling

Modelling the structural behaviour of the adhesive is of vital importance to the behaviour of the entire model. The stiffness of the adhesive and the type of material model greatly influence the stiffness of the panel in torsion and lateral loading. As described in Section 2.1, silicone was used as the adhesive in earlier research into this system. Silicone is also the adhesive of choice in the design of the panel that is used in this research.

Silicone has some unique traits. It is a hyperelastic material, which means it can be stretched very far until it breaks (more on this in Paragraph 2.5.3). It is also incompressible, which influences its behaviour. Therefore, the material model that is used in the FEA must be carefully chosen. In this part of the literature study, the options are laid out and discussed.

2.5.3 Material model

To choose a material model, it should first be clear what the options are. Two options for modelling the silicone exist: linear elasticity, and hyperelasticity.

Linear elasticity

The most simplistic way to model any material is using a linear-elastic material model. In this type of model, the material is described using only two numbers: a constant Young's modulus (E, [Pa]) and a Poisson's ratio (ν, [-]). A constant Young's modulus describes, by definition, the linear elastic relation between strain and stress, such as in Figure 2.22. In other words, if a material is elongated twice as much (e.g. from 5% elongation to 10% elongation), the stress is doubled and vice-versa. The Young's modulus is therefore a measure of stiffness. The Poisson's ratio describes the amount of expansion or contraction perpendicular to a load

(Figure 2.23). This Poisson's ratio is particularly interesting for silicone and other rubber-like materials, which are considered incompressible (Martins et al., 2006). This means that, unlike many other materials, there is no change in volume when silicone is compressed, resulting in a (theoretical) Poisson's ratio of 0.5. In reality, rubber-like materials such as silicone are not 100% incompressible, making the Poisson's ratio ever so slightly lower than 0.5 (e.g. 0.4999 (Mott and Roland, 2009)). In most cases, using $\nu = 0.49$ gives accurate results.

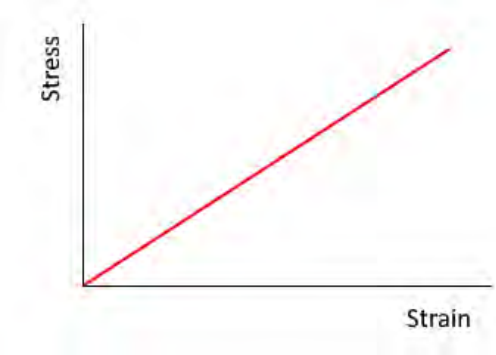

Figure 2.22: *Generic example of linear elasticity, with a linear relation between strain (horizontal axis) and stress (vertical axis).*

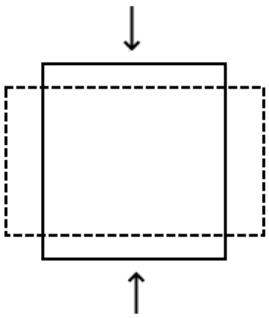

Figure 2.23: *Schematic example of a material expanding laterally due to a compressive load.*

The greatest strength of this model, its simplicity, is also its greatest weakness. The linear-elastic model is easy to comprehend and easy to incorporate. However, due to its simplicity, it can only model fully linear-elastic behaviour. In reality, silicone does not show fully linear-elastic behaviour, so the linear-elastic material model is likely to deviate from experimental results.

Hyperelasticity

An important characteristic of rubbers is that they behave elastically up to very high strains. For example, a rubber band can be extended by a large amount, and it will still return to its original shape when released. To accurately model this behaviour, in combination with incompressibility, hyperelastic models have been developed. Widely used hyperelastic models include the Neo-Hookean, Mooney-Rivlin and Ogden models. Several of these models are proposed by Dow, i.e. the Ogden, Mooney-Rivlin and Yeoh models. These three models give very similar results when used in a FE-analysis (Figure 2.24). The Mooney-Rivlin model - and by extension, the Neo-Hookean model, since it is a specific case of Mooney-Rivlin - is the only one included in DIANA, so that model is considered an option for modelling the silicone. It must be mentioned that DIANA only supports the two-parameter version of the Mooney-Rivlin model. A five-parameter version exists as well, but this version is usually only necessary when the strains exceed 100%, since the two-parameter version is accurate enough for strains below that number (Muhsin and Hassan, 2010).

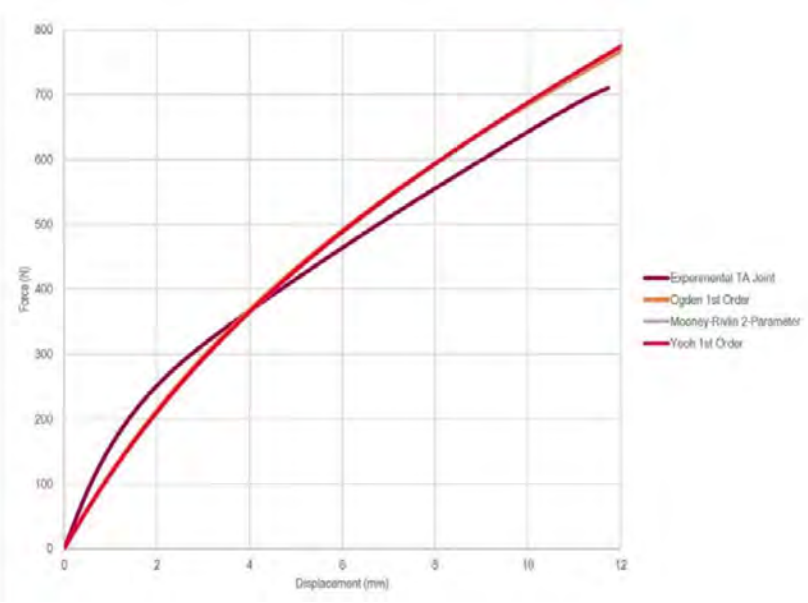

Figure 2.24: *The Ogden, Mooney-Rivlin and Yeoh models compared with experimental data. Image from Dow (2018a).*

Most models that are relevant for silicone are based on strain energy density functions. These describe the amount of energy needed to deform a unit volume of a solid. Melvin Mooney (1940) and Ronald Rivlin (1948) developed the first hyperelastic models, including the aptly named Mooney-Rivlin model. The Mooney-Rivlin model is essentially a compact notation of the strain energy density function. In this notation, the invariants I_1 and I_2 of the left Cauchy-Green deformation tensor $\mathbf{B}$ are multiplied by empirical constants C_1 and C_2. The invariants are made up of the principal stretches λ_1, λ_2, and λ_3, and are defined as follows:

$$I_1 = \lambda_1^2 + \lambda_2^2 + \lambda_3^2 \tag{2.3}$$

$$I_2 = \lambda_1^2\lambda_2^2 + \lambda_2^2\lambda_3^2 + \lambda_3^2\lambda_1^2 \tag{2.4}$$

A third invariant exists, i.e. $I_3 = \lambda_1^2\lambda_2^2\lambda_3^2$. However, because of the assumption of incompressibility, $\lambda_1\lambda_2\lambda_3 = 1$, so $I_3 = 1$ (Dos Santos et al., 2014). The invariants are written into the strain energy density function W as:

$$W = C_1(I_1 - 3) + C_2(I_2 - 3) \tag{2.5}$$

Using the strain energy density function in this form (Haines and Wilson, 1979), and the principal stretches that are implicitly included in it, the stresses and deformations can be determined in the finite element model.

3

Finite element modelling

3.1 Silicone adhesive modelling

Dow, the manufacturer of the chosen adhesive, has provided documents with recommendations for how to model the silicone. In addition to that, from the options mentioned in Paragraph 2.5, the hyperelastic Mooney-Rivlin model is chosen as the most suitable alternative to model the silicone. The linear-elastic model is too simplistic, and does not match with the actual behaviour of silicone. The hyperelastic Mooney-Rivlin model is not only recommended by the supplier of the silicone, but it was created with hyperelasticity and incompressibility in mind. Therefore, the silicone should be modelled using this model.

3.1.1 Calibration

The manufacturer of the silicone, Dow, has created a document with which clients can calibrate their finite element analyses of the 993 structural glazing sealant. For the calibration, a tensile test is performed on a small silicone sample holding together two structural steel substrates, as shown in Figure 3.1. This type of test specimen is called an H-piece, as usually the plates extend beyond the adhesive, making the specimen resemble the letter *H*, but in this case the plates have the same area as the adhesive.

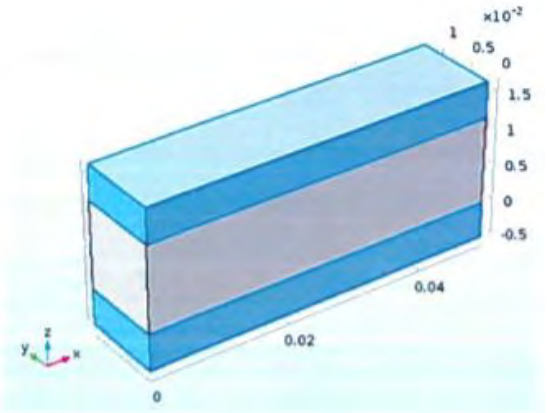

Figure 3.1: *The test piece that is modelled in the calibration of the silicone. The silicone is shown in the middle as grey/white, the steel substrates are shown in blue on the top and bottom.*

Dow provides several specifications to build the model. These include dimensions, material parameters, support conditions and load.

Dimensions and mesh

The dimensions are given by Dow as follows (length × width × height, or x × y × z-directions):

- Dimensions of the silicone: $50 \times 12 \times 12$ mm;
- Dimensions of the substrates: $50 \times 12 \times 5$ mm.

Two meshes should be used and compared for the silicone, a fine and a coarse mesh. The fine mesh should have $1 \times 1 \times 1$ mm cells, and the coarse mesh should have $2 \times 2 \times 2$ mm cells. The mesh of the substrates is allowed to be coarser, but is kept the same size as the mesh for the silicone for the sake of simplicity, as calculation time isn't an issue with this model. It is not mentioned whether the mesh should be linear or quadratic, but it is assumed that a linear mesh was used by Dow, since all results are only given at the vertices of the mesh.

Material parameters

The material parameters for the steel substrates are not of great importance, as long as the deformation in them is negligible. However, Dow recommends using stainless steel with a linear-elastic material model, and the parameters given in Table 3.1.

Quantity	**Symbol**	**Magnitude**
Density	ρ	7850 [kg/m^3]
Poisson's coefficient	ν	0.3 [-]
Young's modulus	E	200 [MPa]

Table 3.1: *The steel material parameters that are to be used in the calibration of the FE-model of the D993 silicone by Dow.*

The parameters for the silicone *are* very important, as they define how the model behaves. Dow prescribes the use of the Neo-Hookean model for the silicone, with the parameters in Table 3.2.

Quantity	**Symbol**	**Magnitude**
Density	ρ	1100 [kg/m^3]
Poisson's coefficient	ν	0.49 [-]
Young's modulus	E	1.95 [MPa]

Table 3.2: *The silicone material parameters that are to be used in the calibration of the FE-model of the 993 silicone by Dow.*

Quantity	**Symbol**	**Relation**	**Unit**
Shear modulus	G	$\frac{E}{2(1+\nu)}$	[MPa]
Bulk modulus	K	$\frac{E}{3(1-2\nu)}$	[MPa]
Lamé parameter	μ	$\frac{E}{2(1+\nu)}$	[MPa]

Table 3.3: *Relations to derive additional material parameters from the given parameters.*

The Neo-Hookean model is not explicitly available in DIANA. However, the Neo-Hookean model is a special case of the Mooney-Rivlin model, where the C_2 from Equation 2.5 equals zero, so the strain energy density function for the Neo-Hookean model is defined as Equation

3.1. The C_1 in this case can be found from the Lamé parameter that is given by using Equation 3.2.

$$W = C_1(I_1 - 3) \tag{3.1}$$

$$C_1 = \frac{\mu}{2} = 3.27 \times 10^5 \text{ Pa} \tag{3.2}$$

Support conditions and load

As this is a simple tensile test, the boundary conditions and loading are fairly straightforward. The bottom substrate is fully supported in all directions. This will further guarantee that the substrate deforms as little as possible. The load is applied on the entire top surface of the model. The exact magnitude of the load is not given, but the document says to 'check the results when the reaction force in the silicone reaches 0.14 MPa and 0.84 MPa'. With these conditions, the silicone is checked at a point when it still acts as a linear material, and at a point where its hyperelastic character is shown. In further clarification, Dow specifies the load as an upward prescribed displacement of 12 mm. This load is applied in 60 time steps of one second each. To recreate this, the displacement is applied in 60 equal increments.

Calibration values

The document by Dow gives two options for checking the results. The first is to check the results at the entire plane where the silicone meets the top substrate. For a few different quantities, the maximum figures are given for this plane. The second option is to check the results along a line that runs horizontally from the middle of the aforementioned plane to the long edge of the plane. See Figure 3.2 for an illustration of these locations.

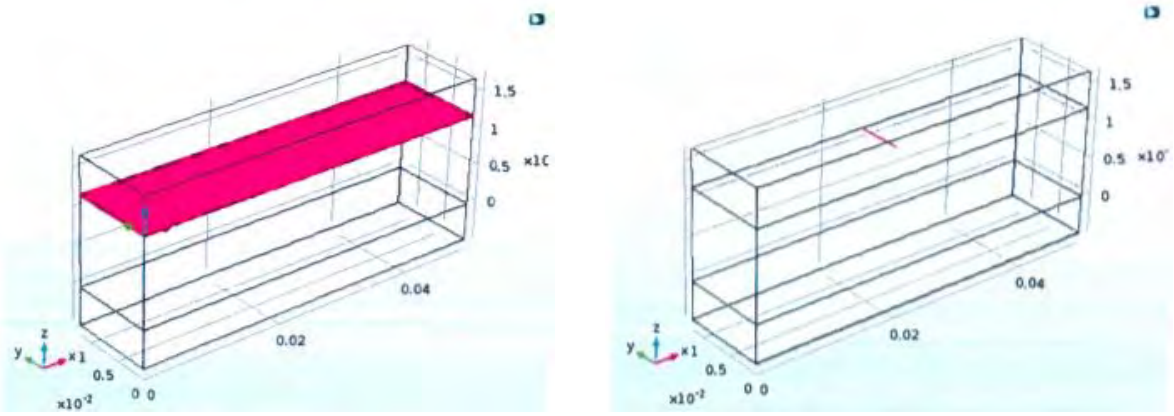

(a) *Check the results on the plane where the silicone and the top substrate meet. For several quantities, the maximum numbers are given for this plane.*

(b) *Check the results on a line that runs from the middle of the plane where the silicone and top substrate meet to the edge. A graph is given for the strain magnitude along this line.*

Figure 3.2: *The two options for checking the results. Dow (2018b)*

Quantity	**Magnitude**				**Unit**
Mesh size	1		2		[mm]
Reaction force	0.139	0.840	0.140	0.841	[MPa]
Elongation	5	45	5	45	[%]
Von Mises stress	0.389	2.533	0.302	1.961	[MPa]
1st principal strain	0.295	2.860	0.219	2.115	[-]
Strain magnitude	0.313	2.859	0.234	2.138	[-]

Table 3.4: *Results of the model by Dow, split into the fine (1 mm) and coarse (2 mm) mesh.*

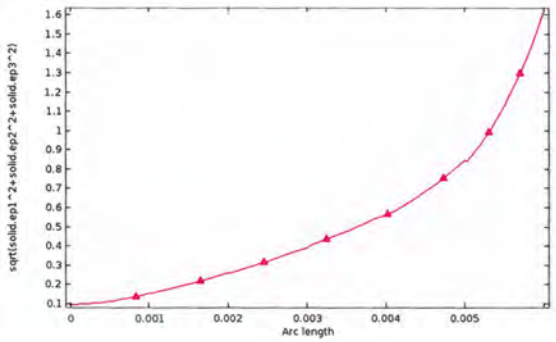

(a) *Strain magnitude for the 1 mm mesh.*

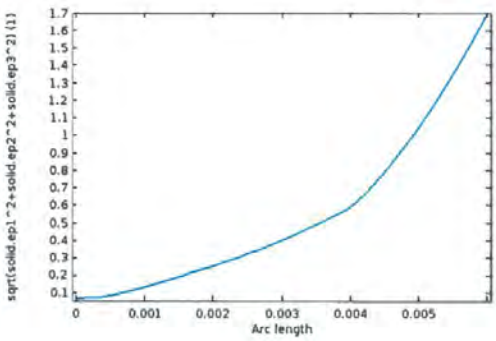

(b) *Strain magnitude for the 2 mm mesh.*

Figure 3.3: *The graphs of the results provided by Dow. Both graphs show the strain magnitude on the vertical axis. The strain magnitude is defined as the square root of the sum of all principle strains squared:* $\sqrt{\varepsilon_1^2 + \varepsilon_2^2 + \varepsilon_3^2}$. *These strain magnitudes are plotted along the length of the cut line shown in Figure 3.2b. The axis runs from the center of the cut plane (0 on the horizontal axis) to the edge of the specimen (0.006 on the horizontal axis).*

Verification

Using Dow's specifications, the H-piece was recreated in DIANA, which can be seen in Figure 3.4. The two meshes were combined in one model for ease of use. The document did not specify the use of linear or quadratic elements, but since the geometry was and final deformed shape were not complex, and even the course mesh was fairly dense ($2 \times 2 \times 2$ mm), linear elements were chosen. The silicone was modelled using both the Mooney-Rivlin parameters of given in the technical data sheet for the silicone (Table 3.5, Dow (2018a)), as well as the Neo-Hookean parameters given in the calibration document (Equation 3.2). Displacement control was used to apply the load. The exact elongation of the silicone was specified in percentages, i.e. 5% and 45%, so these were used as an applied deformation. To accurately model the behaviour, a nonlinear analysis was performed, taking both physical and geometrical nonlinearity into account. All results were taken at the interface between the steel substrate and the silicone, but only taking the values from the integration points of the silicone.

Parameter	**Magnitude** [Pa]
C_1	3.3306×10^5
C_1	8.6268×10^3

Table 3.5: *Mooney-Rivlin parameters for the D993 silicone (Dow, 2018a).*

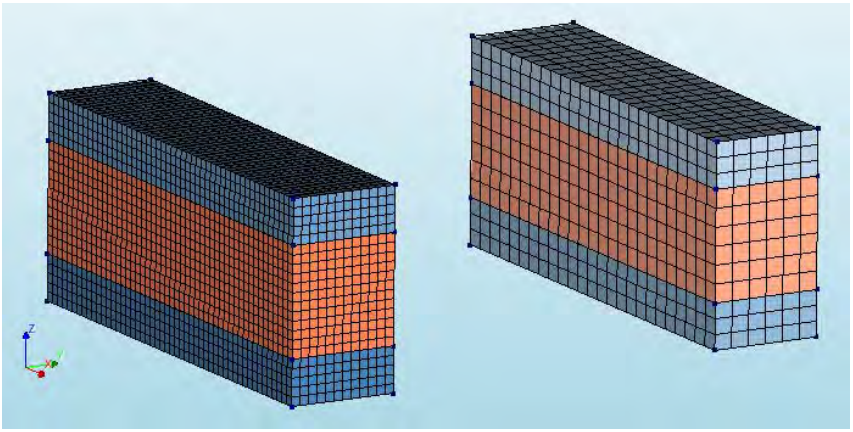

Figure 3.4: *The recreated H-piece with both mesh sizes. The 1 mm mesh size on the left, and the 2 mm mesh size on the right.*

Although the input parameters were fairly straightforward, there was a consistent mismatch in all the models between Dow's results and the results from the DIANA models. In Figure 3.5, the differences in strain magnitude along the cut line are visualised. Note that on the horizontal axis, the arc length along the cut line from Figure 3.2b is plotted. The axis starts at 0.000 m, which represents the center of the silicone, and ends at 0.006 m, which represents the point where the cut line meets the outside edge of the silicone. The units are in [m], to keep consistent with the graphs from the calibration document (Figure 3.3). We can see in Figure 3.3b there is no significant difference between using the Neo-Hookean and Mooney-Rivlin material models. This is logical, as the models are very similar, so it would make sense that the numbers for both material models specified by the manufacturer give similar results.

However, there are significant differences between how closely the Dow results are matched between the coarser and finer mesh. In the finer mesh (Figure 3.5a), the strain magnitude of the Dow model is very closely matched at the center $\frac{2}{3}$rd of the silicone volume. However, at the outer edge the strain magnitude in the Dow model starts moving up sooner, but the difference between the models only goes up to about 15%. It is a different story with the coarser mesh. There, the results strain magnitude in the DIANA model starts in the center at around 0.45 in the center, and ends around 0.75, whereas the Dow model starts around 0.1, and ends around 1.7. Both models have a homogeneously increasing curve, as well as an ever increasing slope. This difference seems to be in line with most differences between the Dow and DIANA models. In Table 3.6, it is visible that the maximum values of the Dow model are consistently higher than the maximum values of the DIANA model.

There is one likely reason for the difference between the models. The geometry of the model is simple, the same material models are used, and there are not many other input parameters. The most likely explanation for the difference is the fact that in the Dow model the load is applied using an explicit, time-dependent solver, whereas the implicit DIANA model has its load-steps applied quasi-statically. This might induce dynamic effects in the Dow model. For example, if we look at Figure 3.5b, the graph of the DIANA model looks like a smoothed out version of the graph of the Dow model, where the peaks - both low and high - have moved towards the average. It is possible that the instantaneous behaviour of the silicone is to have a high peak of strain and stress around the perimeter, and have little mechanical response in the center. When time passes, the stress is redistributed over the whole surface due to viscous effects. This is what is seen in the DIANA model, which is loaded quasi-statically. In the end, the choice between Neo-Hookean and Mooney-Rivlin is not critical, as the difference is less than 5%. As Dow recommends the use of the Mooney-Rivlin material model, this is chosen.

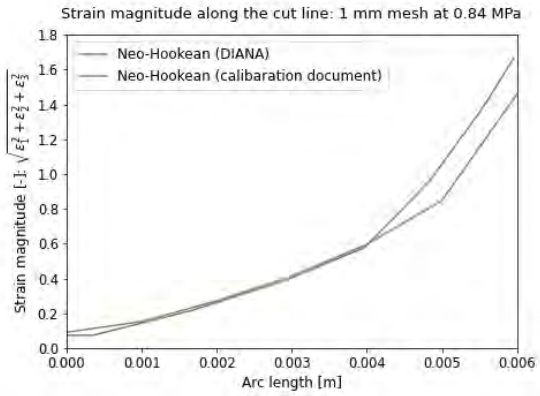

(a) *The results at* 45% *elongation or 0.84 MPa reaction force for the 1 mm mesh. The results match closely on the inside of the silicone, but at arc length 0.004 m, the results from Dow start sloping upward sooner than the DIANA results. Both graphs finish at a similar upward slope, but the DIANA results end around* 10% *lower.*

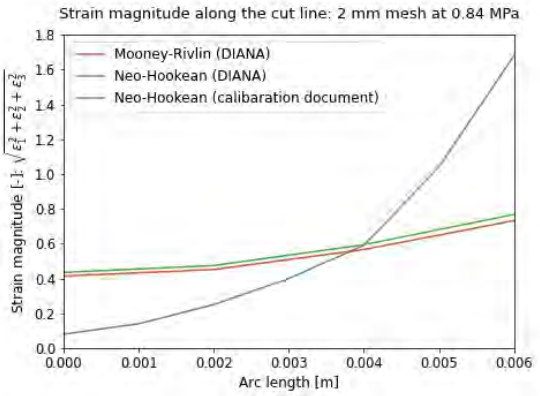

(b) *The results at* 45% *elongation or 0.84 MPa reaction force for the 2 mm mesh. All results have a positive slope from start to finish, but the results from the Dow model start a lot lower and end a lot higher. Note that there is very little difference between the Neo-Hookean and Money-Rivlin material models.*

Figure 3.5: *Comparison between the results from the calibration document and the results from the DIANA model. The horizontal axis represents the cut line, going from the center of the silicone (0.000) to the edge (0.006). Strain magnitude is plotted on the vertical axis.*

Quantity	**Magnitude**								**Unit**
	Dow				DIANA				
Mesh size	1		2		1		2		[mm]
Reaction force	0.139	0.840	0.140	0.841	0.158	0.951	0.165	0.995	[MPa]
Elongation	5	45	5	45	5	45	5	45	[%]
Von Mises stress	0.39	2.53	0.30	1.96	0.27	2.43	0.20	1.83	[MPa]
1^{st} principal strain	0.30	2.84	0.22	2.12	0.17	1.47	0.12	1.05	[-]
Strain magnitude	0.31	2.86	0.23	2.14	0.02	1.14	0.03	2.23	[-]

Table 3.6: *Quantitative comparison between the Dow and DIANA models. The values here are the maximum values along the cut plane shown in Figure 3.2a. Each model is split into the two mesh sizes, and then into the specified reaction force/elongation.*

3.1.2 Maximum stress

Silicone adhesives, as well as other types of hyperelastic materials, are known to be able to deal with large stress peaks. Because of its hyperelastic character, silicone has the ability to distribute large (in magnitude) but localised concentrations of stress very efficiently. Therefore, if the maximum tensile strength given by the manufacturer occurs in either a numerical model or in a real-life application, it does not mean the silicone will actually fail. A common check to see what the stress limits in a finite element should be, is to apply the specified maximum stress to the silicone, and see how high the stress peaks are (Glasscon, 2018). These stress peaks can then be accepted in the full model.

This approach is used to find the maximum acceptable stress peaks. The silicone is modelled with the same dimensions as it has in the full model of Paragraph 3.2.2. A block of steel is modelled on top as a substrate. On top of the steel, a distributed load of 0.95 MPa is applied, which is the tensile strength of D993 according to the manufacturer. This model can be seen in Figure 3.6.

The model is surprisingly unstable, especially given the fact that the stress in the silicone

seems to exhibit linear behaviour. It is difficult to get the load past 70% of the intended load. In the interest of time, the linear stress vs load graph (Figure 3.7) is extrapolated. From this extrapolation, we find that the peak stress in the model at the highest load is 1.65 N/mm^2. This peak stress will be accepted in the model, as long as it's a localised stress concentration.

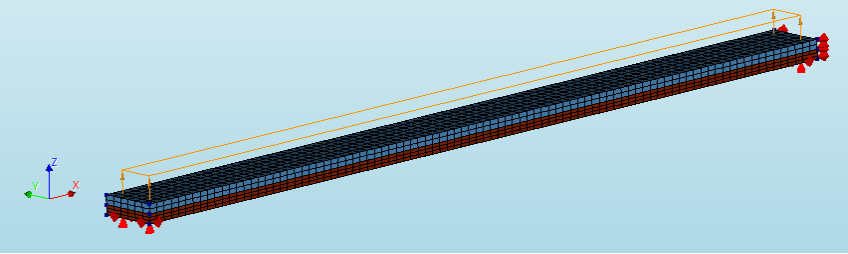

Figure 3.6: *The model used for the determination of the maximum peak stress in the silicone adhesive.*

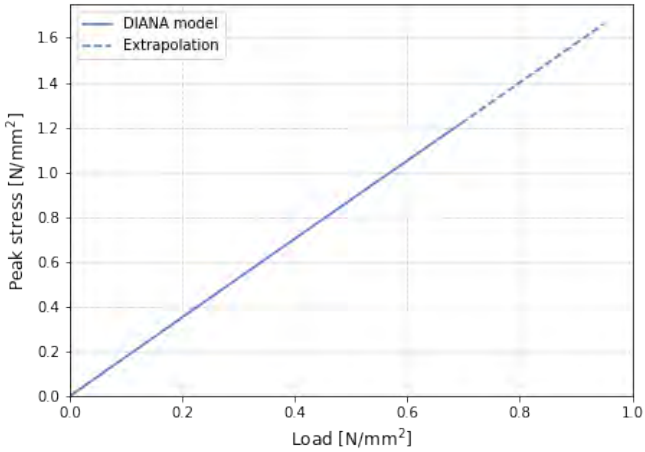

Figure 3.7: *Maximum peak stress in the DIANA model of the silicone. Starting at a load of 0.7 N/mm^2, the graph is extrapolated, because the model did not converge, and the behaviour was perfectly linear.*

3.2 Model build-up

Having established the most important and influential parameters, it is possible to build a finite element model that matches the results of the experiments done in Cambridge by Young (2019) in Cambridge. If this model manages to produce results that are in line with these experiments, the model can be expanded to represent the full sandwich panel.

The first step in creating this model is to make a simple square plate to see if the behaviour is in line with the literature. From there on the FE-model can be expanded upon, i.e. first the frame and finally the second glass plate are added.

3.2.1 Square plate

The plate (Figure 3.8) is modelled after the numerical simulation of Galuppi (2014), which can be seen in Figure 2.16, and consists of a few elements:

- Two-dimensional 2.0 × 2.0 m glass plate (flat shell elements) with a thickness of 10 mm, a Young's modulus of 70 GPa, and a Poisson's ratio of 0.22;
- Pin and roller support conditions at the corners of one diagonal;

- Two vertical displacement controlled point loads (and corresponding supports to restrict the vertical translational degree of freedom) at the corners of the other diagonal;
- Global vertical load to create an imperfection.

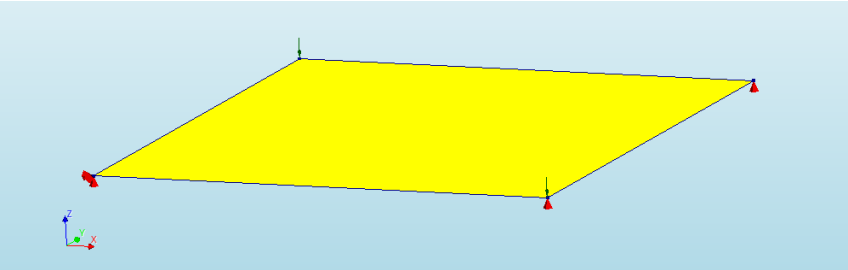

Figure 3.8: *The support conditions of the plate with which the buckling phenomenon is recreated. Pin and roller supports on one diagonal, displacement controlled loads (and corresponding vertical supports) on the other. The imposed displacement is downwards, as well as the imperfection load.*

This model is slightly different from the model made by Galuppi (2014), because in that model solid 3D brick elements are used, and the choice is made to use 2D flat shell elements here. Since the plate is very slender in terms of thickness, and the out-of-plane stress (σ_{zz}) are not of great importance, it is possible to use these two-dimensional elements that are computationally less expensive.

The numerical simulation of the plate without imperfections can form a stable state where neither of the diagonals buckle. However, this state is in reality very unstable, and any disturbance would cause the plate to move to a state where one of the diagonals is buckled. To prevent this, an out-of-plane load of 10^{-3} MPa is applied across the entire plate to slightly push it to one side. The corner loads are then applied, and when they have reached their desired displacement, the 'imperfection load' is removed. The same method is applied by Galuppi (2014).

The plate is evaluated at three prescribed corner displacements of 10 mm, 70 mm, and 150 mm. At 10 mm, as we can see in Figures 3.9a and 3.10a, the plate still behaves according to linear plate theory and very much resembles a hypar. When the displacement is increased further (Figures 3.9b and 3.10b), the edges start curving as expected, and the plate starts diverging from the hypar shape. In the last evaluated step, with a corner displacement of 150 mm, the lower diagonal has buckled. This can be clearly seen with the straight contour lines in Figure 3.10c.

From these images, it can be concluded that the panel behaves as expected. It shows the same general behaviour as the results from Galuppi (2014), and also matches quantitatively. The center point in Figures 3.10a (linear phase, non-buckled) and 3.10b (deformed, non-buckled state) has exactly half the displacement of the loaded points. In the buckled state, the center point has between 25 and 38 mm less displacement than the loaded points in the model by Galuppi (2014), and in the DIANA point the difference 30 mm, which means the models match. The behaviour of the DIANA model also follows what was expected from experiments. Therefore, the model can be expanded by adding the GFRP frame around it, to try to match the experimental results from Young (2019).

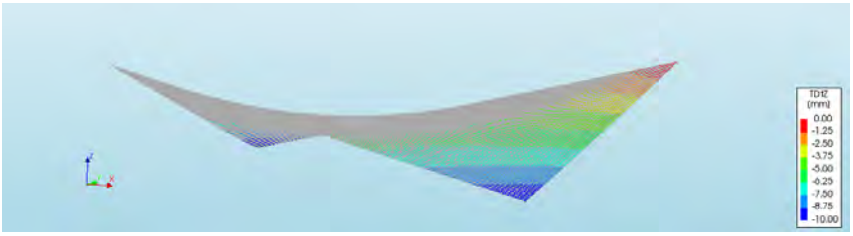

(a) *Corner displacement of 10 mm, with displacements scale factor of 50. The displacement is low, so the plate still looks like a hypar, with straight edges and identical - though flipped - curves between the loaded and supported corners.*

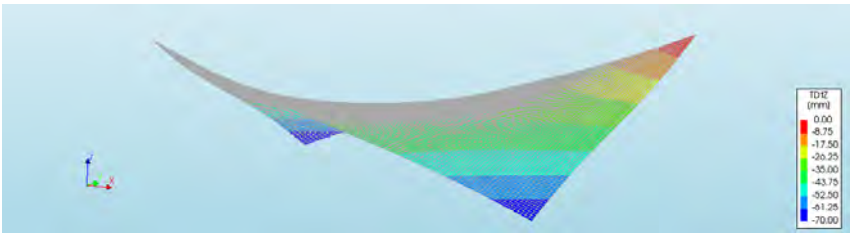

(b) *Corner displacement of 70 mm, with displacements scale factor of 10. The displacement is still relatively low, but is moving out of the range of linear plate theory. Neither of the diagonals have straightened, but the edges are starting to curve, making the plate less similar to a hypar.*

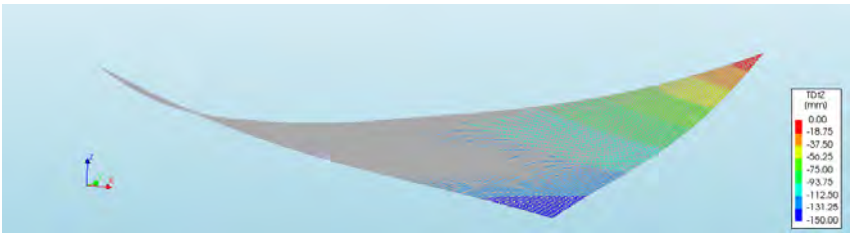

(c) *Corner displacement of 150 mm, with displacements scale factor of 3. The supported corner has buckled because of the higher deformation.*

Figure 3.9: *Recreation of the numerical simulation of a cold twisted plate by Galuppi (2014), where two corners are given an out-of-plane prescribed deformation. The glass plate is* 2×2 *m, with a thickness of 10 mm. In each figure, the scale is shown for the upward out-of-plane (z-direction) displacement. For different views, see Figure 3.10.*

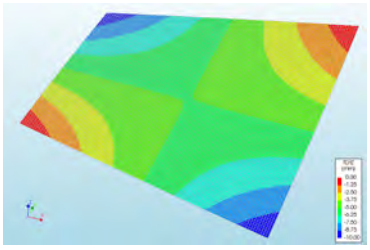

(a) *Corner displacement of 10 mm, with displacements scale factor of 50.*

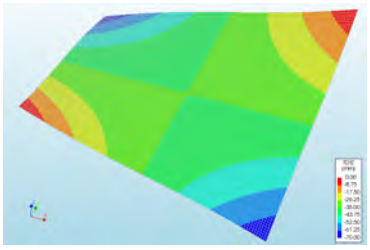

(b) *Corner displacement of 70 mm, with displacements scale factor of 10.*

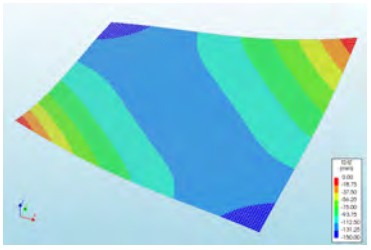

(c) *Corner displacement of 150 mm, with displacements scale factor of 3.*

Figure 3.10: *Recreation of the numerical simulation of a cold twisted plate by Galuppi (2014). For different views and more information, see Figure 3.9.*

3.2.2 Frame addition

The addition of the frame comes with a caveat: not only does the model need to work qualitatively, it needs to replicate the results from the experiments in Cambridge quantitatively. In order to achieve this, the dimensions and mechanical properties of the FE model have to be the

same as the ones used in the experiments.

In those Cambridge experiments, a single 1.0 × 1.0 m thin glass plate of 1.5 mm was used. The plate was stiffened along the edge using GFRP profiles, glued to the glass using a 5 mm thick layer of DOWSIL 795 silicone building sealant (D795). The set-up, shown earlier in Figure 2.9, consisted of the panel, supported on one diagonal with two roll supports, and loaded on the other diagonal. This is quite similar to the plate that was modelled in Paragraph 3.2.1, except stiffened with a frame. Young (2019) states the properties of the GFRP as follows:

- $E_1 = 26$ GPa
- $E_2 = E_3 = 8.5$ GPa
- $\nu_{12} = 0.075$
- $\nu_{23} = 0.23$
- $\nu_{13} = 0.38$
- $G = 3$ GPa

For the D795, Dow has created a technical data sheet specifically for modelling the silicone adhesive. One of the recommended models is the Mooney-Rivlin model, discussed in Section 2.5. The recommended parameters are:

- $C_1 = 1.8303 \times 10^5$ Pa
- $C_2 = 2.1181 \times 10^4$ Pa

To model the glass, standard glass properties are used:

- $E = 70$ GPa
- $\nu = 0.23$

The supports and load conditions are fairly similar to the ones used in modelling the square plate. However, to simulate the load and support conditions in the experiments, and to prevent stress concentrations, loading and support blocks are used. The loading blocks have a Young modulus of 1 GPa, so they don't deform excessively when loaded, and don't impact the stiffness of the spacer or the glass too much. The blocks are only 30 × 30 × 30 mm, so they only affect a small area and are placed at non-critical positions. The model can be seen in Figure 3.11.

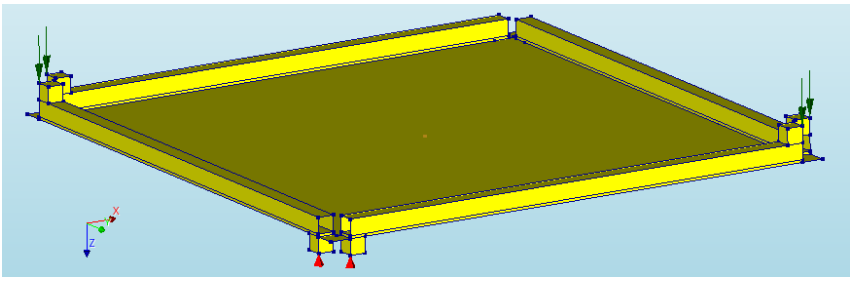

Figure 3.11: *The DIANA model used to simulate the experiments done by Young (2019). Loading blocks and support blocks are used to spread the point loads and supports.*

The supports and loads are defined as points. This is done to create true hinged supports and to prevent any clamping of the corners. If an area support or load would be used, the block would act as a semi-rigid connection, making the panel behave more stiffly and inducing stress where there is none in reality. Normally point loads or supports can The loading blocks help to spread the load and therefore prevent stress concentrations in the model.

Using the findings from Section 3.3, three elements are used over the height of the silicone. The mesh size for the other elements is adjusted to match with the silicone mesh. This is shown in Figure 3.12. Note that the corners of the frame are cut off. This was done to avoid stress

peaks, which can occur in the corners of silicone joints. It also solved a meshing issue. HX25L solid brick elements were used for modelling the silicone, which are strictly 8-node elements. Because of this, they cannot form triangles, which is required to model the corners. In the same figure we can see that the glass is modelled as 2D flat shell elements. Because the results in Paragraph 3.2.1 were accurate, we assume that the 2D elements will suffice to model the glass plate in this model as well.

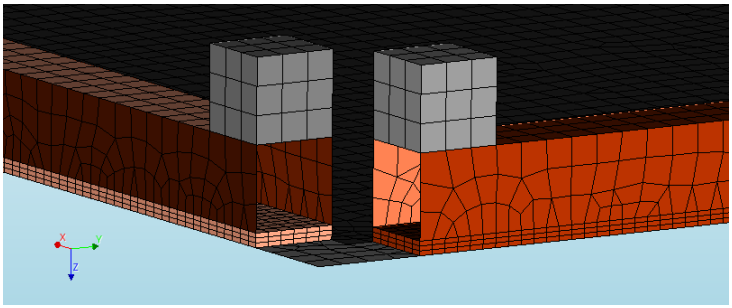

Figure 3.12: *The mesh used in the DIANA model for the simulation of the Cambridge experiments.*

Using a nonlinear analysis, the corners of the model are pushed down by 50 mm, and the force used to get to that displacement, taken from the reaction force at one of the supported corners, is used to compare the stiffness of the model to the results of the Cambridge experiments. The comparison can be seen in Figure 3.13. The results from Cambridge had to be corrected, as the graph starts at 35 mm displacement for 0 N load. However, Young (2019) states that the load applicators weighed about 2 kg each, so this should be included in the load. 20 N is added to compensate for this, but since the weight was not accurately reported, this might be a bit too high or too low.

The DIANA model has an initial phase of stiffening, but has a linear stiffness starting from around 10 mm displacement. We can see that this linear part of the DIANA model is almost a perfect match with the stiffness of the Cambridge experiment. Because this stiffness is the only thing we have to assess the quality of the model, and it matches the goal, we can consider this version of the model a success, and we can use what worked for this model to simulate the experiments for the experiments conducted later on in this research.

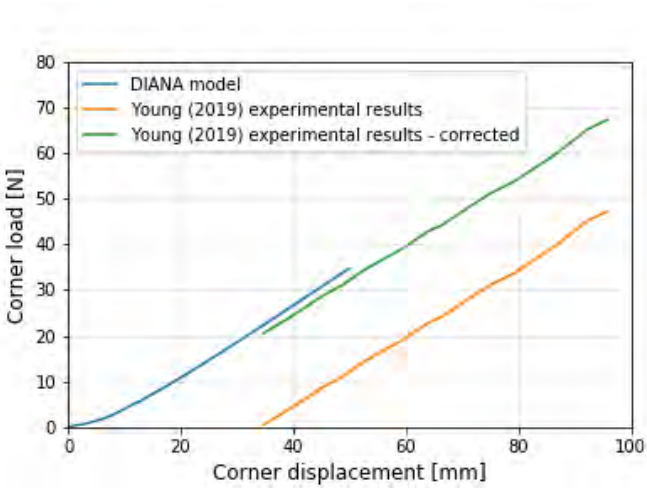

Figure 3.13: *The results of Young (2019) compared to the results from the DIANA model. The results from Cambridge show a displacement of about 35 mm at 0 N load. However, the weight of the load applicators, about 2 kg each, should be counted as a load. Therefore, the results are corrected by adding 20 N to the whole graph. The corner load is the load on one of the corners, not the total load applied.*

3.2.3 Full sandwich panel

Before we can start modelling the full sandwich panel, we must first make a choice on what material to use for the spacer that acts as the frame.

The spacer has two primary functions in the panel: to create a cavity between the inner and outer pane, and to stiffen the edge of the glass. These functions put requirements on the cross-section and the material that is used for the spacer, as it needs to be stiff enough to fulfil its role. Of course, a material with a lower stiffness could be used in combination with thicker walls to increase the bending stiffness, but this comes with a weight penalty.

Along with the primary functions, several other aspects of the spacer are considered: torsional stiffness, sustainability/recyclability, weight, and cost. Torsional stiffness is important since the glass performance increases when the edge is allowed to rotate. Therefore, a spacer with a low torsional stiffness is desirable.

For the spacer, GFRP, aluminium and steel are considered. In Table 3.7, estimated scores are given to these materials based on their performance in all the aforementioned categories.

Material	**Longitudinal stiffness**	**Torsional stiffness**	**Weight**	**Sustainabilty/ recyclability**	**Cost**	**Thermal insulation**
GFRP	0	++	++	-	0	+
Aluminium	+	-	+	+	+	-
Steel	++	- -	- -	+	+	–
Timber	-	++	0	++	++	++

Table 3.7: *Scoring of material options for the spacer. In this scoring matrix, higher longitudinal stiffness is considered to be better, while Lower torsional stiffness, weight, and cost are preferred. A material is considered more sustainable when it takes less energy to create, and more recyclable if it can be reused as a raw material at the end of its life cycle.*

From Table 3.7 we can see that steel is the least viable option. While it scores great in terms of stiffness, and also gets positive scores in cost and sustainability/recyclability, it is simply too heavy to be considered as a serious option.

On the opposite side of the scale, there is timber, which has the highest total score of all materials. However, on weight and longitudinal stiffness, the two most important aspects of the spacer, it scores worse than GFRP and aluminium. It also has a low strength perpendicular to the grain, so it may not be able to deal with the torsional loads that are induced by the shaping process. On top of that, the adhesive that is used may not work with timber, resulting in premature failure of the bond. Due to its great score in sustainability timber may be suitable for the design, but further research is needed to find the specific use cases in which the longitudinal stiffness and strength perpendicular to the grain are high enough, and the weight is less of an issue. A suitable adhesive also has to be found.

GFRP scores very positively on torsional stiffness and weight. Its main downside is the sustainability/recyclability score. While it takes less energy to create than steel or aluminium, it is harder to recycle, which is why it gets a negative score. The total score of aluminium is the same as that of GFRP. However, as mentioned before, weight is one of the most important factors in this design. GFRP scores better in terms of weight, so GFRP is considered to be the best option to use for the spacer.

Since the eventual experiments will be conducted with 1.5 $\times$ 1.5 m panels, the size of the previous model is adjusted. Several other elements are adjusted as well, but one thing could stay the same: the properties of the GFRP frame. The exact same profiles will be used for these experiments as the Cambridge experiment, so the dimensions (except length) and physical

properties can be copied. Further information about all materials of the panels are discussed can be read in Section 4.3.

Although a minor detail, it should be mentioned that the thickness of the silicone is increased from 5 mm in the previous model to the industry standard of 6 mm. The correct spacing to get this joint thickness is created by using Norton V2100 Thermalbond spacer tape. This spacer tape, with a Young's modulus op about 2.1 MPa, is placed along the entire inside edge of the frame, and because of its stiffness it is included in the model.

Two glass types are used in the experiments: 4 mm FT glass and 1.1 mm CT glass. The 1.1 mm glass is made with very low tolerances, and can be modelled as 1.1 mm thick. However, when ordering 4 mm glass, the thickness is actually 3.8 mm. This was confirmed when the glass was received by measuring with calipers, which showed that all the 4 mm plates were 3.8 mm thick. Therefore, it needs to be modelled as such. The glass plates are still modelled as 2D flat shell elements. The stress distribution over the depth of the glass is not of great importance, and this will save large amounts of computation time.

Dow has also created a document (Dow, 2018a) outlining the parameters to be used for the modelling of the silicone adhesive that will be used for the experiments: D993. These consist of the following Mooney-Rivlin parameters:

- $C_1 = 3.3306 \times 10^5$ Pa
- $C_2 = 8.6268 \times 10^3$ Pa

These parameters have been discussed in Section 2.5, so we know we can use them to model the silicone accurately.

The same loading blocks as before are used, because at the time of the creation of the model, the details of the experiments are not yet finalised. It will be attempted to match the design of the experimental set-up with the support and loading conditions created by the blocks.

The full model and a detail of the mesh can be seen in Figures 3.14 and 3.15. Four elements are used over the height of the silicone, one additional element at the cost of computation time.

Using a nonlinear analysis that includes geometrical and physical nonlinearities, the dead load is applied first in 20 steps. This makes the model more stable, and it mimics the way the experiments will be conducted. The weight of the load applicators is not included in this self-weight, so to compare the deformations of the model and the experiments, the equivalent weight first has to be put on the model.

The force-controlled load is applied in very small steps, with a maximum of 1% of the load per step. This is necessary in order for the model to converge between each step. If the step size is larger than this, divergence can occur quite quickly. This small step size, in combination with the large amount of elements and nodes in the model, unfortunately means long computation times of 6 to 8 hours for the full model.

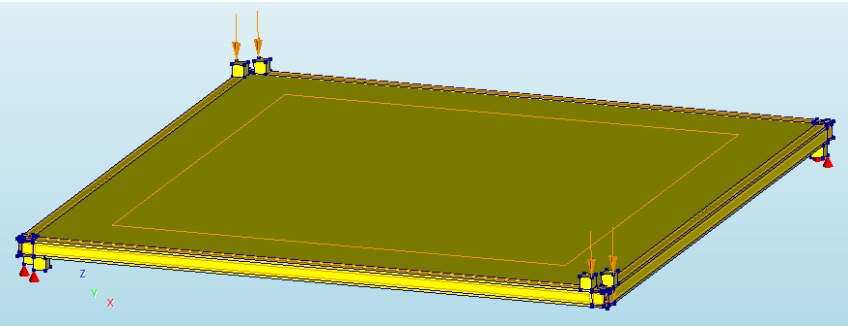

Figure 3.14: *DIANA model of the full sandwich panel, including loads and supports.*

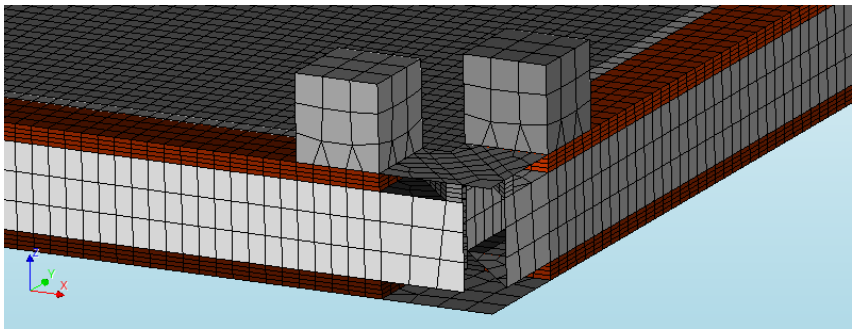

Figure 3.15: *Mesh detail of one of the corners. 4 elements are used over the height of the silicone, and the rest of the mesh is adapted to the silicone mesh size.*

3.2.4 Contact

From the results of the model, as well as the results from the experiments, it is clear that during the loading process, the top and bottom plate touch each other in the center. In order to model the stresses in the model over the course of the experiments, this contact has to be modelled.

The first option to model the contact was to make use of 'contact elements'. In an analysis with contact elements, one plate is given the 'contacter' role, and one plate is given the 'target' role. In theory, when the nodes of these two element types get within a certain distance, contact is established, and they will not pass through each other. To test if this works, a simple model is set up in DIANA with two plates touching in the middle (Figure 3.16).

With this simple model, it is already very difficult to get convergence once the plates get close. The settings for equilibrium iteration need a lot more adjustments than 'regular' models in order to get convergence. However, with the right settings and the right step sizes, it is possible to model the contact between the plates. To get the model to converge, the convergence norm is set to require both the force and displacement to satisfy the specified norms. The maximum number of iterations is increased from 10 to 50, and the solver is set to continue if there is no convergence. This does not solve divergence issues, but if there is no convergence, the solver may be very close to it. For example, if the convergence tolerance is set to 1%, which is merely conventional, and the solver reaches 2%, it is possible to go the next step without many (if any) issues. It is necessary to keep an eye on the convergence tolerance if convergence is not reached in a certain step, because if the result is too far off the tolerance, the result is incorrect.

Figure 3.16: *DIANA model used to try out contact elements.*

However, implementing these contact elements into the full sandwich panel is problematic. The additional contact sheets add thousands of extra elements and nodes, so the computation time increases, making it difficult to tweak the settings after running a failed analysis. On top of that, the necessary convergence seems harder to achieve with this model than the simplified version. This makes sense, as the full model was already sensitive to divergence. When contacting the DIANA customer service for advice, they mentioned that it is better to model the contact using other methods. The contact elements in implicit solvers like DIANA work best if there are large deformations due to the contact, which this model is not expected to have. A better way of modelling the contact would be to use interface elements or springs. Therefore, the simple model was adjusted to use nonlinear springs, as shown in Figure 3.17. Springs are placed along the center line of the plates. The plates are placed 50 mm apart, so the springs are defined in such

a way that for the first 49 mm of shortening almost no force is required. For the final 1 mm, the spring becomes practically infinitely stiff. This requires tweaking the settings once again, because if the transition from weak to stiff is too sharp, the analysis will diverge more easily. However, it is possible to get the same result from this model as with the contact elements. This concept is therefore implemented into the full sandwich panels, first in the 4 mm panel, then in the 1.1 mm panel.

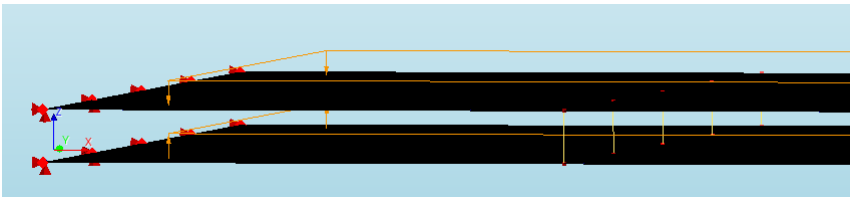

Figure 3.17: *DIANA model used to test springs as a way of modelling contact between plates.*

At first, a large array of 11×11 springs is used for the panel with 4 mm plates. However, when testing this it quickly becomes apparent that only the inner springs are actually working, as can be seen in Figure 3.18, so the array is reduced to 5×5. The spring stiffness is defined as a graph (Figure 3.19, with a smooth transition to help the analysis converge. After a lot of trial and error, the right balance between spring stiffness and step size is found to make the analysis converge.

The model of the 1.1 mm panel is too unstable to get useful data with the available computation power. In the final try, just the self-weight of the glass was added in 50 steps, but convergence was not reached after 33 steps, diverging at step 34. Since these 34 steps already took about 5 hours, and this should be the easiest, most stable part of the analysis, the model is abandoned in the interest of time.

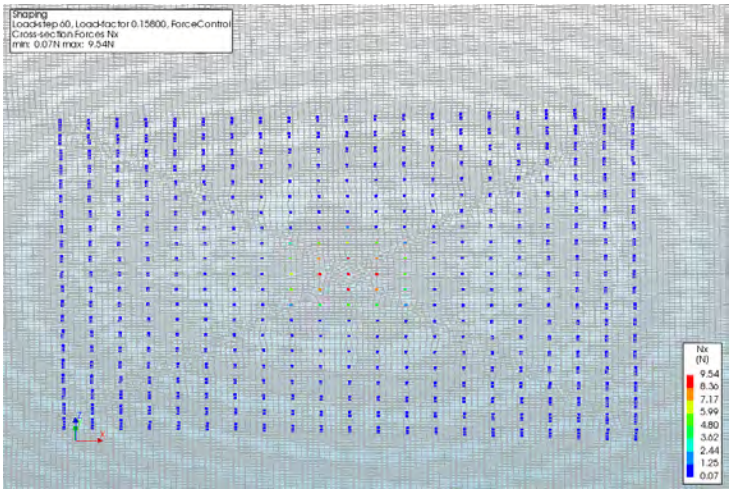

Figure 3.18: *Showing the full array of springs, but only the innermost springs are taking any load.*

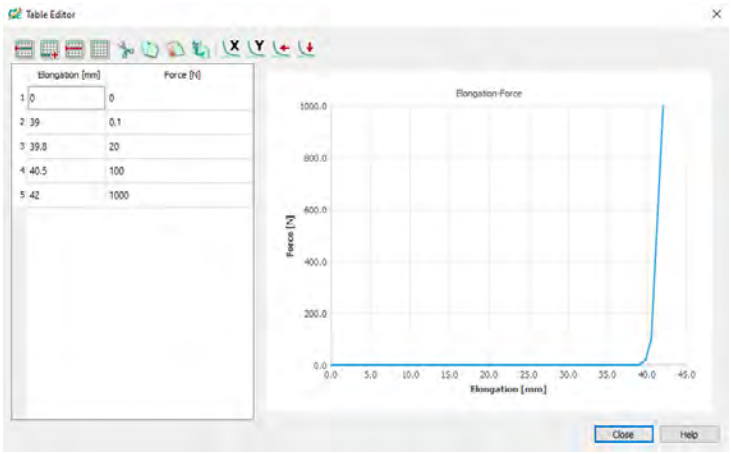

Figure 3.19: *Graph of the nonlinear spring stiffness used to model contact.*

3.2.5 Results

The results are presented in such a way that they can be compared with the experimental results. Since all measurements from the experiments are displacements and the applied loads, these will be the main focus.

The displacements along the loaded diagonal are the most critical results. Not only are these measured for all tests, but these give a good indication of the shape of the panel. If the center point of the panel has around half the displacement of the loaded corners, and there is a curve from loaded corner to loaded corner, the panel likely strongly resembles a hypar. If the center point has approximately the same displacement as the loaded corner, and the loaded diagonal is straight, then the panel resembles a single-curved plate more than a hypar.

Figure 3.20 shows the displacement of four key points along the loaded diagonal of the top plate of the model. The points are numbered in the same way as the experiments (Section 4.5), starting from point 1 in the corner to point 4 in the center (Figure 3.21). We can see in the graph that points 2, 3 and 4 have vertical displacement trajectories that are indistinguishable. The corner, though, is consistently around $10-15\%$ lower. This means there is a kind of plateau in the center region of the plate, while the corners are curved downwards.

All points start at a displacement of a little under 20 mm. This is because of the self-weight of the panel, the load trajectory of which is not included in the graph. Starting from that point, the stiffness of the panel is linear, until the point where contact is made between the plates. At that point there is a small drop in displacement, before the graph continues its linear trajectory.

The vertical displacement for the same points on the bottom plate are plotted in Figure 3.22. Here, we get some more insight into the behaviour of the model. Up until a corner load of around 400 N, the bottom plate bears more semblance to a hypar than the top plate. At 400 N, the corner has a displacement of around 75 mm, and the center point has a displacement of 50 mm, while a perfect hypar would have a center displacement of 37.5 mm at that corner displacement. The bottom plate is thus closer to a hypar than to a single-curved plate. Shortly after that point, the bottom plate shows the buckling phenomenon described in Section 2.3. The center points move up, and the corner points move down, indicating that the supported diagonal straightens. It is not fully straight, however, because the center points come into contact with the top plate. This change of shape is also the reason for the temporary decrease in stiffness of the top plate.

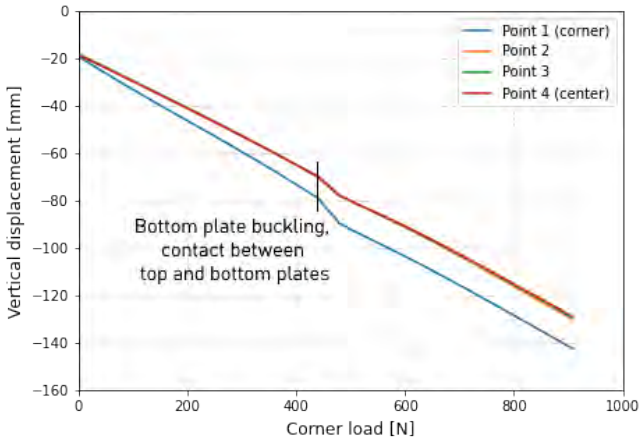

Figure 3.20: *The vertical displacements of four points on the top plate of the model, plotted against the corner load. Points 2, 3 and 4 have practically the same displacement trajectory, meaning the diagonal is almost straight, but the corner is lower throughout the loading process, so the plate curves towards the end.*

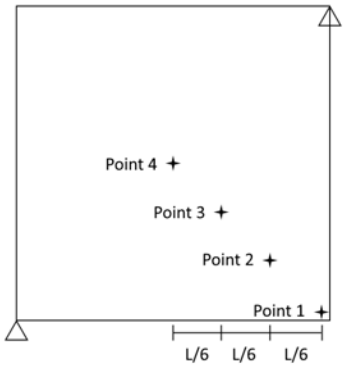

Figure 3.21: *Points numbering system in the results from the DIANA model. These numbers match with the numbering in the experiments. Points 1 and 4 match the location of the displacement measurements in the Cambridge experiments.*

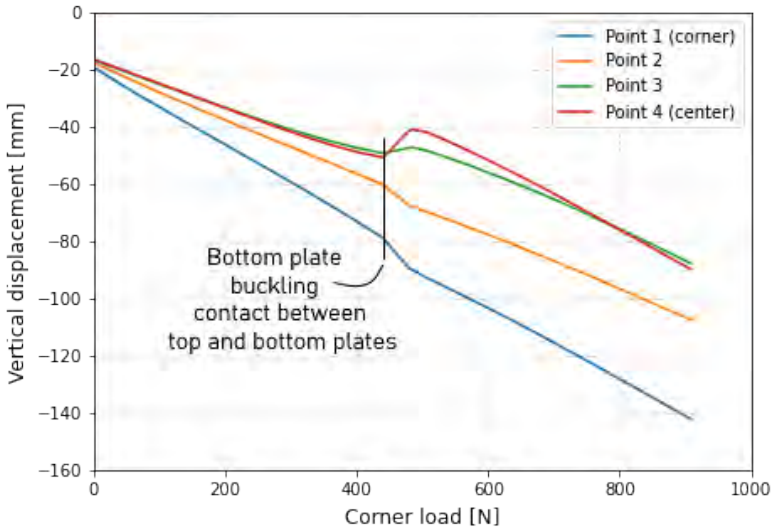

Figure 3.22: *The vertical displacements of four points on the top plate of the model, plotted against the corner load. The model is linear until a corner load of 400 N. At that point, the supported diagonal buckles out of plane, as shown by the upward movement of point 4, and contact is made between the top and bottom plates. The loaded diagonal keeps that shape as the load increases.*

3.3 Mesh study

Starting at the model that simulated the Cambridge experiments, it was found that the silicone material model and mesh size was the most impactful element of the whole model. To get accurate stresses and deformations in the model, a mesh study is performed with the silicone adhesive layer isolated.

An arbitrary, 'infinite' for all intents and purposes, length of silicone is modelled, with the full width and height of the joint in Paragraph 3.2.2, i.e. 30×5 mm. Five models are placed next to each other, as seen in Figure 3.23, with an increasing amount of linear mesh elements over the height, running from one to five. The Mooney-Rivlin material model is used, with the parameters from Paragraph 3.2.3. The bottom of each silicone 'slab' is fixed in all directions, and a displacement controlled load is put on the top. Tests are done in compression and tension.

In Figure 3.24, it can be seen that the possibility for hourglassing is strongly impacted by the amount of elements over the height. When there is only one element, the hourglass shape cannot be formed, which also results in the stresses being practically infinite. The stress trajectory for the top center element of all meshes is plotted in Figure 3.25. In both tension and compression it is clear that there is a large difference in stress between 2 and 3 elements. From 3 to 4 there is still a difference of about 4% in the tension graph, and 6% in the compression graph. The difference between 4 and 5 elements is negligible. Because the difference between 3 and 4 elements is so small, while the implications on the computation time will be very big, the use of 3 elements over the height of the silicone joint is deemed acceptable. The stress will likely be slightly overestimated because of this.

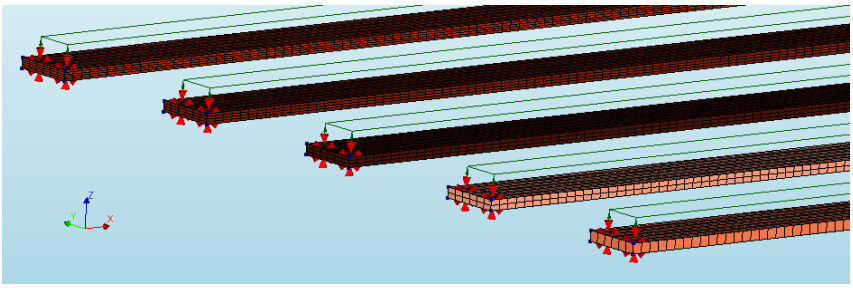

Figure 3.23: *DIANA model used for the mesh study. The five mesh sizes are modelled next to each other for easy comparison.*

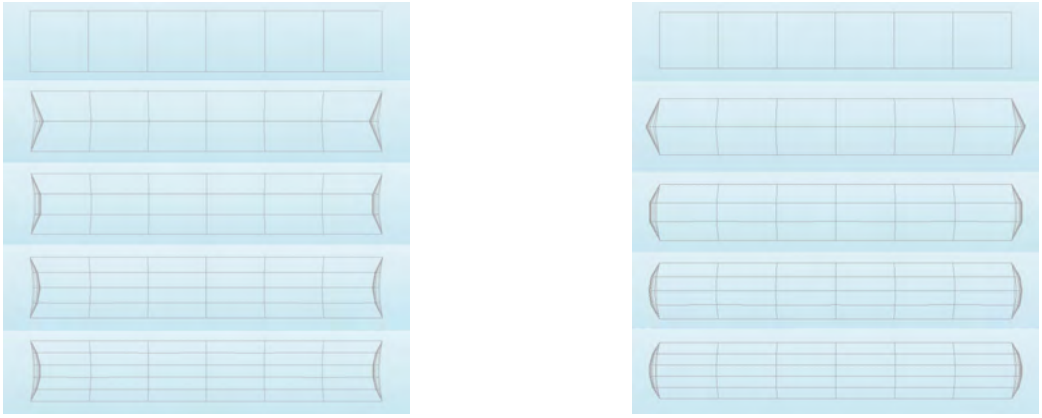

(a) *Different mesh sizes in tension.* (b) *Different mesh sizes in compression.*

Figure 3.24: *Mesh size comparison for the silicone adhesive layer.*

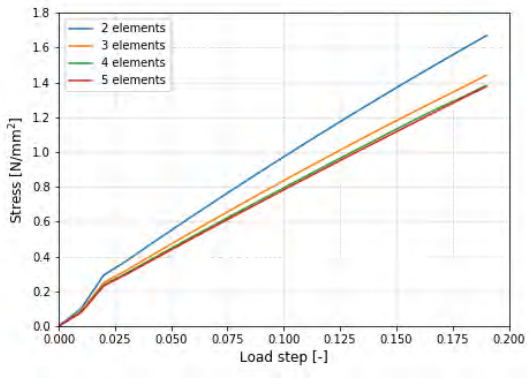

(a) *Stress trajectory at the top center element in tension.*

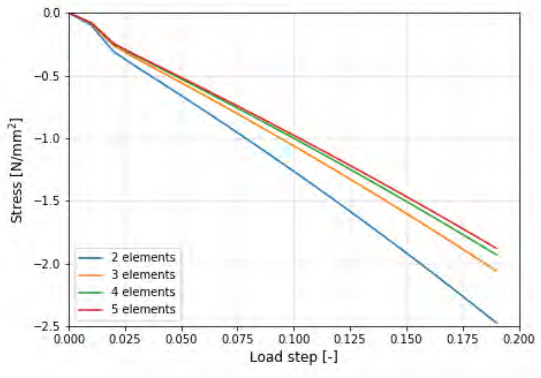

(b) *Stress trajectory at the top center element in compression.*

Figure 3.25: *Stress trajectories for the different mesh sizes of the silicone mesh study.*

3.4 Internal pressure

As part of predicting how the panels behave, it is helpful to have a way of predicting the behaviour under external load in a building application. It was explained in Section 2.4 that the panels are made airtight after shaping. A low flow rate valve is installed, so the inner and outer leafs can work together in taking up short-term loads, such as wind or impact loads. For the purpose of the load calculations, the panel is considered airtight.

In case of an external load, e.g. a wind load against the outer leaf, the volume of the cavity decreases. In response, the pressure in the cavity rises according to Boyle's law. This results in a distributed load against the loaded outer leaf, but also a load of the same magnitude against the spacer and the inner leaf. Again in response, the inner leaf bulges out, and the outer leaf gets pushed back. In theory the spacer moves as well, but because this deformation is assumed to be small, it is neglected. In practice, this change of shape of the glass and the subsequent change of volume and pressure of the cavity happens very quickly, and equilibrium between the components is found nearly instantly. However, when calculating the displacement of both leafs for which the wind load, internal pressure and deformation of the glass are all in equilibrium, an iterative process (Figure 3.26) is likely necessary.

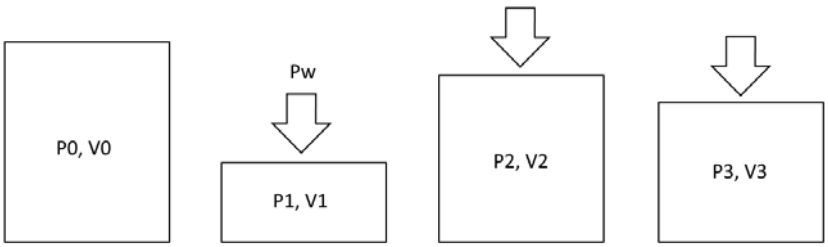

Figure 3.26: *Schematic of a converging algorithm. The box represents the volume inside the cavity. Wind pressure P_w is applied and the box deforms. Through iteration, the volume and pressures converge to the correct solution.*

Examples exist in literature on how to calculate cavity pressure due to wind loads. For example, the Dutch Building Decree NEN 2608 (2014) has a series of formulas to calculate cavity pressure for IGUs. Other examples include Feldmeier (2003), which is widely used for wind and climatic loads, but assumes an initially flat IGU, Galuppi (2019), which requires prior calculation the stiffness of the bent IGU, and Marinov (2012), which requires FEA to determine

the stiffness of each individual leaf of the IGU. These example all either require the panel to be flat, or require the use of a FE-model. Since a FE-model has to be created anyway, an iterative approach is designed, with the aforementioned sources in mind, to use the model to find the correct equilibrium between the pressures.

3.4.1 First version

A first version of the algorithm is created using the FE model. Using a nonlinear static analysis, a unit wind load is applied to the outer leaf, with the assumption that there is no internal (over)pressure. Once the wind load is applied, the change in volume is calculated using the script shown in Appendix D. With the new volume, the change in pressure is calculated using Boyle's law:

$$P_0 V_0 = P_1 V_1 \tag{3.3}$$

Where P_0 is atmospheric pressure (approx. 10^5 Pa), V_0 is the internal volume of the cavity of the unloaded panel, and P_1 and V_1 are the pressure and volume after loading. This newly calculated pressure P_1 is always higher than P_0, because $V_1 < V_0$. The overpressure $(P_1 - P_0)$ is applied to the inside of the deformed cavity. After the load is applied, the newly formed volume V_2 is compared again to P_0 and V_0:

$$P_0 V_0 = P_2 V_2 \tag{3.4}$$

This process would continue until the volume and pressure had converged into an equilibrium. However, when this method was applied, the solution always diverged. The second calculated volume (V_2) would always be larger than V_0, resulting in a negative overpressure (i.e. a pressure lower than atmospheric pressure) P_2. This would then lead to a V_3 that was smaller than V_1, thus diverging instead of converging, as shown in Figure 3.27.

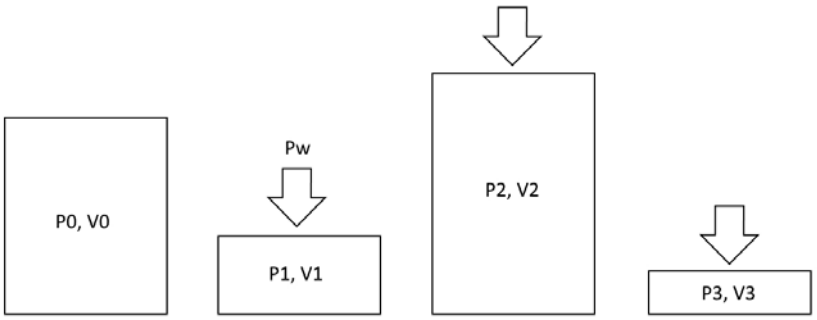

Figure 3.27: *Schematic of a diverging algorithm. The box represents the volume inside the cavity. Wind pressure P_w is applied and the box deforms. Because of the overpressure, $V_2 > V_0$, which leads to the model diverging.*

3.4.2 Second version

To solve the problem of V_2 being larger than V_0, only part of the overpressure is applied to the inside of the cavity. The process starts the same as before, so a wind pressure is applied on the cavity with the assumption that there is no internal pressure. The new pressure is then calculated using Equation 3.3. Then, instead of the full overpressure, only part of the overpressure is applied to the inside of the cavity, i.e. $C \cdot (P_1 - P_0)$ with $0 < C < 1$. When C is small enough, V_2 will be smaller than V_0. If the iteration is continued from there, the algorithm will converge to a certain volume and find equilibrium between the pressures.

However, even though there is convergence, this method is not the solution. The volume that the algorithm will converge to depends on the C that the overpressure is multiplied with. If C

is smaller, the algorithm will converge to a smaller volume than it would with a larger C. If the iteration has converged and the rest of the overpressure is applied in steps that converge, eventually there will come a step that results in a higher volume than V_0. This occurs before the full overpressure has been applied. The end result is that the algorithm always diverges in the end.

3.4.3 Third version

The seemingly random convergence volume that depended on the arbitrarily chosen C from the last version is the basis for this third version of the iteration algorithm. If a random pressure is applied to the cavity after the wind load has been applied, the algorithm will either converge to a random volume (directly related to the chosen pressure), or diverge. So what would happen if one were to guess the equilibrium pressure, and it happened to be the correct one?

An educated guess for the equilibrium pressure can be made by using the method for calculating the cavity pressure from the Eurocode (EC). The NEN2608 provides a method of calculating the cavity pressure for rectangular double glazing units loaded by wind. By using this set of formulas we can calculate the cavity pressure of the flat (not cold-bent) panel of the correct panel dimensions. Using this, we can determine if 'guessing' tactic works. Once that has been established, the EC formulas can be used to make an estimated first guess to calculate the cavity pressure for the deformed (i.e. cold bent) panel. Though it must be said that we can already expect that the equilibrium pressure of the FE model will never match exactly with the outcome of the EC formulas. For example, the EC formulas do not take the stiffness of the adhesive and the spacers into account. However, if the model is reasonably close to representing the real panel, the EC formulas will provide a good educated guess.

When inputting 'guessed' pressures into the model, the same method is followed as before. Wind load is applied, the volume changes, and the guessed pressure P_g is applied to the cavity (Figure 3.28). The cavity subsequently expands, and the resulting pressure P_2 is calculated with P_0 and V_0. Here, an interesting observation is made. When the P_g is lower than the pressure from the EC formulas (P_{EC}), the calculated P_2 is higher than P_{EC}, and vice versa. What's more is that there is a linear relationship between P_g and P_2.

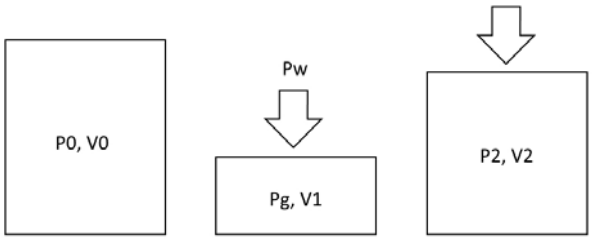

Figure 3.28: *Schematic of a diverging numerical model. The box represents the volume inside the cavity. Wind pressure P_w is applied and the box deforms. Then, an estimated guess for the equilibrium pressure is applied, and the resulting volume is used to calculate the new pressure.*

Remembering that we want to create a method of guessing the equilibrium pressure in the first try, in order to avoid convergence to a random point or divergence, we can use the linear relation between P_g and P_2, which we will call P_r for 'resulting pressure', to get to the correct pressure. To do this we use a three-step iteration. First, we use the P_{EC} to make a first estimation of the pressure ($P_{g,1}$). Using this we calculate $P_{r,1}$. If $P_{r,1}$ is higher than $P_{g,1}$, the first guess was too low, so our second guess should be higher, and vice versa. The magnitude of the second guess ($P_{g,2}$) is not critical, but to make sure the results are robust and to avoid very large deformations of the glass, it is a good idea to have $P_{g,2}$ within about 10% of $P_{g,1}$. Because there is a linear relation between P_g and P_r, we can use the results from $P_g, 1$ and $P_g, 2$ to draw a line on the P_g vs P_2 graph. Because we want our guess pressure to be correct, we can simply choose our $P_g, 3$

to be the pressure where the drawn line crosses the line for $P_r = P_g$. This final $P_{g,3}$ should be the equilibrium pressure for the FE model.

3.4.4 Example

To test the algorithm, a simple model is set up. The double glazed panel is modelled using parameters that are set up to aid computation time. These parameters are not entirely accurate for modelling the real-life panel. However, the parameters (mainly mesh size) should only affect the stiffness of the model, and can still be used as a proof of concept for the algorithm. It would be the same as modelling a panel with slightly thicker glass and stiffer silicone, for example.

The modelled panel 3.29) is supported on all sides, and a wind load of 1 kN/m^2 is applied in the normal direction of the top pane, so it will move inwards, decreasing the cavity volume. To avoid meshing problems, the corners of the GFRP profiles and the silicone are cut off. Again this will only affect the stiffness of the glass, not the fundamental working of the model. Only two solid brick elements are used over the height of the silicone. This will result in a silicone joint that is too stiff, but will save large amounts of computation time.

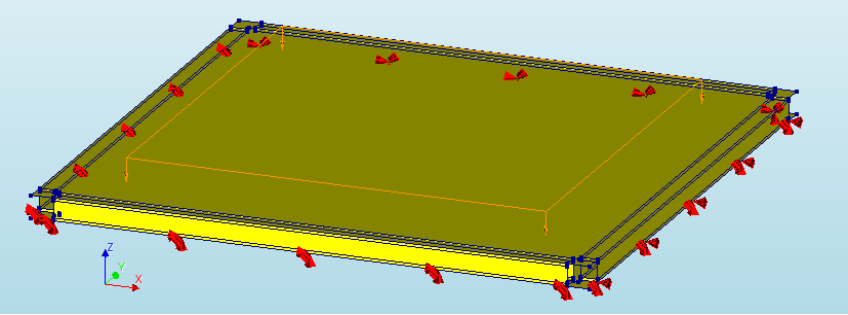

Figure 3.29: *The finite element model used as an example for the cavity pressure algorithm. The model is supported on all sides, and a wind load is placed on the top pane.*

With the EC formulas, the first guess pressure, $P_{g,1}$ is calculated. The input parameters are the following:

- Panel length: a = 1000 mm;
- Panel width: b = 1000 mm;
- Cavity depth: s = 40 mm;
- Top pane thickness: $t_{blad;1;ser}$ = 4 mm;
- Bottom pane thickness: $t_{blad;2;ser}$ = 4 mm;
- Wind load: p = 1 kN/m^2.

Through a series of formulas from NEN 2608 (2014), which can be found in Appendix E, we can calculate $P_{EC} = 478.0$ N/m^2, which we use as a our first guess, $P_{g,1}$. The wind load is applied using a nonlinear static analysis, after which $P_{g,1}$ is applied. Using Boyle's law (Equation 3.3), the resulting volume $V_{r,1}$ is used to calculate the corresponding pressure $P_{r,1} = 365.6$ N/m^2. This $P_{r,1}$ is lower than our first guess, which means the first guess was too high. The second guess will be made by lowering the first guess by 10%. This gives $P_{g,2} = 0.9 \cdot P_{g,1} = 430.2$ N/m^2. Applying $P_{g,2}$ to the model leads to a pressure of $P_{r,2} = 658.9$ N/m^2 after the aforementioned steps are taken.

Since we know the relation between $P_{g,i}$ and $P_{r,i}$ is linear (shown in Figure 3.31), we can trace a line through the calculated points. This line can be described using the equation:

$$P_{r,i} = -6.1353 \cdot P_{g,i} + 3298.3 \tag{3.5}$$

Because we want our first guess to be the correct one, we want $P_{r,i} = P_{g,i}$. Therefore we want to find the point where Equation 3.5 intersects with $P_{r,i} = P_{g,i}$. This is a simple equation to solve, and results in $P_{g,3} = 462.3$ N/m^2. Putting this through the model results in $P_{r,3} = 461.4$, which differs less than 0.2% from $P_{g,3}$ N/m^2. From this, we can conclude that the three-guess-algorithm has worked.

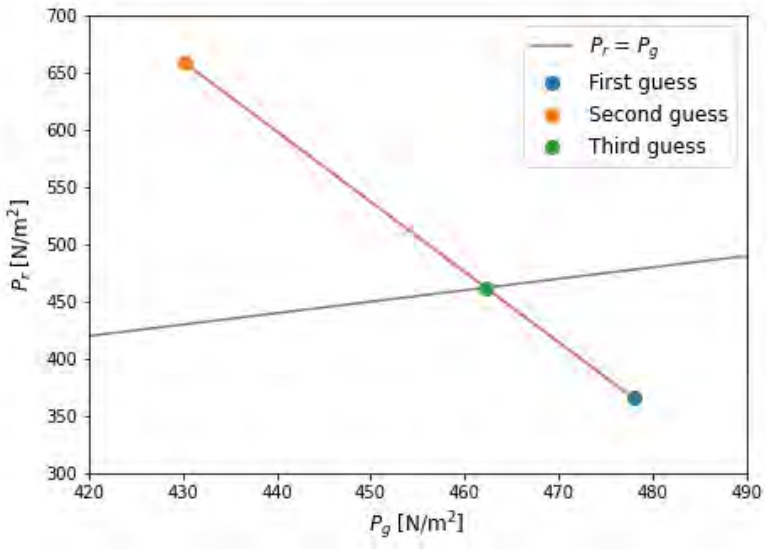

Figure 3.30: *The intermediate steps of the cavity pressure algorithm visualised in a graph. On the horizontal axis, the input or 'guess' pressures (P_g, for 'guess pressure') are plotted. The vertical axis shows the pressure that is calculated from the volume that is created with the guess pressure. This is called P_r for 'resulting pressure'. The first and second guess are made based on existing formulas, and the third and final guess is based on the intersection of the line between the first and second guess, and the line $P_r = P_g$.*

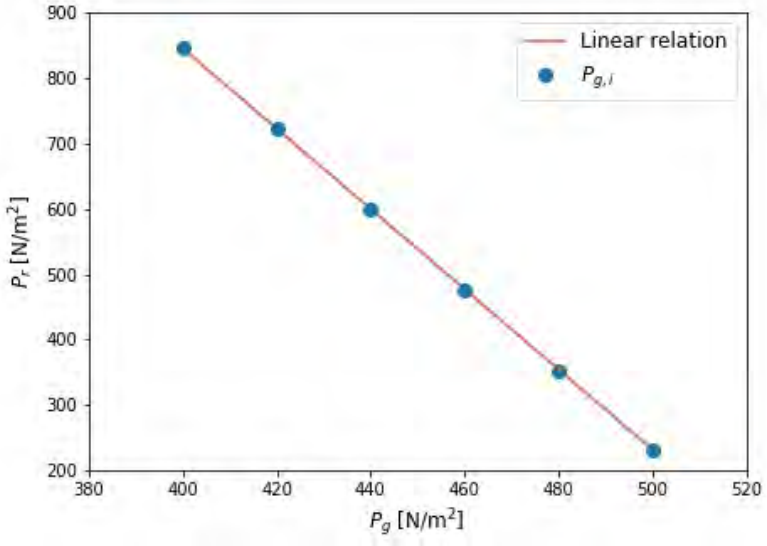

Figure 3.31: *Demonstration of the linear relation between P_g and P_r, where a series of guess pressures P_g were put on the model in 20 N/m^2 increments, and the P_r was calculated.*

4

Experiments

4.1 Goal

The experimental set-up should be designed so that the boundary conditions of the numerical model are matched. The numerical model was set up to create the scheme shown in Figure 4.1. When these conditions are applied to a regular plate, they should lead to a hypar when the load is applied, as discussed in Section 2.3. Of course, the specimens that are tested are not regular plates, and as such will likely diverge from the perfect hypar shape. This was already predicted in the numerical model, but the tests performed with this set-up will have to provide a definitive answer.

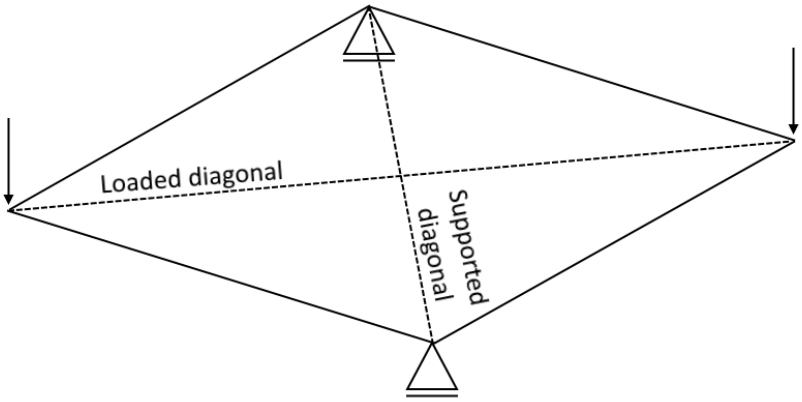

Figure 4.1: *Schematic representation of the ideal support and loading conditions for the experiments.*

In order for the experimental set-up to recreate the conditions from Figure4.1, there are several requirements:

- Supports must only take up vertical load;
- Load must be perpendicular to the surface of the glass;
- Global rotation of the panel must be prevented.

When designing the experimental set-up and its components, these requirements should be kept in mind.

4.2 Set-up

As a starting point for the set-up, we can look at the experiments done by Young (2019), since those essentially have the same starting points, and the same boundary conditions applied. However, before we actually start analysing what to use and what not to use from those experiments, we should ask ourselves if we should take the same approach as Young (2019).

In the Cambridge experiments, as well as other similar experiments such as the first series done by Staaks (2003), the choice was made to perform the experiments with the panel lying horizontally and applying the load vertically. The experiments don't have to be performed like

this. It's also possible to start with the panels in vertical position and apply the load horizontally. This way, gravity doesn't impose an out-of-plane load on the glass. This may be advantageous for the buckling behaviour of the panels, as the out-of-plane load already causes the loaded diagonal to flatten.

Despite this, the choice is made to perform the experiments for this thesis horizontally. As stated before, the main goal of the experiments is not to create a curvature or deformation that is as large as possible, but to verify the numerical model. One of the first and most crucial steps in building up the model was to simulate the Cambridge experiments, which were performed horizontally. In order to be consistent, to be able to compare the results of various experiments, and to expand the numerical model as progressively as possible, the experiments in this research are done horizontally.

4.2.1 First draft

The initial design for the experimental set-up is based on the previously mentioned set-up from the Cambridge experiments (Figure 4.2). This set-up uses steel rollers (Figure 4.3) as supports, with wooden brackets to prevent global rotation of the panel. These wooden brackets were added after the initial test, because the panel rotated and fell of the supports, breaking the glass. Therefore, preventing rotation is important. The load is introduced via a steel portal-frame with hydraulic jacks. polytetrafluoroethylene (PTFE or teflon) load transfer blocks (Figure 4.4) are placed on the corners, with which the load is transferred from the jacks to the panel. On top of the frame, PTFE plates are positioned, on top of which the load blocks are placed. PTFE has a very low coefficient of friction of 0.04 (Walker, 2004), so no horizontal loads are introduced, and the load is almost perfectly perpendicular to the surface of the frame.

Figure 4.2: *The final version of the set-up used for the experiments by Young (2019).*

Figure 4.3: *One of the roll supports used in the experiments by Young (2019).*

Figure 4.4: *A loading block used in the experiments by Young (2019).*

Since the experiments done for this thesis are very similar to those done in Cambridge, the initial design for the set-up is very similar as well. In Figure 4.5 an overview can be seen. Two load applicators are used, one for each corner, which are both attached to a portal frame that is placed over the panel. The load applicators can be either hydraulic or manual (e.g. with threaded rods), and load cells are used between the panel and the applicators to measure the applied loads. Temporary supports are used underneath the loaded corners while preparing the panel for a test. This way, a proper zero-measurement can be taken with the panel in its flat, unloaded state.

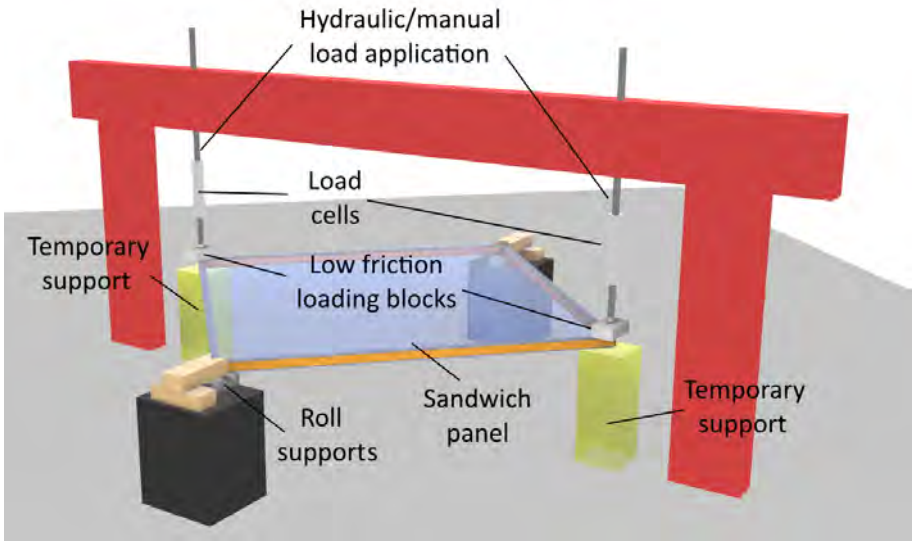

Figure 4.5: *Initial design of the experimental set-up using a portal frame to introduce the load from above.*

Unfortunately, after discussing this set-up with the technicians at the Stevinlab, a few issues have become clear that prevent the set-up from being used as designed. First, the space around the set-up is limited, and the portal frame would take up too much space, both in footprint and in height. Second, the budget for the set-up is relatively low, and building the set-up as it was designed will likely be too expensive. It will require costly time to build it up, as well as costly new parts that need to be manufactured. Finally, the only available jacks that have the amount of travel required are very large and very heavy, making the set-up even larger. For these reasons, a revised design is made for the set-up.

4.2.2 Revised set-up

The final version of the set-up uses a more compact design. Instead of a portal frame above the panel, the load is introduced from underneath. In Figure 4.6, we can see a 3D drawing of the set-up.

Located on the bottom left of the image, there is a hydraulic cylinder, powered by a manual pump. This cylinder is what provides the force. Through a mechanism of steel bars, the displacement of the cylinder is transferred to two steel cables, one for each corner. Each cable is then fed through two pulleys to change its orientation from horizontal to (near) vertical. Note that Figure 4.6 does not show the final version. In the final version the supports are placed on taller blocks to allow for more travel of the loaded corners (Figure 4.7), and to decrease the angle at which the cable arrives at the corner. A load cell is placed in the horizontal part of each of the two cables.

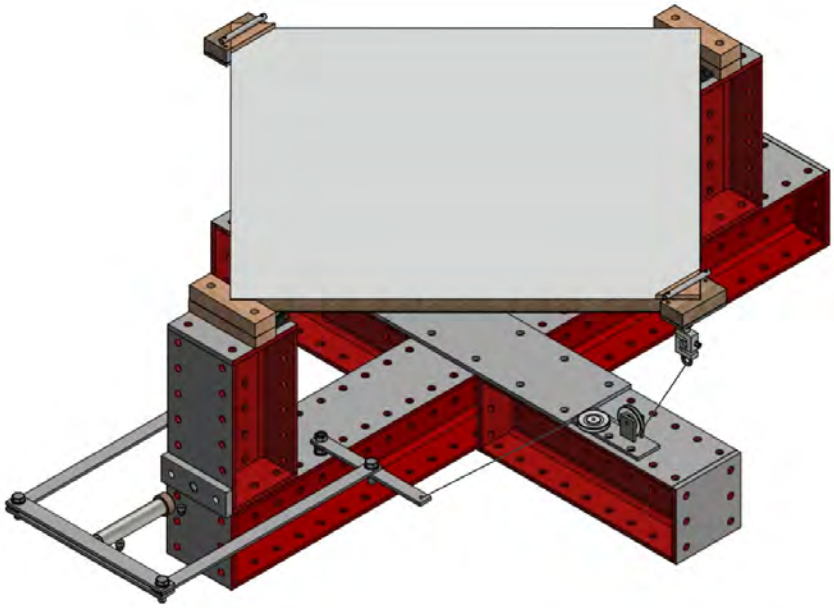

Figure 4.6: *3D drawing of the revised version of the experimental set-up. In the final version, the supports are placed on higher blocks, and the load cells are placed in the horizontal parts of the cables, not at the corners of the panel.*

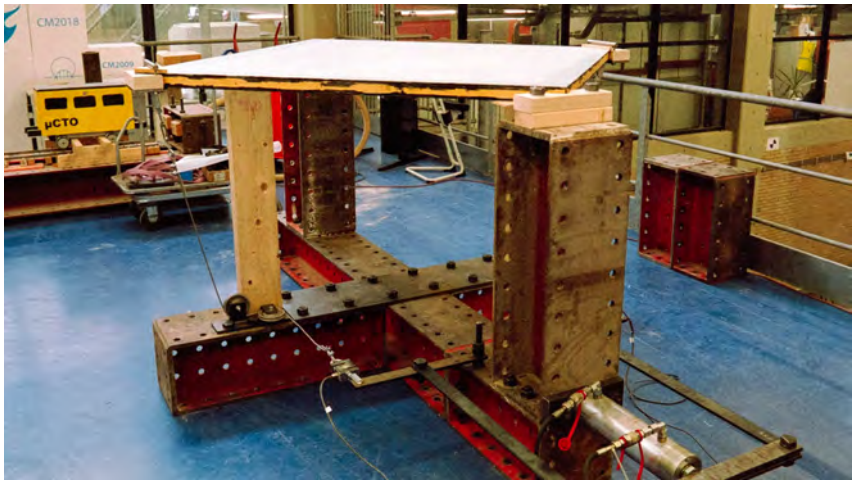

Figure 4.7: *Picture of the final set-up (including higher support blocks) with one of the panels in place. The panel is still supported by the temporary supports.*

The supports for the 4 mm panels (see Section 4.3 for more information about the two panel types) are shown in Figure 4.8. This support was designed to support the glass through the largest amount of surface area for the longest time. The rounded steel block with a stiff rubber pad on top created a sturdy surface that could move slightly under load. The piece of multiplex served to create a larger surface area on which the frame could rest, and which could also flex under load.

The supports were altered for the 1.1 mm panel, to avoid any 'free' part of the glass taking up any load. In Figure 4.9 it can be seen that a large piece of thick felt was used. In all the possible deformations resulting from the corners moving downwards, the piece of glass in the center of the support would either stay flat or move upwards, with both cases leaving (almost) all of the load to be supported by the frame.

Figure 4.8: *Support for the 4 mm panels. A steel block with a rounded top, a thick rubber pad and a piece of multiplex created a flexible support to spread the load.*

(a) *Front view.*

(b) *Side view.*

Figure 4.9: *Supports for the 1.1 mm panels, using a thick felt pad on top of a steel line support.*

The load has to be applied from the top, so the corner detail (Figures 4.10 and 4.11) is designed to transfer the load from the cable on the bottom of the panel to a steel rod on top. The cable is attached with a hinge to the steel bottom plate of the corner detail. The load then travels through two threaded rods from the bottom plate to a cylindrical steel rod. This rod applies the load to the top of the panel, with soft material in between to prevent high local stresses. In between the bottom plate and the steel rod is a timber block with a 90° cut-out to keep the corner detail in place.

Something to note is that when the panel is undeformed (flat), the cable arrives at the corner at an angle of around 12°. This is because when the panel deforms, the corner slowly angles

downward, which can be seen in Figure 4.31. If the cable is attached vertically, the corner detail has the possibility of slipping off, because the load has a component away from the corner. Since the angle is the greatest when the load is zero, and the angle becomes smaller when more load is applied, the horizontal component of the load is never very large. More on this in Paragraph 4.5.

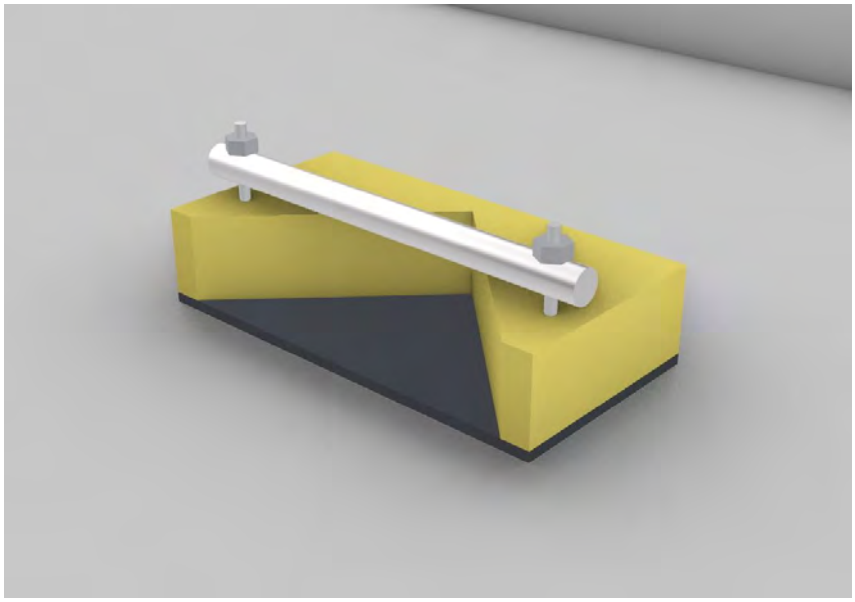

Figure 4.10: *The corner detail used to transfer the load from the cable to the top of the panel. The cable is attached to the steel bottom plate of the detail. Two threaded rods go through the bottom plate, a timber block with a corner cut-out, and through an steel rod. The timber block makes sure that everything stays in the right orientation. The steel rod is placed on top of the glass, with some soft material in between to prevent high local stresses.*

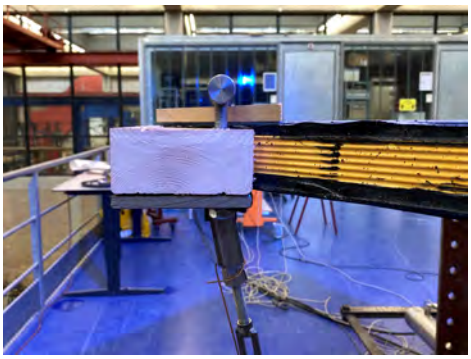

(a) *Side view.*

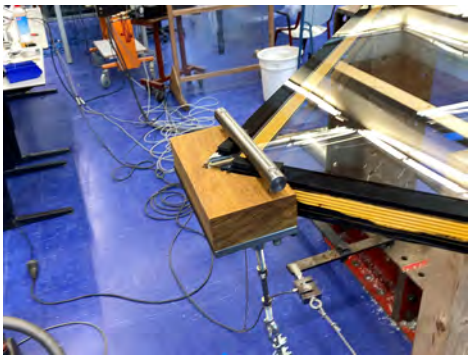

(b) *Perspective view.*

Figure 4.11: *Two images of the physical corner detail. Note that the two images are not of the exact same detail. Subfigure 4.11a is the one used in the first test, after which the detail was altered slightly. The timber block was replaced and rubber was used instead of medium-density fibreboard (MDF) between the steel rod and the glass, which can be seen in Subfigure 4.11a.*

4.2.3 Measurements

To verify the model, measurements needed to be made that could relate the experiments to the FE-model. The amount of instruments that could be used was limited, as each additional instrument or sensor (type) would add man hours for the technicians, which would add costs while the budget was already mostly used up for the designing and making of the base set-up. In addition to that, some instruments were already in use for higher-priority projects and thus could not be used for some or all of the experiments for this research.

Two quantities were at the core of the measurements: force and displacement. If these two quantities are measured, the global behaviour of the FE-model can be verified. If the global behaviour is correct, it is probable that forms of local behaviour, such as local stresses and and deformations, are at least somewhat close to reality.

In all four tests, the applied force was measured at the loaded corners. To be more specific, the applied force on each loaded corner was measured with a load cell (Figure 4.12) that was placed in the horizontal part of the cables. Because each cable went through two pulleys, there were some losses because of friction, but because the pulleys had internal bearings, these losses can be neglected. In addition, the cable itself was not infinitely stiff and would elongate under load. However, the elongation of the cable at maximum load was estimated to be less than 2 mm, the loss of the load was less than 1% and is therefore also neglected.

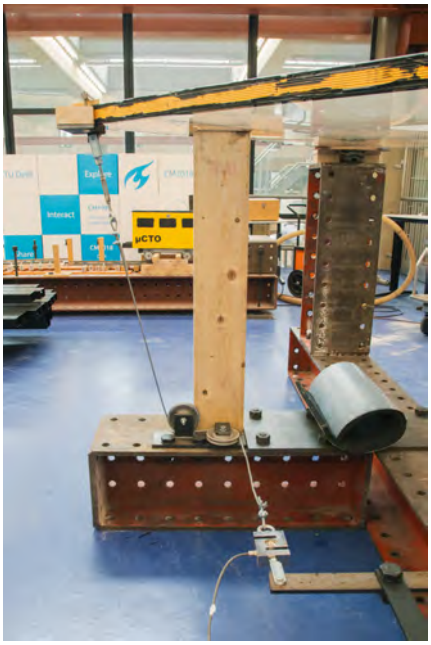

Figure 4.12: *The path of the cable with which the load was applied. The load cell can be seen on the bottom right of the image, where the cable starts. The cable then goes through two pulleys to change it direction, and finally it attaches to the corner of the panel.*

The displacement of the corners was measured using displacement sensors in the form of linear variable differential transformers (LVDTs) with wire gauges. The sensors were attached to the pulleys, and the end of the displacement gauges were attached to the corner details (Figure 4.13) , so the wire gauges were in line with the cables. In this way the displacement of the corners was directly measured, and the elongation of the cables did not have to be taken into account. It should be noted that these LVDTs arrived at the corners at an angle, so to get the vertical displacement, the data would have to be corrected in post-production.

(a) *Full view of the load cable, pulleys, LVDT sensor and the wire gauge attached to the panel's corner.*

(b) *The LVDT sensors were clamped to the pulley so that the wire gauge came out as close to the cable as possible.*

(c) *Wire gauge attached to the corner detail. A simple hook was made with a metal to attach the wire gauge.*

Figure 4.13: *Several views of one of the LVDTs used to measure the corner deflection. Note that in subfigures 4.13a and 4.13b the cable had not been tightened yet, and was therefore not parallel with the LVDT's wire gauge.*

The displacement was not just measured at the corners, but attempts were made to measure the displacement of the entire panel. During the period of the first test, a camera system designed for 3D digital image correlation (DIC) was available. This system, shown in Figure 4.14, uses two cameras to form a complete three-dimensional displacement field. For the software to recognise the evaluated surface, it needs to be covered in a random speckle pattern. The software then uses the deformation of the speckles to determine the deformation of the surface. Only one camera system was available. With the cameras, it was not possible to get the whole panel in view from underneath, so it was obvious to choose the top of the panel to measure.

Figure 4.14: *The* GOM ARAMIS Adjustable *camera system used for the 3D digital image correlation.*

Through the deformation of the speckle pattern, the 3D DIC can also be used to visualize strains in the measured surface. However, the cameras had to be quite far away to get the whole panel in view. Because of this, the size of the speckle pattern was fairly small for the resolution of the cameras. Therefore the results were likely to not be very accurate, especially the magnitude of the strains.

Because the cameras could only see the top of the panel and it was preferred to have some information about the behaviour of the bottom panel as well, a displacement sensor (Figure 4.15) was placed underneath the panel. This sensor consisted of a spring-loaded LVDT with a travel of 100 mm. The tip was positioned so that it just touched the center point of the bottom panel. As the center of the panel would move downwards, the sensor would be pushed in and measure the displacement. However, the with the numerical model it was predicted that the center would move more than 100 mm downwards, so during the test it was important to pay attention to the sensor. When it would get near the maximum travel, the sensor would have to be removed.

For the remaining tests, the 3D DIC camera system was not available. To get an idea of the displacement in other places than just the corners, a 2D DIC system was created. This was fairly straightforward, because GOM - the company that makes the DIC software - also makes black and white dots in different sizes, which can be recognised by the software. These dots were placed on small thin wooden strips at several locations. Since the experiments had been set up to create a hypar shape in the panels, the dots were placed along the loaded diagonal. This positioning gave the possibility to evaluate the hypar shape, because the straightening of the loaded diagonal determines how closely the deformed panel matches a hypar. Had the dots been placed along the supported diagonal, it would have been possible to say whether or not a hypar had been formed, but the evaluation of how closely it matched a hypar would be more difficult.

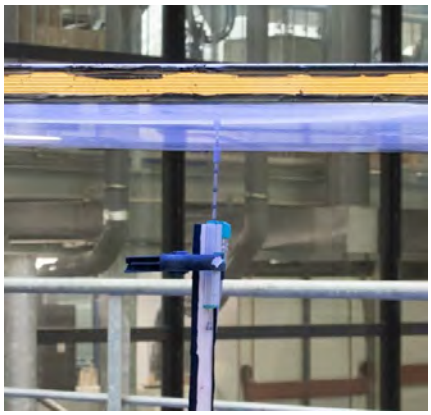

Figure 4.15: *The LVDT used to measure the displacement of the bottom panel during the first test.*

Regular DSLR (Digital Single Lens Reflex) cameras were used to take photos at specific time intervals. The first test using this 2D DIC only one camera was available, so to be able to compare the 3D and 2D DIC results, the top panel was measured. For the final tests, two cameras were available, so both the top and bottom were measured. It was impossible to get the whole bottom of the panel in view since a part of the set-up would always be in the way. Therefore the choice had to be made to either get the whole bottom of the panel in view except for the center part, or get half of the bottom in view, including the center. Since the deformation had shown to be symmetrical, both from the numerical models and the previous tests, it was chosen to look at half the panel, so a measurement could be taken at the center of the panel.

The final measured quantity was the shear in the adhesive layer. The behaviour of the silicone was very important for the global behaviour of the panel, so it was important to get some measurement to verify the FE modelling approach. This was done with a simple setup of two LVDTs, one for the top of the panel and one for the bottom, as shown in Figure 4.32. They were placed approximately 40 cm from the supported corners, because that's where the highest shear was expected.

(a) *Side view of both LVDTs.* (b) *Perspective view of the top LVDT.*

Figure 4.16: *Two views of the sensors used to measure the shearing of the silicone adhesive. One LVDT was used for each glass plate (top and bottom). Because these were spring-loaded, they could measure displacement in both directions.*

These LVDTs consisted of a small spring-loaded pin that could only move along one axis, and its movement was recorded. The LVDTs were glued on the glass, and the pins were pushed against a bracket glued to the frame. The output of the LVDTs was a length in millimeters, which could be compared be used to compare the stiffness of the silicone in the model and the stiffness in real life.

As mentioned earlier, due to budget constraints it was not possible to do any type of strain measurements on the glass. A plan was drafted to measure the strain at various places using strain gauges. Unfortunately this would have taken too many man hours and material costs, so it was not possible to proceed with these measurements.

4.3 Panels

Using the information gained in Chapters 2 and 3, the specifications for the test specimens - the glass sandwich panels - were chosen. The panels used in the Cambridge experiments were used as a base. These were 1×1 m glass plates with a GFRP frame around the edge. In order to gain a bit more knowledge about the panels in a real-world application where larger glass sizes are used, the panels for this research were scaled up to 1.5×1.5 m. Even larger panels were considered, but the glass supplier could not supply thin glass larger than 1.5×1.5 m.

4.3.1 Materials

For the sake of consistency and the advantages mentioned in Section 3.2, all calculations and numerical simulations prior to the experiments had been done using the specifications of the GFRP profiles used in Cambridge. Luckily, Fiberline, who supplied those profiles, was willing to assist in this research as well, and therefore supplied the exact same GFRP profiles.

These profiles are not fully symmetrical, as they have two ribbed sides and two flat sides, though they are symmetrical from flat side to flat side or from ribbed side to ribbed side. In preparation for the assembly of the panels, the flat sides of the profiles were sanded and cleaned. Immediately before assembly they were also degreased. These steps were necessary to help the silicone adhesive bond to the GFRP.

As explained in Chapter 2, the choice was made to use a silicone adhesive to bond the panels to the glass. Silicone adhesive has a good mix of flexibility and strength, and is therefore ideal to use for such a panel. In consultation with Dow, DOWSIL 993 Structural Glazing Sealant was chosen. The adhesive was applied using the industry standard thickness of 6 mm, both to be as close to a real-world application as possible, and because this thickness would allow for enough flexibility of the adhesive.

Two types of glass were used to make two types of sandwich panel. Initially, the plan was to create all the panels - however many - with thin glass. However, the supplier was not able to supply enough thin glass. Since the type of thin glass they would supply, i.e. chemically toughened thin Falcon glass, is still a new product, it is expensive to make. Despite this, they were prepared to supply the following 1.5×1.5 m glass plates:

- $6\times$ 4 mm fully thermally toughened;
- $6\times$ 1.1 mm chemically toughened;
- $6\times$ 1.1 mm annealed.

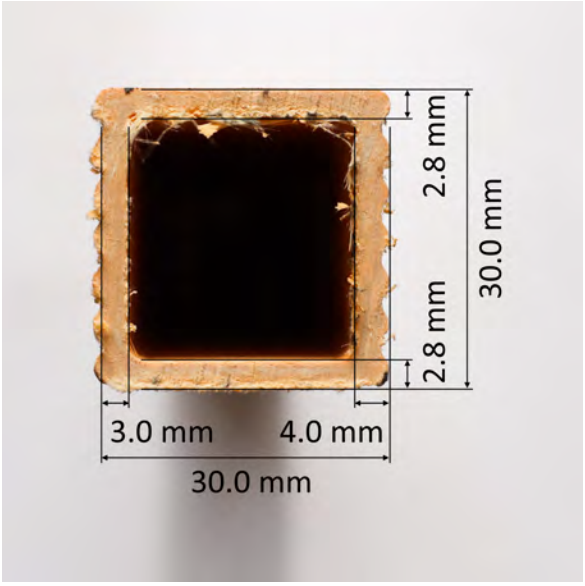

Figure 4.17: *Outer dimensions and wall thicknesses of the profiles' cross-section. The flat walls are both 2.8 mm thick, while the ribbed walls are 4.0 mm thick when measured on the peaks, and 3.0 mm thick when measured in the troughs. The outer dimension of the cross-section is measured on the peaks of the ribs.*

Figure 4.18: *The GFRP profiles cut to the correct length of 1.48 m, with 45° angles at both ends.*

Unfortunately, the 1.1 mm plates are very fragile. Therefore, three of the six panels broke during the process of chemically tempering. With the remaining three panels it was only possible to make one thin CT glass sandwich panel. There was enough GFRP to make three more panels, so the choice had to be made which glass to use. Given the fragility of the annealed 1.1 mm glass, and with that its likelihood of breakage and its low practicality for real-world applications, the 4 mm glass was chosen. Since there were six 4 mm plates, the test pieces with the following glass types (Figure 4.19) were made:

- 3× panel with 4 mm fully thermally toughened glass;
- 1× panel with 1.1 mm chemically toughened.

Figure 4.19: *Comparison between the 1.1 mm CT glass (top) and the 4 mm FT glass (bottom).*

4.3.2 Assembly

The means and space necessary for assembly of the panels were kindly been provided by Si-X and Van Dijken Glas. The glass, having been delivered by AGC to Van Dijken Glas, was first cleaned properly with glass cleaner. This was done carefully, as they were quite dirty and scratches were to be avoided.

The panels were laid flat on a movable cart with timber beams (Figure 4.20), again to avoid scratches. All the panels were assembled dry on top of each other with timber beams in between before the silicone adhesive was applied. Soft plastic shims were used in places where the panel was not completely flat.

Figure 4.20: *The first panel, partly assembled on the movable cart. Note the orange GFRP profiles that form the frame. The spacer tape is placed on the inside edges of the frame, lengthwise as well as in the corners. The blue film to protect the spacer tape's adhesive is removed before placing the top panel. The removable timber cross can also be seen here.*

To make this dry assembly possible, double sided adhesive spacer tape was used. The spacer tape is a foam band that is placed between the frame and the glass to ensure the correct spacing of 6 mm. It was placed on the inside edge 4.21 of the frame to prevent silicone spilling into the cavity. In addition, the spacer tape also has a fairly strong adhesive on both sides, so when the panels are dry-assembled, they hold their shape easily.

To make sure that the glass was as flat as possible during assembly, a removable timber cross (Figure 4.20) was placed in the middle of each sandwich panel. This was especially important for the 1.1 mm glass, as it sags significantly under its own weight when held horizontally. The timber cross kept the glass flat within a tolerance of about 5 mm. Felt was added on the outside of the cross as an extra measure to prevent scratches when the cross would be removed before the experiments.

Figure 4.21: *Top view of the corner of one of the panels. Note the orange GFRP profiles with the black spacer tape on the inside edge and the timber cross with black felt through the middle of the image.*

The 4 mm plates could be easily lifted and placed on the cart with two people, but to avoid breaking or damaging the 1.1 mm glass, the tilting mechanism of a large class cutting machine was used. The plates were manually lifted from their near vertical position in the glass rack to the mechanism, also in near vertical position. The mechanism then tilted from vertical to horizontal. The two 1.1 mm plates were laid next to each other, and the

GFRP profiles and timber cross were placed on one of the plates, and the other one was then carefully lifted on top of it, creating the sandwich panel. The full dry-assembled sandwich panel was a lot stiffer and could be safely picked up and moved to where the other panels were.

Finally, with all the panels dry-assembled and stacked, the silicone adhesive was applied by a professional glazing technician. The main reason for this is that the D993 adhesive is a two-part silicone that needs to be mixed using a large machine. Once the silicone was mixed, the nozzle was simply inserted in the space between the frame and the glass to fill it up with adhesive. This was a messy process, where care needed to be taken to not get adhesive in the wrong places, the timber crosses that needed to be removed later, for example. The excessive spillage was cleaned up, and after the final gap had been filled, the panels were left to cure for at least 48 hours before transporting them, as per the specifications of the manufacturer. However, due to several delays with regards to the experimental set-up, the panels had several weeks to cure before the start of the tests.

Figure 4.22: *The full stack of assembled panels. The bottom three panels are with 4 mm glass, the top one is with 1.1 mm glass.*

4.4 Execution

The tests with 4 mm sandwich panels were executed first. Since there is always a possibility that changes need to be made to the set-up, it was better to start with the panel type of which there were multiple.

4.4.1 First test

Since the first test was performed with the use of the 3D DIC camera system, the speckle pattern had to be painted on first. For the DIC to work, the paint was not allowed to crack. The expected deformations and strains were large enough that it would be possible that regular paint would crack, so a thin layer of special rubber paint was used for the white base layer. This paint was applied with spray cans (Figure 4.23) and left to dry, after which the black speckles were sprayed on with an airbrush with a low pressure.

When the paint had dried, the timber cross was finally removed from the first panel, and the panel was placed into the set-up with the temporary supports in place. The shear LVDTs and the corresponding metal bracket were glued onto the panel with hot glue, the corner details were placed on the corners, and the wire gauges of the displacement LVDTs were attached to the corners. In this first test, a triangular piece of MDF (Figure 4.24) was placed between the load application rod and the glass. MDF is fairly soft and light, so it was deemed a good way of spreading the load while avoiding scratches on the glass.

By hand-tightening the nut on the bottom plate, the corner of the panel was clamped between the bottom plate and the steel rod. The idea behind this was to avoid applying a bending moment

to the corners. The line of action of the load (i.e. the direction of the cable) does not cross through the steel rod, where it is applied on top of the panel. Because of this eccentricity of the horizontal component of the load, a bending moment could develop. By slightly clamping the corner, the horizontal force would be spread over a larger area by the timber block, decreasing the bending moment.

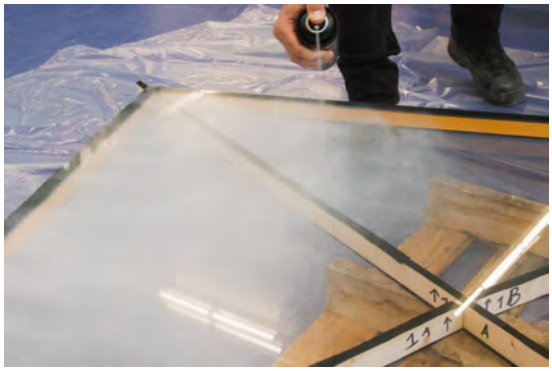

Figure 4.23: *The white base layer of rubber paint being applied.*

Figure 4.24: *Corner detail with MDF triangle to spread the load.*

With everything in place, the cables were tightened with the turnbuckles to get the slack out of them. All LVDTs and load cells were then zeroed out and the 3D DIC cameras were used to take a zero-measurement. The final thing to do before the load could be applied was to remove the temporary supports, after which the panel was only supported by the roller supports.

As soon as the panel was off the temporary supports and everyone present was at a safe distance, the load was applied. As mentioned before, a hydraulic manual pump was used for this. Since the hydraulic cylinder that was used to apply the load was not automated but had to be pumped by hand, the load was not applied with a smooth gradient, but in small increments. Despite this, efforts were made to apply the load as smoothly as possible. The pump lever was moved slowly on the downstroke, when the load was actually being applied, and quickly on the upstroke, to have as little time without load application as possible.

Partway through the test, the supported diagonal of the bottom plate 'buckled' and straightened out. However, this was not noticed during the test itself, as the panel was below chest-height, so the bottom could not be seen without ducking. It only became apparent when looking at the results, so therefore it is further discussed in Section 4.5.

At a certain point it became clear that the center displacement center would indeed probably reach its maximum displacement of 100 mm before the glass breaking, as predicted. When the sensor was almost at its maximum, the pumping was stopped, and the cylinder pressure was slowly taken off, allowing the panel to go back to its original state, only (or mostly) loaded by its self-weight. This way, the center displacement sensor could safely be removed. After it was removed, the load was increased in the same way as before.

Throughout the loading process, it appeared that the panel was not taking on a nice hypar shape. It already seemed that way fairly soon after the loading started, and it remained until the panel broke. Instead, the panel appeared to take on a mostly single-curved deformation. From support to support, the panel was bent, but from loaded corner to loaded corner, the panel was almost straight.

At a corner displacement of around 140 mm (more details in Section 4.5), the bottom panel broke. There were no real warnings before it broke, and during the test it was unclear what the reason of the failure was.

The top plate was still intact, so the loading was continued. Despite the bottom plate breaking, the corners did not have any only showed a small amount of additional deflection. The broken panel had a bit of capacity left, but soon after the loading was restarted, the top plate broke. As expected of FT glass, both plates broke into many small pieces.

4.4.2 Second test

In the first test, it appeared that the panel did not take on the desired shape. The panel looked less like a hypar, and more as if it had a single-curved deflection shape. There was one possibly major element of the set-up that could explain this difference between the expectation and reality: the corner details. Because of the way the corner was clamped between the bottom plate and the MDF triangle, the corner may not have had enough freedom to deform. It's likely that this influenced the way the panel behaved under load. Therefore, the corner detail was altered. Instead of the MDF triangle, small stacks of rubber sheets were placed between the steel rod and the glass. The same was done between the bottom plate and the bottom plate of the corner detail. This way the load is applied as point loads on the frame, without any load going directly to the unsupported glass. This solution also allowed more freedom for the panel and the frame profiles to move, because they were not clamped as much. The nuts on the threaded ends were still slightly tightened to ensure the rubber did not slip, but this did not create a clamped corner without the possibility of movement. In addition to this change, the timber block was replaced by an identically shaped block made of hardwood, as on of the softwood blocks cracked and broke during the first test.

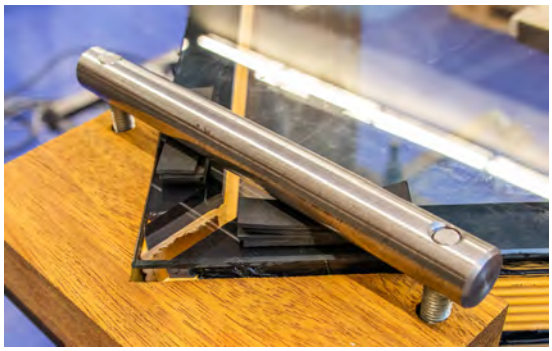

Figure 4.25: *Small stacks of rubber sheets were placed between the steel rod. This way the load was applied as point loads only on the frame, and the panel had room to deform.*

For the second test, the 3D DIC camera system was not available anymore. Therefore, a 2D DIC measuring system was created. With the one available DSLR camera, images were taken at a regular interval (2 seconds for this second test) of black and white dots placed on top of the panel. Using the software GOM Correlate, the displacement of the dots could be visualised and analysed. Because 3D DIC was not used, this panel and all the following panels did not have to be painted, and were thus completely transparent.

The panel was placed, the cables were tightened to take the slack out, the sensors were zeroed, the temporary supports were taken away and the load was applied. At the start, the panel again seemed to have a fairly single-curved displacement shape, and it looked like the loaded diagonal was relatively straight. However, at some point, the center of the top plate started moving down slower than the corners, and even seemed to move slightly upwards. Because of this, the panel started to resemble a hypar a little bit more. Similarly to the first panel, at a corner displacement of around 140 mm, the bottom plate broke. The corners moved down slightly, but not by much. The breaking of the bottom plate did cause the top plate to change shape. The glass was almost straight along the supported diagonal, while the loaded diagonal was curved. This single-curved shape remained until the panel broke at a corner displacement of around 220 mm.

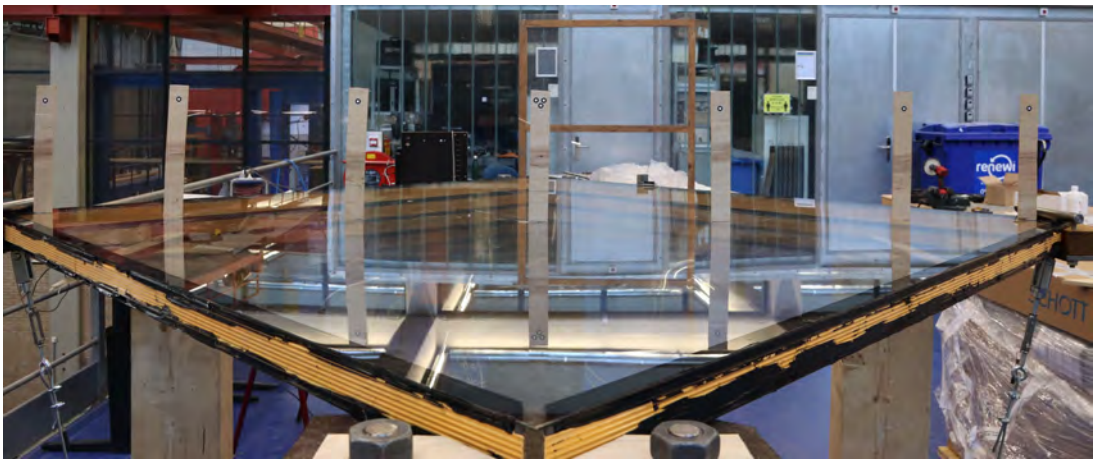

Figure 4.26: *Zero measurement of the panel in its flat state, still on the temporary supports.*

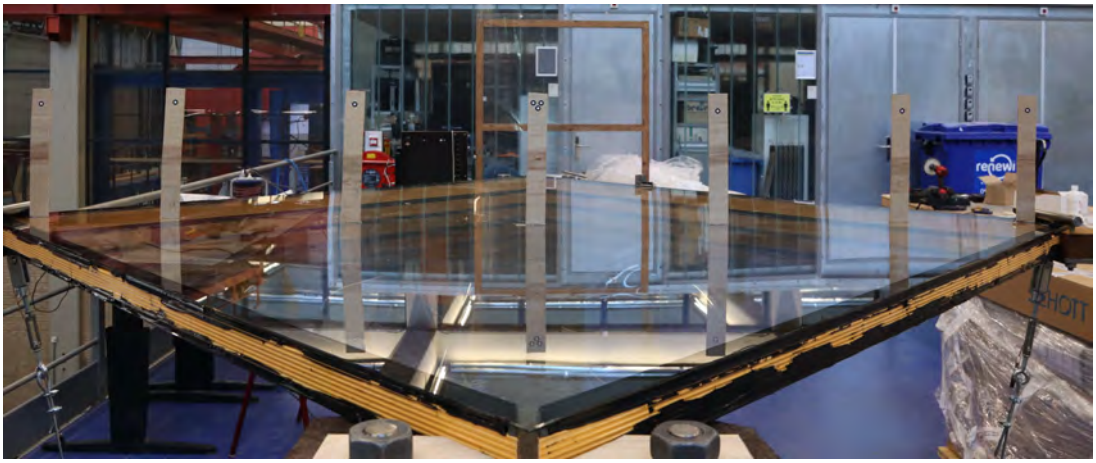

Figure 4.27: *Temporary supports removed, the panel was only loaded by its own weight and the weight of the corner details.*

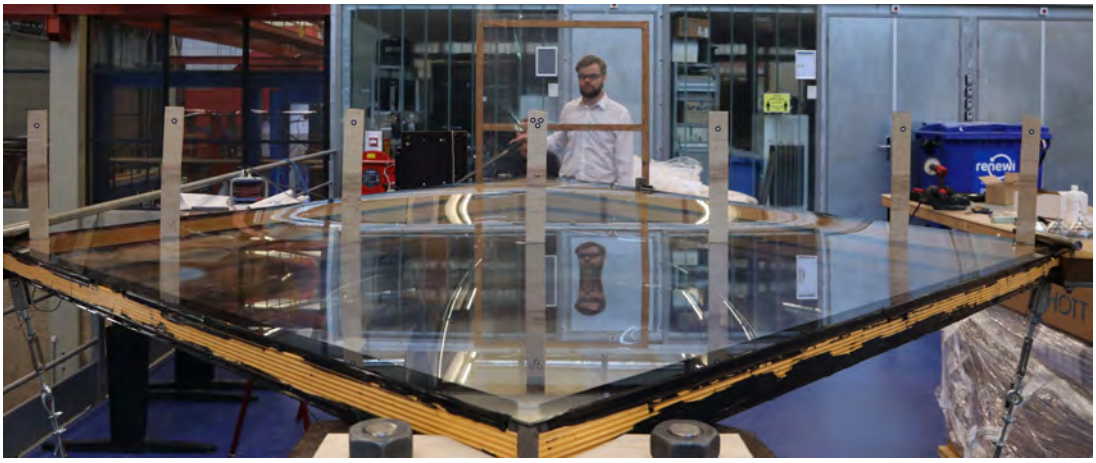

Figure 4.28: *In the first deformation stage, where the loaded diagonal was fairly straight and the supported diagonal was curved.*

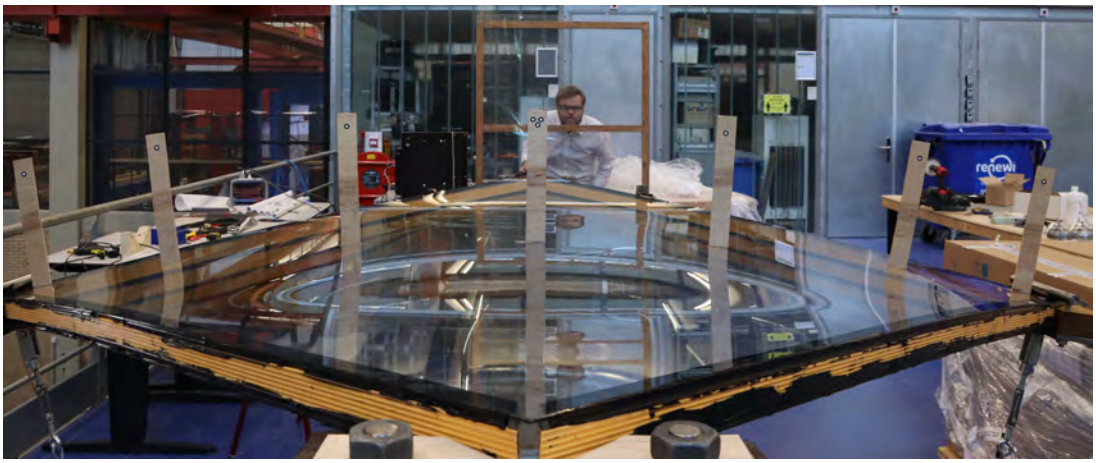

Figure 4.29: *Second deformation stage, where the center point moved up and then stayed at approximately the same height.*

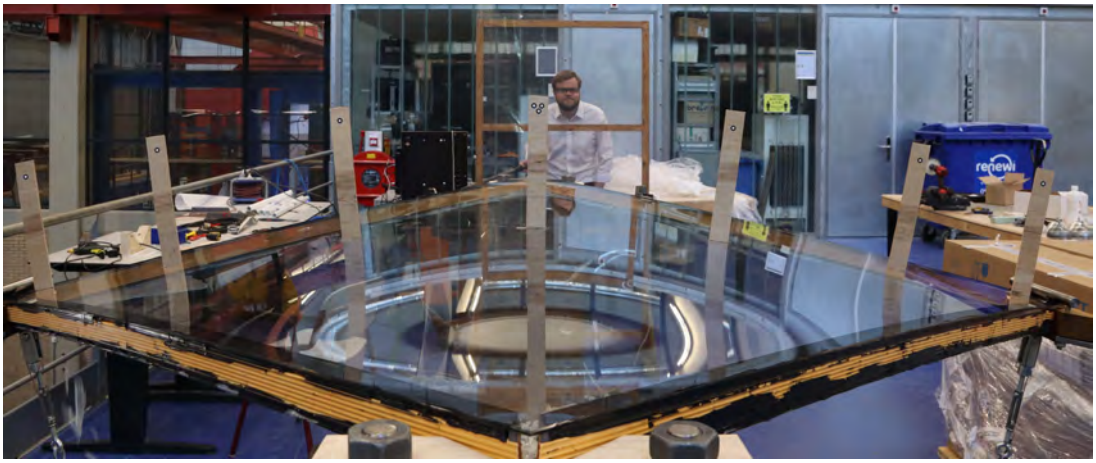

Figure 4.30: *The first frame after the bottom plate had broken. The supported diagonal was almost straight while the loaded diagonal was curved.*

Figure 4.31: *Last frame before the top plate broke. The supported diagonal has barely changed its curvature, while the loaded corners have moved down, curving the loaded diagonal more.*

4.4.3 Third test

A second DSLR camera was available for the third test. This meant that the deflection of the bottom plate could be measured with the same 2D DIC solution. As explained in Paragraph 4.2.3, half of the bottom of the panel was measured, because the bottom was partly obscured by the set-up. The choice was made to measure the loaded diagonal, and not the supported one, so the hypar resemblance of the bottom and top plates could be directly compared with each other.

For this third test, an additional element was included to make sure only the instantaneous deformation of the silicone adhesive was being measured in the previous tests, and no time-dependent viscous effects were affecting the shape of the panels. The effect of the time-dependent behaviour of the panel under its self-weight was measured by not applying load until approximately 50 minutes after the temporary supports were removed. After this time, any relaxation and/or viscous effects that were seen in the data seemed to have levelled out, so the load was applied. Obviously this test took longer than the other tests, so the cameras were set to take a picture every 5 seconds instead of every 2 seconds, to make sure all the images would fit on the SD cards.

The panel behaved the same as the one in the previous test. First the loaded diagonal was fairly straight, and at a certain point the center point of the top plate moved up. However, the behaviour diverged from the previous test when not just the bottom plate broke at a corner displacement of 140 mm, but both plates broke simultaneously.

4.4.4 Fourth test

For the fourth and final test, the only panel with 1.1 mm CT glass was used. Because the glass was so flexible, the temporary supports were extended with the timber crosses that were taken out of the panel. Due to these extensions, the supports were not just touching the glass, but also the frame, which would carry most of the self-weight because of its relative stiffness.

2D DIC was used on this panel as well, but to influence the thin and flexible glass less by putting weight on it, 5 dots were used instead of 7 on top and 3 instead of 4 on the bottom. Even before the dots were placed, it could be seen that the top plate was already sagging significantly more under its own weight than the 4 mm plates.

After the panel was taken off the temporary supports and load was applied, it quickly became apparent that there was hardly any resemblance to a hypar. The loaded diagonal looked almost perfectly straight, and the black-and-white dots moved downwards at seemingly the same rate as each other. At a corner displacement of 110 mm, the bottom plate broke into large shards, not dissimilar to how annealed glass breaks, with a maximum size of approximately 15×15 cm. When the bottom plate broke, the corners, and with it the loaded diagonal, immediately came down by a lot, approximately 120 mm. Despite this, there was still travel left between the corner and the cable pulleys, so the loading was continued.

The loaded diagonal looked almost perfectly straight after the bottom plate had broken, and the curvature of the supported diagonal was so great that the panel almost fell in between the supports. However, just before the panel would have slipped down, the top plate broke as well. The way the top plate broke was very different from all the other fractures. Near the edges of the plate and in the area around the supports, it broke in large shards similar to the bottom plate. However, in the center region (Figure 4.33) the glass broke into long, thin rods that ran from one loaded corner to the other. These rods had a length of up to around 1.5 m, so they didn't span the full length of the loaded diagonal, which was 2.12 m. They had a cross-section of around t×t to t×1.5t, with t the thickness of the glass.

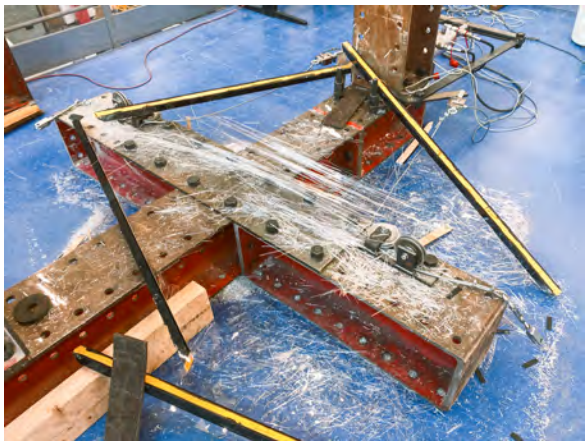

(a) *Full view of the broken panel.*

(b) *Close-up of the glass rods.*

Figure 4.32: *Two views of the glass rods that the 1.1 mm glass broke into. Note that they only formed around the central area of the panel.*

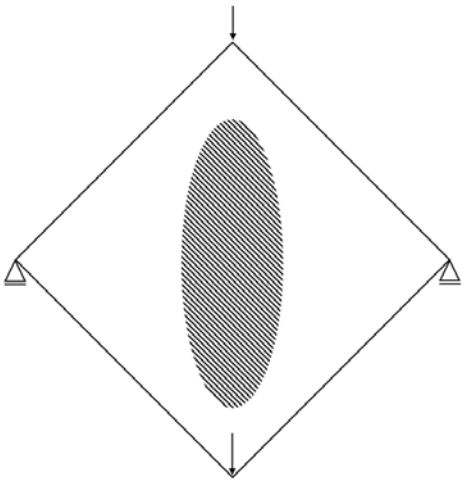

Figure 4.33: *The approximate area where the top 1.1 mm plate fractured into long thin rods.*

4.5 Results

The results of the experiments are discussed in this section. First, a few matters specifically related to the first test are discussed. After that, all data of the 4 mm panels is presented, first the data gathered at the corners (displacement and load), then the DIC data. The same is then done for the 1.1 mm panels. Finally, the results of the experiments are compared to the results from the numerical modelling. The shear of both panel types is also shown in the final section, as it is mostly relevant for the assessment of the models.

4.5.1 First test

As mentioned in Paragraph 4.4.1, the first test was the only one that included the use of a displacement sensor for the bottom plate. Because the sensor ran out of travel halfway through the test, it had to be removed. We can see this in the time vs load graph in Figure 4.34, which shows a dip to almost zero load.

Another interesting aspect of the graph is the smaller dip in the first part of the graph, around t = 170s. At this point, the bottom plate straightened out. This can be seen more clearly in Figure 4.35, where the graph first goes down, and at a certain point suddenly moves up again. This was not noticed during the test itself, but it was obvious from the data, as well ass video footage that was made from below (screenshots in Figure 4.36), that the bottom plate did straighten. The center point does move down after the straightening, possibly due to the top and bottom plates touching, forcing the center of the bottom plate down.

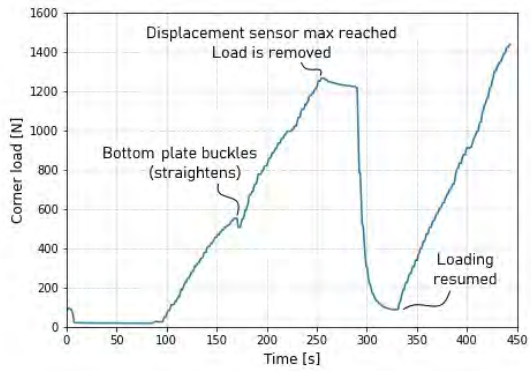

Figure 4.34: *Time vs corner load graph of the first test. Only the load of one of the corners is plotted, as the load graph of the other corner was near identical. The first test was done using the 4 mm panels, and was the only test with a displacement sensor on the bottom plate. The graph starts at around 100 N, because the panel was slightly tilted while taking away the temporary supports, increasing the tension in one of the cables. After the removal of the temporary supports, the cables had a little bit of slack, decreasing the load almost to zero. Note the small dip in load at t = 170s due to the straightening of the bottom plate. The dip in the middle of the graph exists because the load was removed to remove the central displacement sensor. Around t = 310s second mark there is a small plateau. This is where the bottom plate broke. The graph ends where the top plate broke as well.*

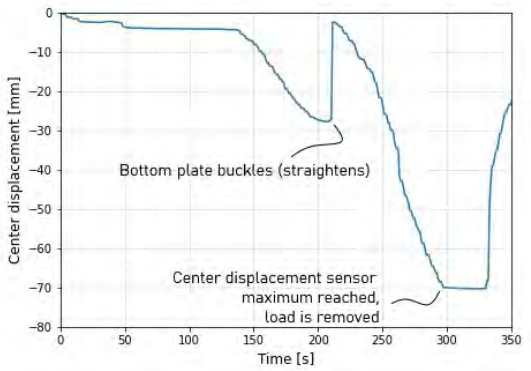

Figure 4.35: *Time vs center displacement graph of the first test. The center displacement is measured with a displacement sensor placed underneath the bottom plate. Halfway through the experiment (around t = 320s), it ran out of travel and had to be removed. The initial part of the graph shows the deflection due to self-weight. Once the load was applied on the corners (at around t = 140s), the center displacement increased. Once a displacement of around 25 mm was reached, the downward movement became slower. At t=210s, the center of the bottom plate suddenly moved upwards, because at that point, the supported diagonal of the bottom plate straightened. The graph ends where the sensor was removed.*

(a) *Before straightening.* (b) *After straightening.*

Figure 4.36: *Images of the bottom of the panel just before and just after the supported diagonal of the bottom plate straightened. Red lines are added at the tip of the displacement sensor to make it clear that the center point moved upwards.*

4.5.2 Corner data: 4 mm panels

In the following figures, we can see the graphs of the data recorded at the corners. Figure 4.37 shows the displacement over time, and Figure 4.38 shows the load over time. For both graphs, the data is only plotted for one of the corners is plotted. The panels' behaviour turned out to be almost perfectly symmetrical, so plotting both corners would only clutter op the graphs without adding additional information. Note also that in both graphs, test 1 is split into two parts. 'Test 1 - Part 1' is the part where the displacement sensor for the bottom plate was still in place, and 'Test 1 - Part 2' is with the sensor removed.

Because the load application was manually controlled, there was no real way of keeping the speed of loading consistent. Therefore, one needs to take care comparing the individual lines each other. A steeper graph does not mean a different stiffness, it only means the load was applied more quickly. With this in mind there are some interesting points to be taken from these graphs.

We can see in Figure 4.37 that both tests 1 and 2 had the bottom plate break before the top one. Both lines show a slight jump in corner displacement, though the size of the jump is very different. In test 1 (around t = 130s), the jump is barely noticeable, while in test 2 (around t = 170s), the jump can clearly be seen. This may have to do with the higher displacement at which the bottom plate broke. There is a spread in the displacement at which the full panel failed. The first panel broke at 210 mm, the second at 220 mm, and the third at 170 mm. Although it must be noted that in test 3, both plates broke at the same time.

In Figure 4.38 we can see the displacement versus time graphs of the 4 mm panels. Though the angle of the graphs is not consistent due to the time dimension, the general behaviour is very similar. The lines start out with an almost linear phase, especially in tests 2 and 3 this phase is close to linear. At the point where the bottom and top plates start touching (t = 70s for tests 2 and 3, and part 2 of test 1), there is a sudden increase in stiffness, because the plates cannot move freely anymore. As the load increases, this stiffness decreases again, until there is another sharp increase. At that point, the plates both moved upwards. The failure of the bottom plate occurred at similar loads for all three plates, around 1250 N for test 2, and a little over 1400 N for tests 1 and 3. In test 3, the top plate broke at practically the same time as the bottom plate, so the graph ends there. In test 1 and 2, the bottom plate did not break immediately, so the panel had some capacity left. There was a big drop in load, as the panel stiffness decreased dramatically due to the bottom plate breaking. After this, the panels could still take some deformation and load, a little over half of what was needed to break the bottom

plate. At the end, the top plates broke as well, ending the measurements.

The final graph that is generated from the corner data of the 4 mm panels is the load versus displacement graph shown in Figure 4.39. Most of the qualitative aspects of this graph are similar to the previous one, so will not be discussed again. However, there are some key points to be taken away from this visualisation.

Because the load is plotted against the displacement, the stiffness of the different panels can be directly compared. Because the shape of the graphs is roughly similar between Figures 4.38 and 4.39, we can say that changes in slope in the displacement versus time graphs is an indication of a stiffness change, but we need to keep in mind that this is only an indication of relative stiffness throughout the experiment, not a measure of absolute stiffness.

It is interesting to note that the first part of test 1 shows stiffer behaviour than the other two panels in the first 60 mm of corner displacement. It is possible that this is due to the clamping of the corners, which delayed the buckling of the bottom plate. After the bottom plate is buckled, the stiffness of all panels is very similar. At around 100 mm corner displacement, the stiffnesses start to diverge slightly, as panel 1 starts to become stiffer than panels 2 and 3.

The second part of test 1 behaves very differently from tests 2 and 3, and even from the first part of test 1. Not only is the corner displacement much higher at the lowest load (approx. 100 N), the shape of the graph is very different from all the others. The graph displays the same 'branches' as the ones described earlier, but the points at which the branches transition into each other is very different. Obviously the deformation shape of either of the plates had changed during the first part. It is possible that when the load was backed off, the plates did not return to their original shape, therefore changing the behaviour when the load was added again.

Finally, the point at which the bottom plates of all panels broke are fairly close to each other, both in terms of displacement and load. The bottom plates - and in the case of test 3, the top plate as well - all broke between 130 mm and 170 mm, and between 1250 N and 1450 N.

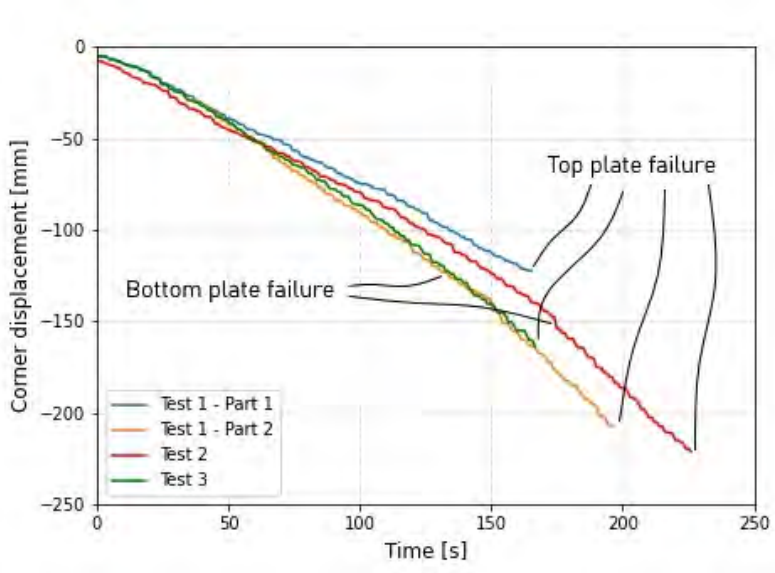

Figure 4.37: *Corner displacement versus time graph of the three tests performed with 4 mm panels. The first test is split in two parts, the part with the center displacement sensor in place, and the second part with the sensor removed. Test 1 and test 2 both had the top plate break later than the bottom one, and therefore display a slight jump in displacement (t = 130s for test 1, t = 170s for test 2). Test 2 shows a larger jump in displacement, and it happens at a larger displacement. Interestingly, the displacement at which the entire panel failed differs significantly between the tests, from about 120 mm for test 1 to 220 mm for test 2.*

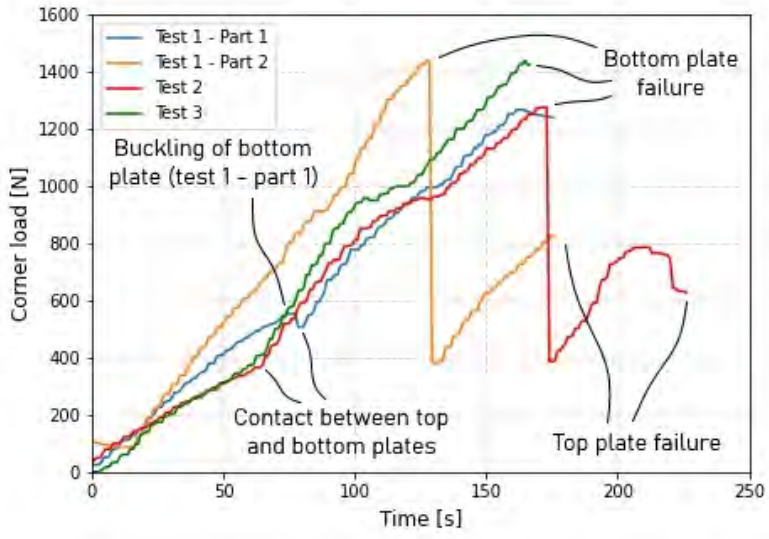

Figure 4.38: *Corner load versus time graph of the three tests performed with 4 mm panels. Because the time is plotted on the horizontal axis, and the load application was manually controlled, a steeper or flatter line does not mean stiffer or more flexible behaviour. All lines show roughly the same behaviour throughout the graph. It starts with a part that is fairly linear. When the plates start touching in the center, there is a sharp upward kink that shows an increased stiffness. After that, the stiffness decreases again. Then again a sharp kink when the top loaded diagonal straightens, and a linear increase in load until one or both of the plates break.*

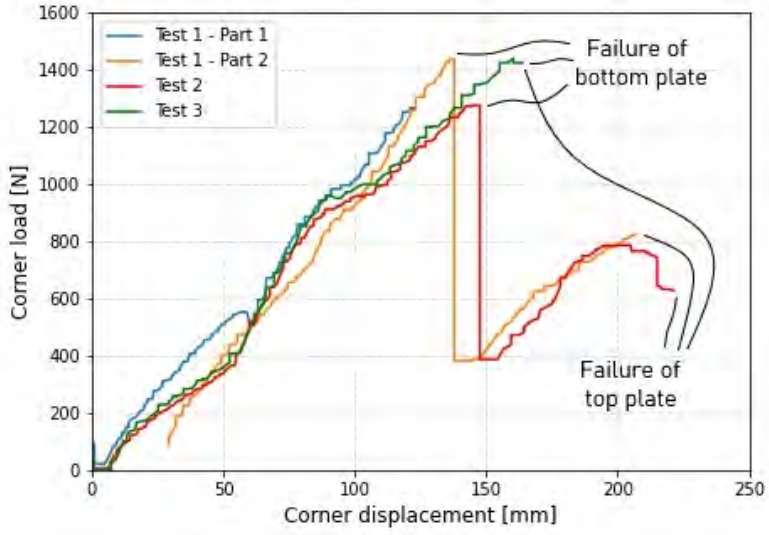

Figure 4.39: *Corner load versus displacement graph of the three tests performed with 4 mm panels. The stiffness of the panels can be directly compared, because there is no time dimension. The panels in test 2 and 3 behave very similarly, but the panel in test 1 behaves differently, both in part 1 and part 2. When the bottom plate buckles in part 1 of test 1, all three panels behave very similarly between corner displacements of 60 mm to 100 mm. The bottom plates break in a similar region for all three panels.*

4.5.3 DIC data: 4 mm panels

In addition to the data gathered by the LVDTs and load cells at the corners, displacement data was gathered through the use of Digital Image Correlation, or DIC. Using *GOM Correlate*, the images from the *GOM ARAMIS Adjustable* camera are used to create a three-dimensional displacement field (Figure 4.40). The camera was not positioned exactly in the middle of the surface, so the image is slightly distorted by perspective, but the software is able to correct for this.

In Figures 4.42 and 4.43, the displacement field is shown. The background image is left out, so the contour lines can be seen more clearly. From these images, it is quite clear that the shape of the displaced top plate remains almost the same throughout the entire loading process. The curvature of the plate occurs mostly along the supported diagonal, while the loaded diagonal is almost straight. This is also visible in Figure 4.41, where the two lines have a fairly consistent distance between them throughout the experiment, meaning the loaded diagonal mostly has the same shape at all points.

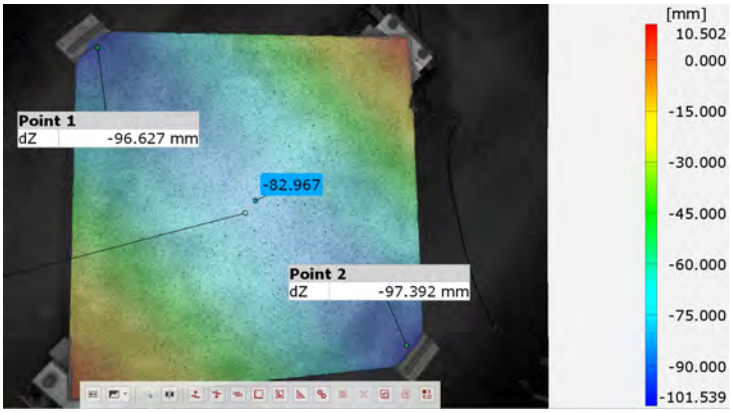

Figure 4.40: *A contour plot of the displacement field mapped onto an image taken by the* GOM ARAMIS Adjustable. *An arbitrary point was chosen to show the image.*

.

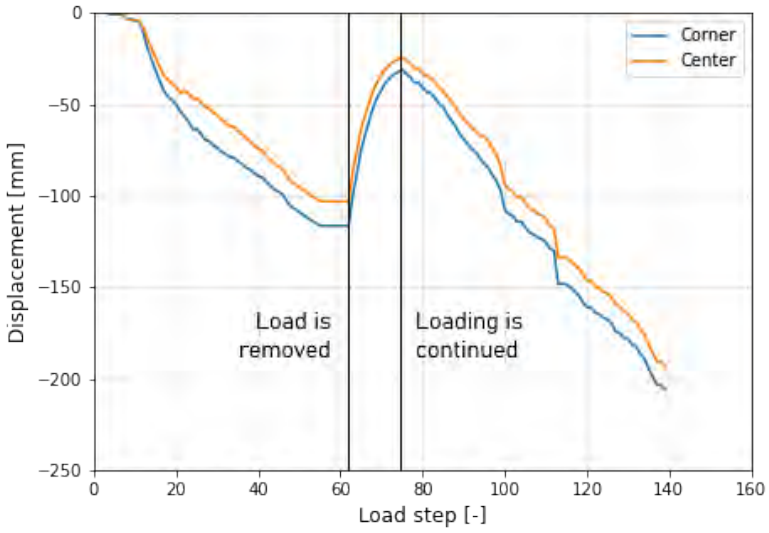

Figure 4.41: *The vertical displacements from the 3D DIC data. On the horizontal axis the load steps are plotted. The data was not recorded at consistent time intervals, but the time could not be exported from GOM Correlate, therefore each data point is counted as a 'load step'. The displacements are plotted for one of the corners and the center point. We can see that at the start the lines move away from each other, but then stay at the same distance. When the load is removed, they move back closer together, but when the load is re-applied, the quickly move back to the same distance as before.*

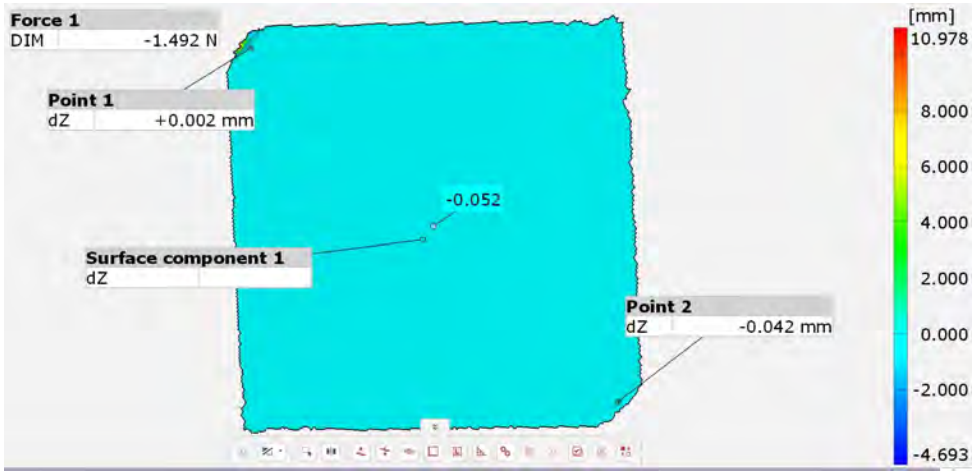

(a) *Flat reference state*

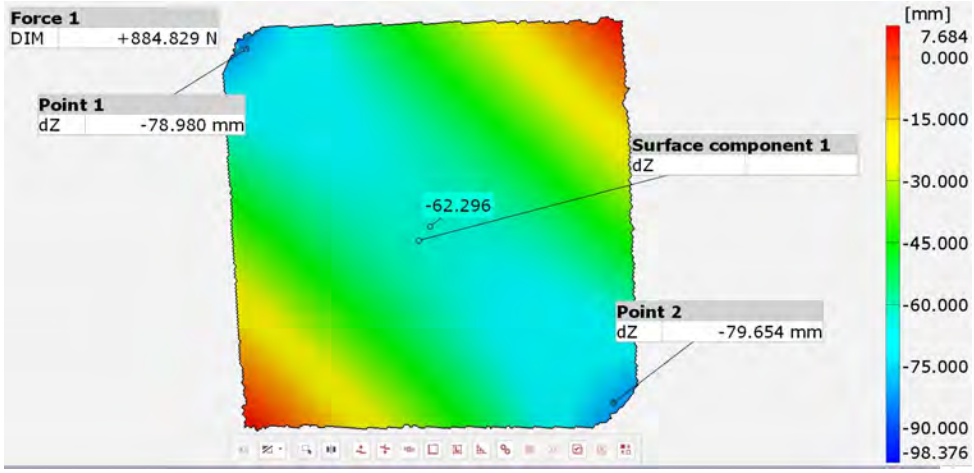

(b) *Halfway through the first loading phase, with the center displacement sensor in place. Note the mostly single-curved displacement field, with curvature mostly on the supported diagonal.*

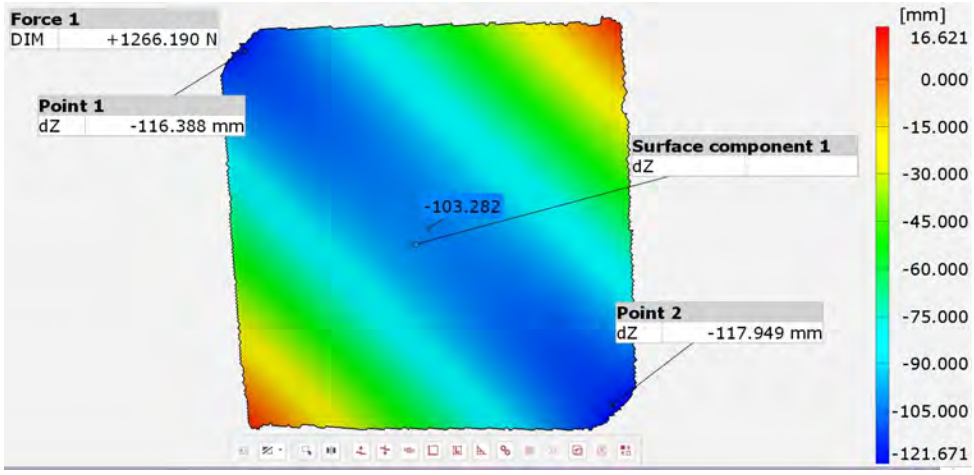

(c) *At the point just before the load was taken away to remove the center displacement sensor. The contour lines are almost perfectly straight, indicating that the supported diagonal is almost perfectly straight.*

Figure 4.42: *Part 1: Screenshots of several key moments in the 3D DIC data. Note that the scale is not the same in all images. The color scale was set to automatically scale to the result shown, so the shape of the panel could be clearly seen. Vertical displacement magnitude is shown on the loaded corners and in the center.*

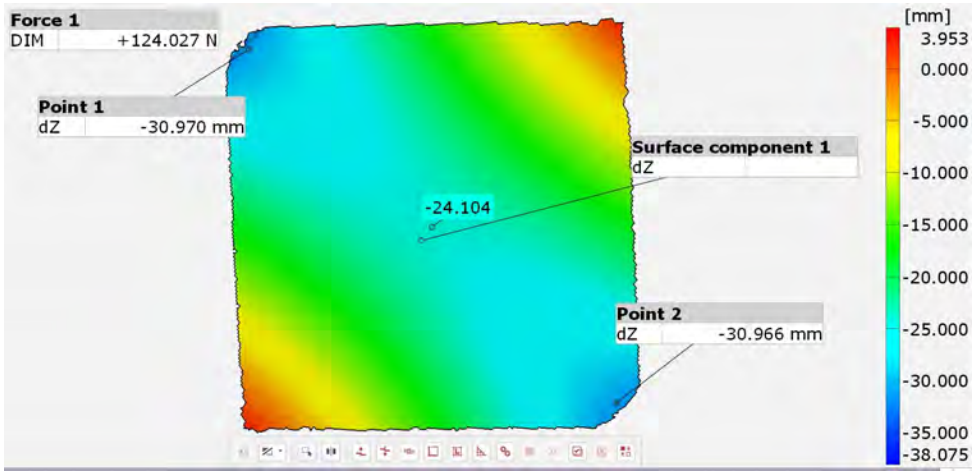

(a) *When almost all the load is taken off, the loaded diagonal has a bit more curvature, although still not a lot.*

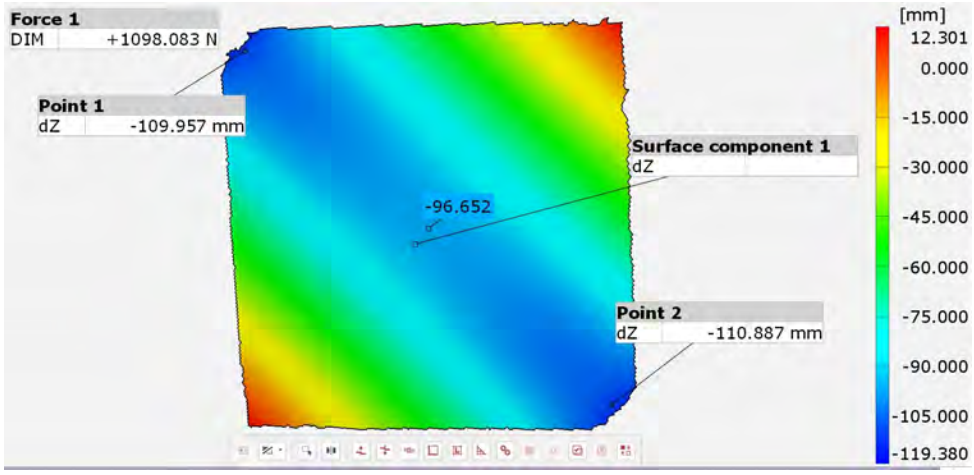

(b) *Halfway through the second loading phase, the loaded diagonal is yet again quite straight. There are no significant shape changes during this second loading phase, including before and after failure of the bottom plate.*

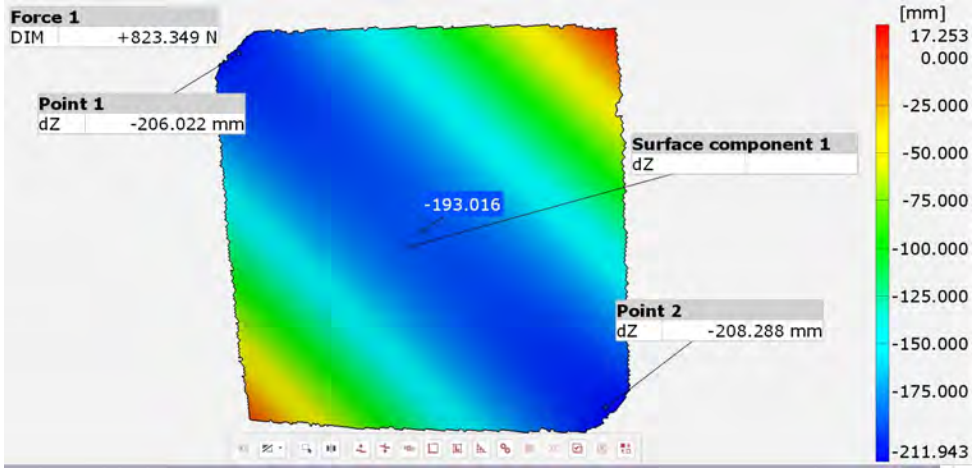

(c) *Final data point before failure of the top plate.*

Figure 4.43: *Part 2: Screenshots of several key moments in the 3D DIC data. Note that the scale is not the same in all images. The color scale was set to automatically scale to the result shown, so the shape of the panel could be clearly seen. Vertical displacement magnitude is shown on the loaded corners and in the center.*

For the second and third test with 4 mm panels, the 3D DIC system was not available, so a 2D

DIC system was made using DSLR cameras, as explained in Paragraph 4.2.3. For test 2, only the top plate was measured, for test 3, the top and bottom plates were measured. The images are processed using the same software as the 3D DIC data, GOM Correlate. Once the images have been imported, a scale has to be set (Figure 4.44), so the displacements can be calculated correctly. The black-and-white dots that are used as points for the software to follow are exactly 10.0 mm in diameter, so these can be used as a way of scaling. Then the dots that the software needs to follow have to be selected, and the identification tolerance for recognising the dots has to be set. If the tolerance is too high, GOM Correlate will wrongly recognise other objects as dots, and if the tolerance is set too low, the software will not be able to follow the points in between images. Because there are issues with the latter in some of the tests, any objects that could be wrongly identified as a point are manually blacked out, and the tolerance is set very high (up to 400 mm for some of the files). This leads to usable results, with the software being able to identify all points correctly at all times. Once the deformation has been calculated, it can be visualised as shown in Figure 4.45.

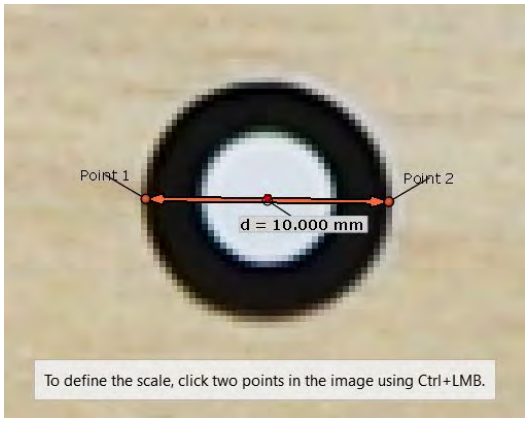

Figure 4.44: *Scaling the images in GOM Correlate to be able to use 2D DIC. The outer diameter of the black-and-white dots is exactly 10.0 mm.*

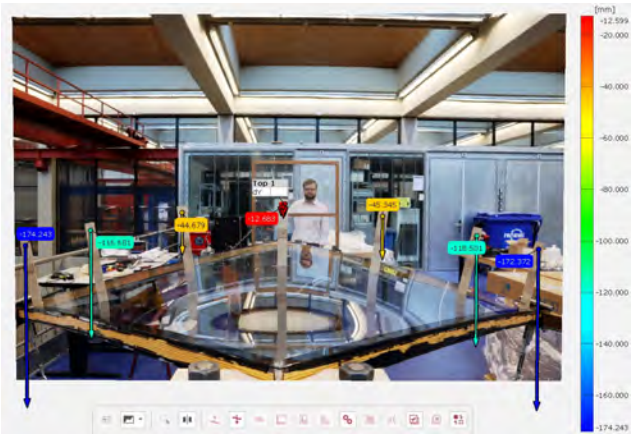

Figure 4.45: *Example of the visualisation of vertical displacement in GOM Correlate. Image was taken at an arbitrary point to show the concept.*

With the scale and point identification set correctly, the vertical displacement of each point could be calculated by GOM Correlate. However, as a final step the vertical displacement data needs to be corrected. The black-and-white dots are not placed directly on top of the glass, but on wooden strips, 20 cm above the glass. If the glass gets any curvature in the loaded diagonal, the black-and-white dots that are not in the center will move outwards. This means that the dots will not only move downwards because the corresponding point on the glass moves downwards, but also because the wooden strip rotates around that corresponding point. The fix for this is fairly simple. Using the height of the dot above the glass - which can be measured in GOM Correlate - and the sideways displacement, the additional displacement due to the rotation can be calculated and subtracted from the total vertical displacement.

Because the time interval between each measurement was known for this 2D DIC data, the displacement of each point can be accurately plotted against time. In the displacement plots, the points are numbered from left to right as they are shown in Figure 4.45. Point 1 is always the left corner. In all plots except Figure 4.48, the final point is center of the plate. The data from the right side of the panels is not plotted, because the displacements are almost perfectly symmetrical. The only exception is the top plate of the 3^{rd} test, where all points are plotted, because it's not fully symmetrical. Note that in all tests, the reference of 0 mm displacement is taken with the temporary supports in place. This means that the reference for the corners is the panel in an undeformed state, but the center point has already sagged due to self-weight.

In Figure 4.47 we can see the vertical displacement of the top plate of the second test. In this

graph, we can see that the center point moves down almost as much as the corners, meaning the loaded diagonal is almost straight. When the plates start touching, the center of the plate stops moving down, and then starts moving up, starting around t = 125s. Once the bottom plate breaks, the supported diagonal straightens, shown by the fact that point 4 almost goes back to a displacement of 0 mm.

All points are plotted in Figure 4.48, not just half of the panel. This is because points 2 and 6 and points 3 and 5 are not symmetrical to each other. Though the asymmetry is not very large (10 mm at maximum), it is still peculiar, because the corners are actually almost perfectly symmetrical, except a small difference at the end. The difference, however, is easily explained. Due to a measurement error, the dots were not placed in the correct position, as can be seen in Figure 4.46. Points 5 and 6 are placed further from the symmetry line than points 2 and 3. We would therefore expect their displacements to be higher, which is indeed what we see in the graph in Figure 4.48. What can also be seen is that he behaviour of the panel is almost identical to the one in test 2. The loaded diagonal is almost straight until the point where the plates touch, then the whole panel takes a more hypar-like shape, which remains until the whole panel breaks.

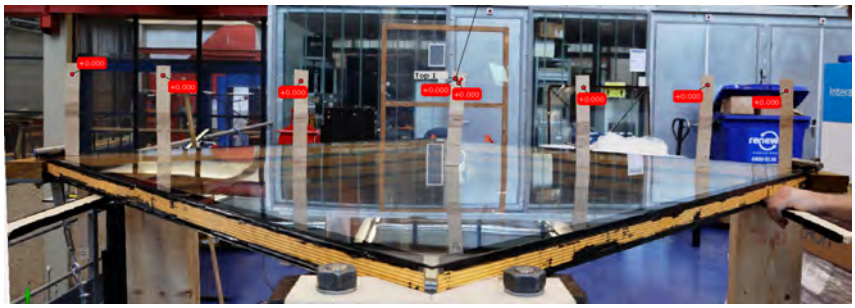

Figure 4.46: *Due to a measurement error, the dots were placed in the incorrect positions on the top plate of test 3, leading to asymmetrical results.*

Figures 4.49 and 4.50 show the vertical displacement of the bottom plate and an estimation of the gap between the top and bottom plates. Four points were placed on the bottom, but shortly after the panel was taken off the temporary supports, the second one from the right fell off, so there is no data from that point. Very quickly into the loading process, the bottom plate straightened along the supported diagonal. Interestingly, this did not cause any significant change in stiffness of the panel, because the corner displacement does not show any change in slope. After the center point had gone back to zero because of the buckling, it remained straight until the top and bottom plates touched. For the first time we do have evidence that this is indeed the point at which the plates touch, because we have comparable data from both plates.

An estimation of the gap is shown in Figure 4.50. This is calculating by taking the gap as designed and measured after assembly (42 mm), adding the vertical displacement of the bottom plate, an subtracting the vertical displacement of the top plate. It is assumed that the plates start touching at t = 75s. This is not where the gap reaches 0 mm in the graph, but this is likely due to errors. For example, the top plate may have sagged more under its own weight than the bottom plate, and there may be some measurement errors. There is a big change in the slope of the gap graph, from decreasing to a slope of almost 0. Because of this, it is assumed that that is actually where the plates touch.

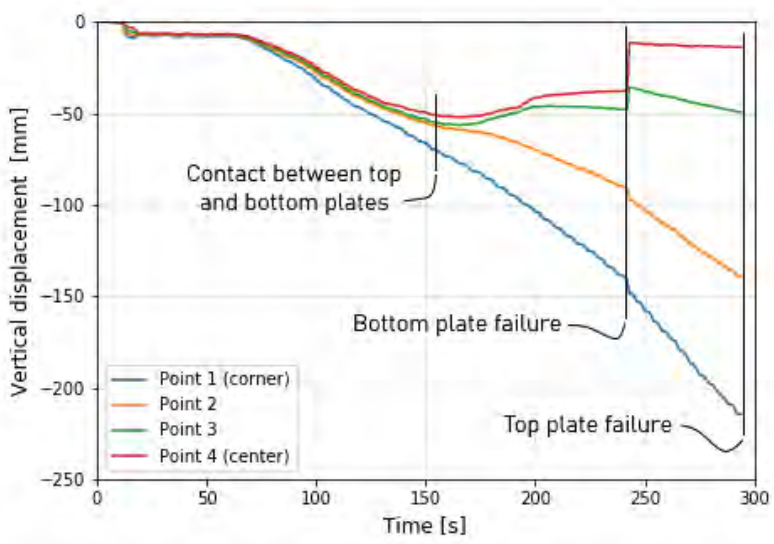

Figure 4.47: *Vertical displacement of the top plate of test 2 plotted against time. The points are numbered from left to right, so point 1 is the left corner, and point 4 is the center of the plate. The time interval between each data point is 1 second. Around t = 125s, the plates start touching, and at t = 240s the bottom plate breaks.*

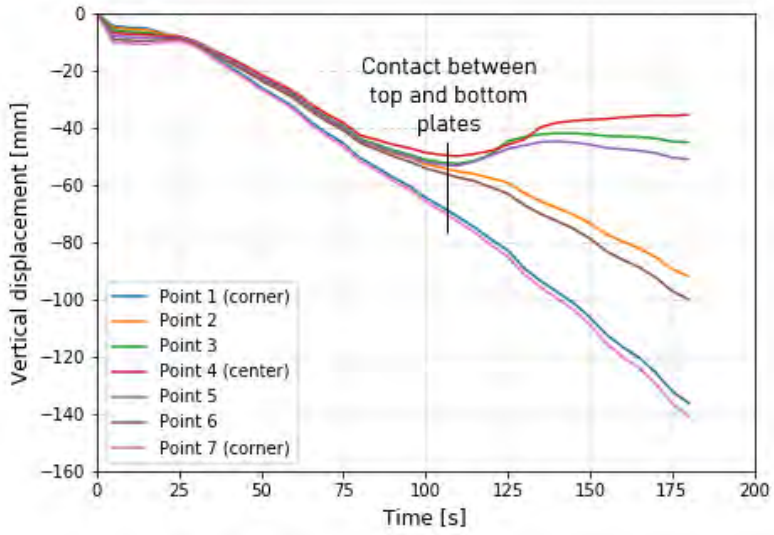

Figure 4.48: *Vertical displacement of the top plate of test 3 plotted against time. The points are numbered from left to right, so points 1 and 7 are the left and right corners, respectively, and point 4 is the center of the plate. The time interval between each data point is 5 seconds, so the lines are smoother. Around t = 90s, the plates start touching, and at t = 180s both plates break simultaneously.*

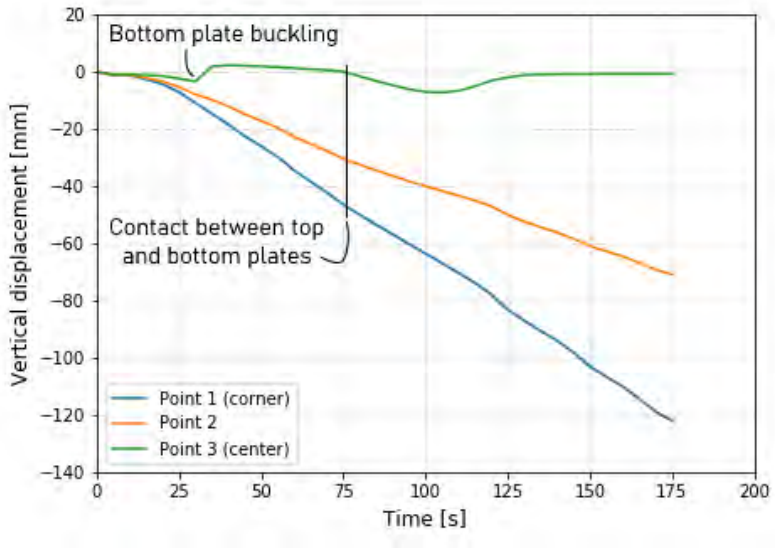

Figure 4.49: *Vertical displacement of the bottom plate of test 3 plotted against time. The points are numbered from left to right, so point 1 is the left corner, and point 3 is the center of the plate. The time interval between each data point is 5 seconds, so the lines are smoother. Around t = 30s, the bottom plate straightens along the supported diagonal. At t = 75s, the top plate start touching the bottom plate so the center points gets pushed down. Soon after, both plates move back up. At t = 175s, both plates break simultaneously.*

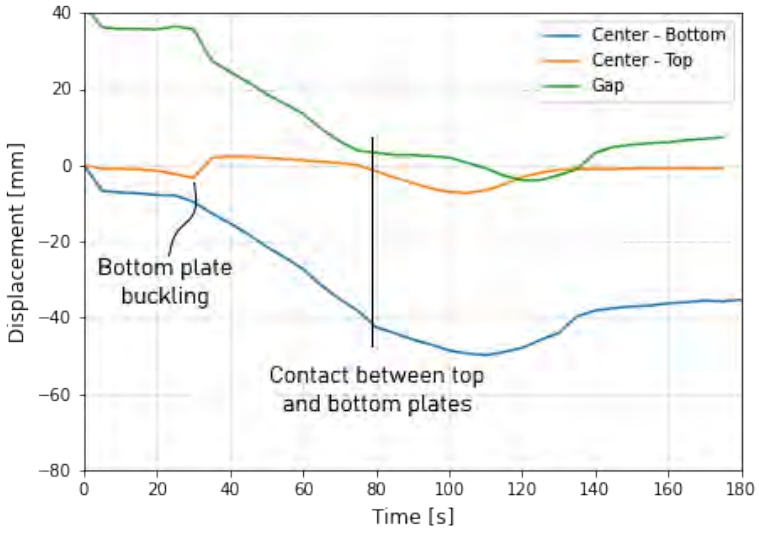

Figure 4.50: *Vertical displacement of the center of the top and bottom plates of test 3, as well as an estimation of the gap between them.*

4.5.4 Corner data: 1.1 mm panel

The data gathered at the corners of the 1.1 mm panel is shown in Figures 4.51 and 4.52. The first interesting takeaway is that after 50 seconds (see Figure 4.51), the loading is started, and the displacement has a small but sudden drop. In the images taken for the 2D DIC, a significant change in shape of the top plate is visible. In Figure 4.53a we can see that when the temporary supports are removed, the top plate is sagging slightly, but there are no large curvatures and the

panel is relatively flat. As soon as the load is applied, i.e. within the first 25 mm of displacement, the top plate undergoes a big change in shape. Most of the top plate sags significantly, with only the regions near the supports remaining flat. There are two possible explanations for this. The first is that the weight of the wooden strips to hold up the dots, although low, forces the top plate to sag more quickly. However, one would expect this effect to already start showing when the panel is loaded with only its self-weight. The second, more likely possibility is that due to the glass being so thin it immediately settles into the 'buckled' shape with the straightened diagonal once any sort of displacement is applied to the corners. Around the supports, the glass is supported by two pieces of the frame, so in that region it has a higher stiffness, causing it to retain its shape. This effect may be amplified by the small additional weight of the wooden strips. It seems that once this initial change of shape has occurred, the whole panel is in a stable configuration with a relatively constant stiffness.

After the initial drop in displacement, the load is increased until the bottom plate breaks around 120 mm. When it breaks, the whole panel drops about 160 mm. The load is increased, but because there is a lot of slack in the cables due to the drop, the corner displacement does not change. When the slack is taken out, the panel deforms until about 390 mm before the top plate breaks.

From Figure 4.52 we can see very well that after the initial change in shape, the stiffness is constant from 40 mm to 120 mm corner displacement. Only very little load is required to get the panel to deform: 200 N to get to 120 mm corner displacement. The load drops to below 0 N when the bottom plate breaks, because the load cell was zeroed after the slack was taken out of the cables, allowing the load to get below 0 N with a large amount of slack due to the big drop in displacement.

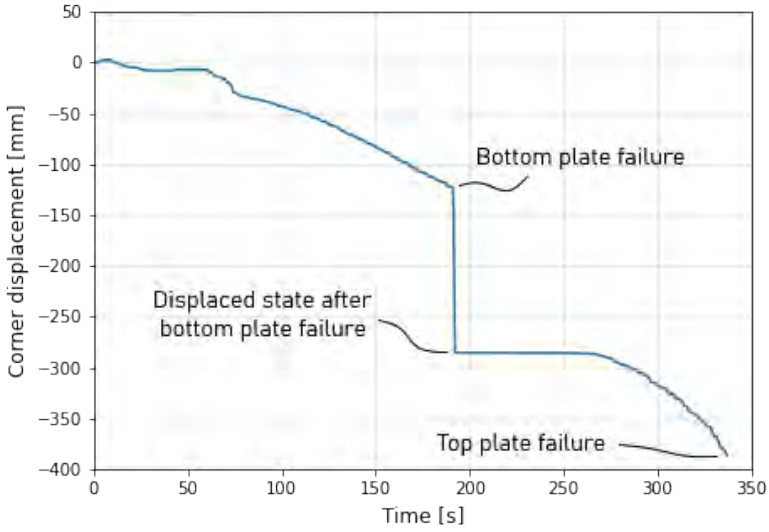

Figure 4.51: *Displacement versus time of the 1.1 mm panel. The first 50 seconds are displacements from removing the panel from the temporary supports. After 50 seconds the load application starts, and the corners see a small drop in displacement, which suddenly stops. After that, the corner displacement follows a smooth trajectory until the bottom plate breaks. The corners experience a drop of about 160 mm. After this there is slack in the cable, so while more load is applied, the corner displacement does not change. Ultimately the top plate breaks at almost 400 mm displacement.*

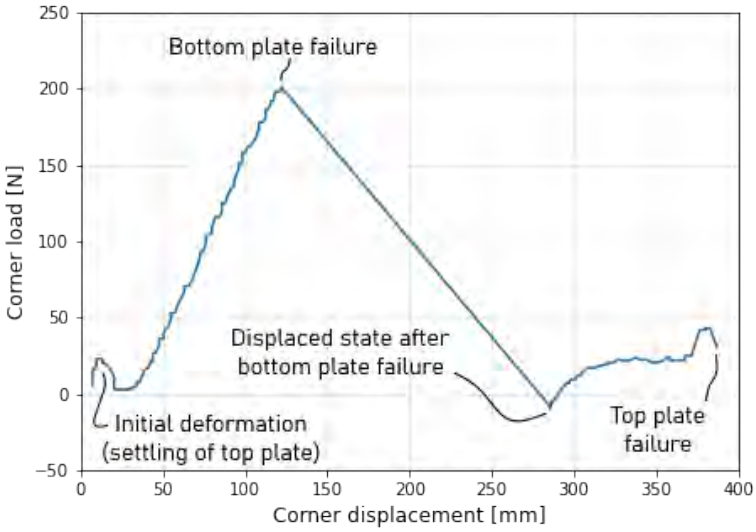

Figure 4.52: *Corner load versus corner displacement of the 1.1 mm panel. At first, the load increases with displacement, but then goes back to almost zero. The load then steadily rises until the bottom plate breaks. The displacement dramatically increases and the load goes back to less than 0 N. This is because the load was set to 0 after the slack was taken out of the cable, which took about 30 N. Very little additional load is required for the final 100 mm of displacement before the top plate breaks as well.*

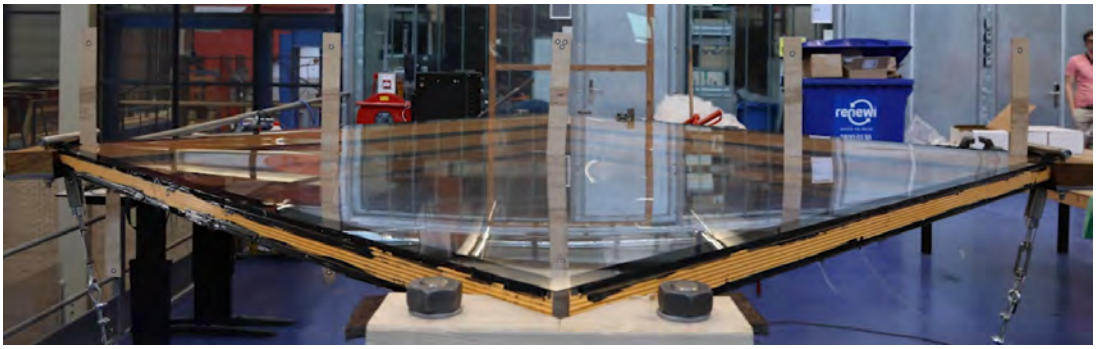

(a) *The 1.1 mm in its unloaded state, only sagging under the dead weight of the components.*

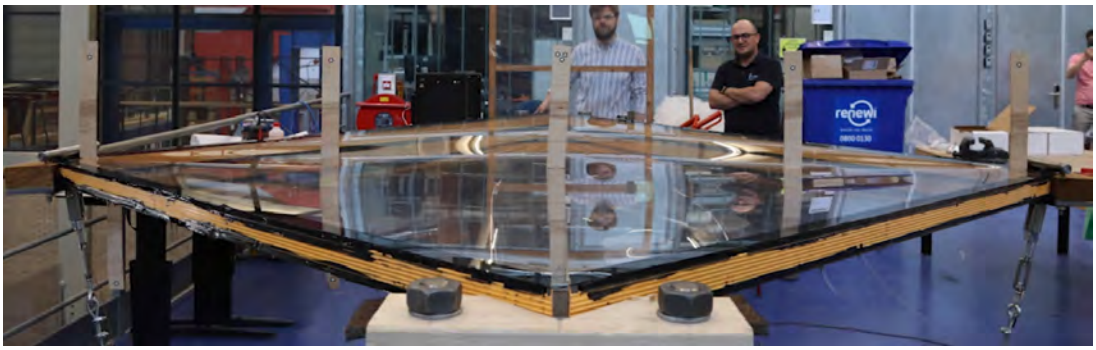

(b) *The 1.1 mm just after the start of load application, with significant ripples along the edges.*

Figure 4.53: *The 1.1 mm plate just before and just after the start of the loading process. We can see from the patterns in Figure 4.53a in the glass that under its self-weight, the top plate has sagged, but is still relatively flat. However, as soon as load is applied, the center portion of the top plate deforms a lot. The reflections in the glass show the ripples around the edges.*

4.5.5 DIC data: 1.1 mm panel

The final two displacement curves are shown in Figures 4.54 and 4.54. The former shows that all points on the loaded diagonal of the top plate have the same vertical displacement throughout the experiment. This means that the loaded diagonal is almost perfectly straight from the start. The deformation only happens in one direction, from support to support, and the top plate has no resemblance whatsoever with a hypar.

The bottom plate behaves differently. When taken off the temporary supports, the center moves up and the corner moves down. When the load is introduced, the corner moves down first, while the center stays up. This means the supported diagonal is straight, while the loaded diagonal is curved. Point 2 also moves upwards, to approximately the same level as point 3. This is likely caused by the horizontal component of the load that causes the bottom plate to buckle upwards. At that point the bottom plate has a relatively straight section in the center, but curves strongly towards the edge, to match the angle of the corner. This strong curvature is possible because the glass is so thin, as well as strong due to the chemical toughening. This shape remains until the bottom plate breaks just after t = 70s.

The large curvature near the corner, caused by the fact that the center of the bottom plate is pushed upwards, but the corner is supported by the frame, is most likely the cause of the failure of the bottom plate. Because the center of the plate is pushed upwards by the horizontal component of the load, but the corners are supported, it even causes the glass near the frame to bulge out. This can be seen in Figure 4.56

As to why the top plate breaks into the long, thin rods described in Paragraph 4.4.4, perhaps the data in Figure 4.54 is the answer. All the points have near enough the exact same vertical displacement throughout the experiment. This means that the loaded diagonal is straight, and curvature (and thus principle strains and stresses) only exists in the direction of the supported diagonal. The fact that the displacement is so high at the end of the experiment means that the radius of curvature is very strong, possibly around $1 - 1.5$ m, which is very low for cold-bent glass. This one-directional stress field is likely to have caused an initial crack perpendicular to that stress field. However, this does not explain the large amount of glass rods.

In order to really know what causes this, the stress would have to be measured. The use of a high-speed camera may also bring some clarity. It is hypothesised that it may be caused by cascading fractures. Strangely enough, the properties of the thin chemically toughened glass may be comparable to that of spaghetti, i.e. flexible but brittle, and therefore the mechanics of fracture may be comparable. The fractural behaviour of spaghetti is described by Audoly (2005): 'when a bent rod reaches its limit curvature and breaks at a first point, a burst of flexural waves described by a universal self-similar solution is sent through the newly formed fragments, which locally further increases the curvature. The limit curvature is therefore exceeded again at a later time, allowing a cascading failure mechanism to take place.'

Due to the small radius of curvature, a high amount (relative to the thickness of the glass) of elastic energy is stored in the glass. When the initial crack occurs, the pieces of glass that are split from each other very quickly release their elastic energy by straightening. Because the curvature is high and the glass is brittle, this way of fracturing may be a kind of two-dimensional version of the cascading fractures that Audoly (2005) describes.

Though no measurements were made, we can roughly estimate the stress in the top plate at the moment of fracture. For this, we assume that all the curvature happens in the central part of the glass. Basically, the panel is made up of two flat, but angled, triangles, connected by the curved glass along the loaded diagonal. From the displacements, we can determine that both 'triangles' are angled about $25-30°$ downwards, so the total angle to overcome is $50-60°$. In the corners, this change of angle needs to happen in the space of 50 to 150 mm. If we take 150 mm as the arc length, we can calculate that the radius of curvature is 170 mm (with a total angle of 50°) or less. With a glass thickness of 1.1 mm and a Young's modulus of 70 GPa, this would result in a tensile stress of at least 225 MPa. Testing by AGC showed a tensile strength of CT

Falcon glass with similar specifications (8 hours of chemical tempering) to be around 320 to 330 MPa, so around 50% higher. However, the parameters to determine the failure stress of the top plate were not measured, and therefore have the large error margins that were mentioned. For example, if the arc length is estimated to be 120 mm instead of 150 mm, which is a reasonable assumption, the failure stress is 335 MPa. In the corners, where the gap is only about 14 mm, it is likely that the silicone deforms a lot, to get a similar radius of curvature in the glass as the unsupported glass. In the end, if we do reasonable assumptions, the failure stress in the top plate is estimated to be between 250 and 400 MPa. This is a wide range, but since tests from the manufacturer have determined the failure stress to be around 325 MPa, the failure stress of the top plate of the 1.1 mm panel was likely near this number.

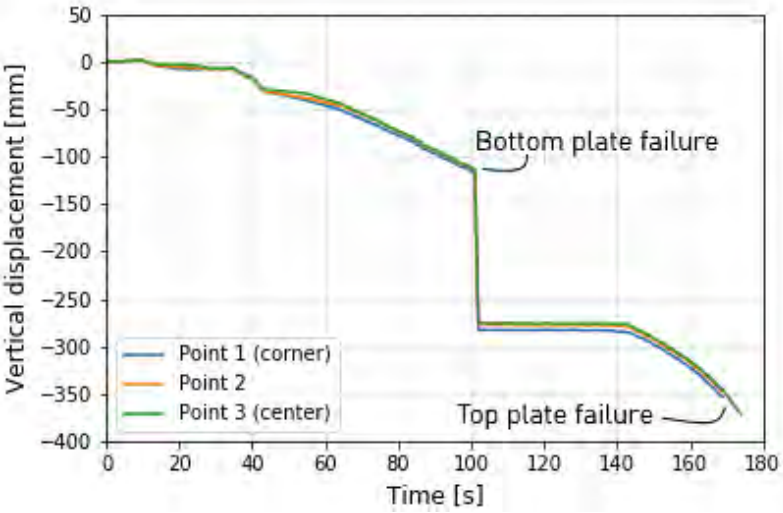

Figure 4.54: *Vertical displacement versus time of the bottom plate of the 1.1 mm panel. All points follow almost the exact same displacement curve, meaning the loaded diagonal is straight from start to finish.*

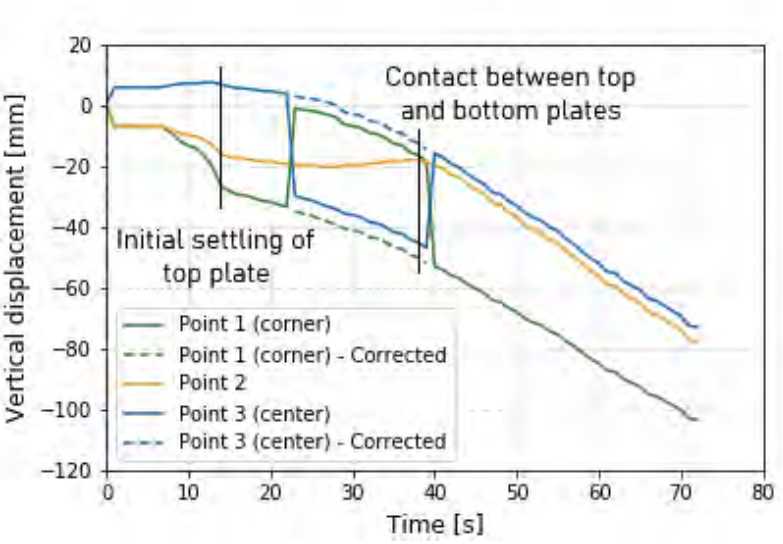

Figure 4.55: *Vertical displacement versus time of the bottom plate of the 1.1 mm panel. Although all points move in a continuous way, without big jumps, the displacement data shows big jumps. This means some kind of measurement error is occurring in GOM Correlate, so the data is corrected to form the dashed lines. These show a more accurate representation of how the displacement curve should be.*

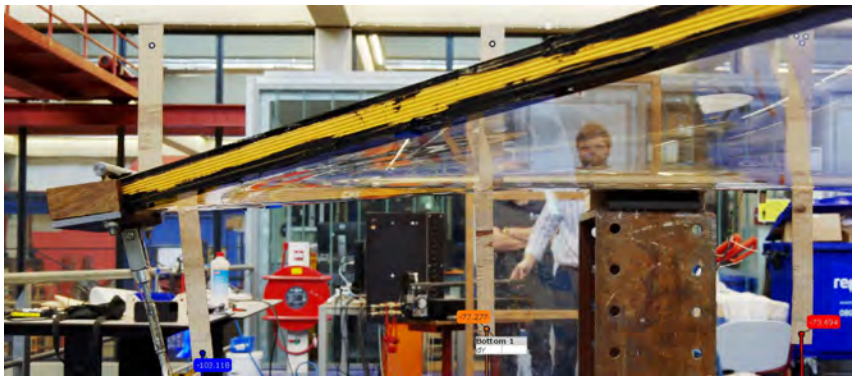

Figure 4.56: *The bottom of the 1.1 mm panel just before the bottom plate breaks. Note the strong curvatures in the corner area near the edges of the glass.*

4.6 Comparison with numerical model

With all the experimental data processed, it can be compared with the numerical model. Figure 4.57 shows the corner load vs corner displacement of the 4 mm panels, both the DIANA model and the experimental results.

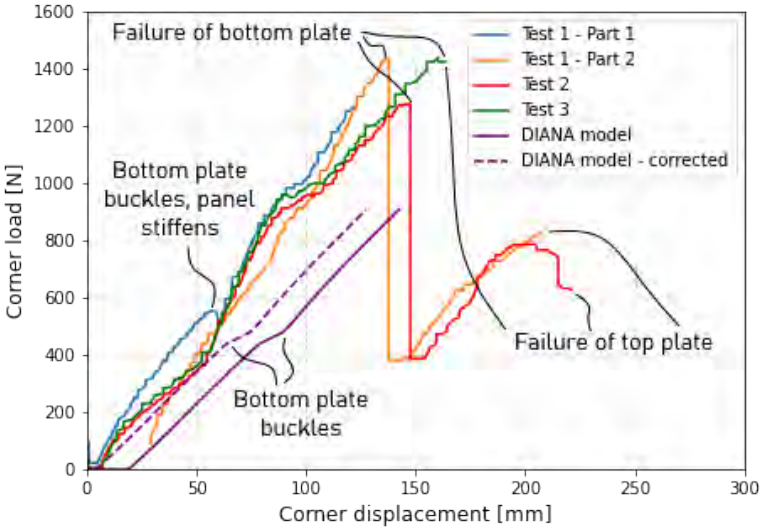

Figure 4.57: *Comparison between the 4 mm panels of the numerical (DIANA) model and the experiments. Load vs displacement is plotted at one of the corners. The model is fairly accurate for the first phase and matches the first part of test 1 in terms of the bottom plate straightening, but loses accuracy after the plates touch. The dotted line is the model, with a correction for the overestimation of the sagging due to self-weight.*

The first thing to note is the discrepancy in displacement due to self-weight. Even though the real-life panels are more heavily loaded with self-weight due to the corner details, the weight of which is not directly modelled, the model still has a significantly higher displacement. All 4 mm panels sag around 7 mm in the corners when taken off the temporary supports, while the model sags almost 20 mm. This difference is likely due to differing boundary conditions. The supports in the model are placed further towards the corners, and the height of the support and load blocks causes a rotation, which adds additional vertical displacement. However, the exact reason could not be investigated due to constraints in time and computation power.

During the first phase of load application, the model matches the stiffness of the real panels reasonably well. Especially the slope of the first part of test 1 is very similar, but the model is also not too far off from tests 2 and 3. The resemblance to the first part of test 1 continues, because the change of shape of the bottom panel and the resulting drop in displacement occur at almost the exact same moment. Though a small difference is that the load drops slightly in the experiment, which is not possible in the model, as it is force-controlled. After contact is made between the top and bottom plate, however, the model loses accuracy. Where the experiments show an increase in stiffness that slowly decreases again, the model continues with a linear stiffness.

The model can also be compared to the DIC data. By plotting the displacement at the same positions as the points for the 2D DIC, the displacements can be directly compared. In Figure 4.58, the vertical displacement of the points on the top plate are plotted for the model and the third test. The model is compared with the third test, because DIC data exists for both the top and bottom plate.

Other than the previously described difference in displacement due to self-weight, there are large differences between the model and reality, but also some similarities. When the corner load is first applied in the experiment, the vertical displacement quickly rises. This phase is missing in the model. However, the stiffness of the model, as well as the behaviour of the plate afterwards, is quite similar for the next stage. In the model, points 2, 3 and 4 have the same displacement, and the corner (point 1) has a higher displacement. This behaviour is very similar to that of the real panel. The corner load at which the top and bottom plates touch is also similar, though not identical. After that, the model is far stiffer than the real panel, and is missing the final change of shape that occurs in the experiment at about 950 N.

Figure 4.59 shows the same comparison for the bottom panel. There is a similar split between the corner en center points in both models, that happens when the supported diagonal straightens. However, this happens a lot later in the model than in the experiment. In terms of stiffness, the accuracy of the model is relatively poor. The overall average stiffness is relatively similar, but the trajectory that leads to that average stiffness is very different.

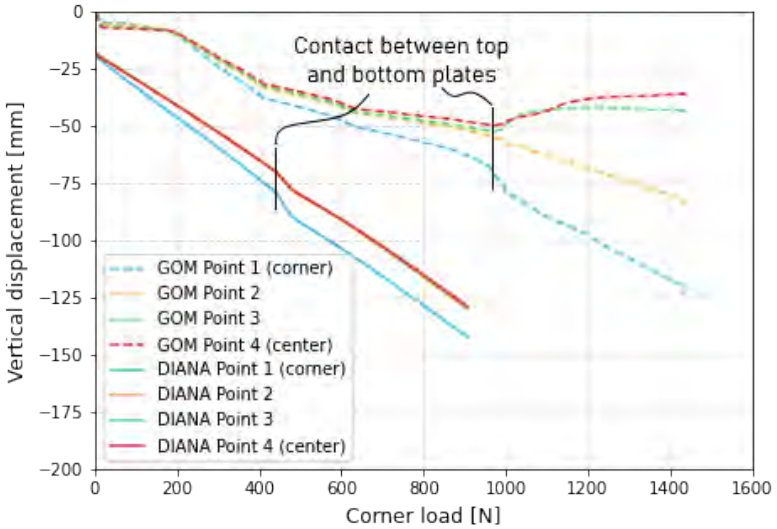

Figure 4.58: *Comparison of several points on the top plate of the DIANA model and the third test of the 4 mm panels. The model matches the real panel in stiffness in the second phase of the experiments, as well as the difference between the corner and center points, but is lacking significantly after the plates have touched (around 400 N).*

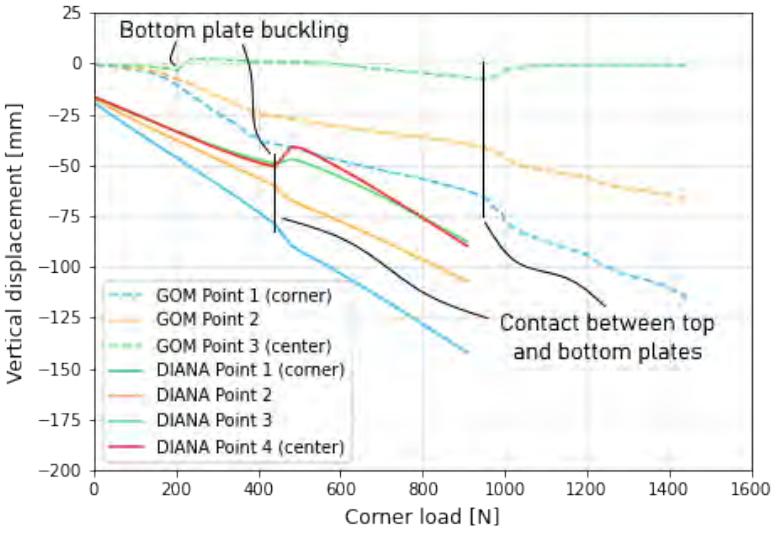

Figure 4.59: *Comparison of several points on the top plate of the DIANA model and the third test of the 4 mm panels. The behaviour of points 2 and 3 of the model resembles that of the corresponding points in the model at the start, but the overall behaviour of the model is not close to the real panel.*

Finally the shear in the silicone adhesive layer is examined. In Figure 4.60 the shear in the top silicone layer is plotted, and in Figure 4.61, the shear on the bottom is plotted. The shear was measured using the LVDTs shown in Paragraph 4.2.3, at 30 cm from the supported corners. The LVDTs had an output in mm, so the 'shear' that is plotted here is a movement of the glass relative to the frame. Positive or negative shear is a matter of sign convention, what matters most is the behaviour of the shear relative to the other panels. In case of the DIANA model, the shear could not be directly measured in millimeters, so it was calculated using the method shown in Appendix B.

In the shear graph of the top of the panel, we can see that the shear behaviour of the panels was not very consistent. In test 1, the shear is very different from tests 2 and 3, especially the second part of test 1. In the first part of test 1 we do see a temporary reduction in shear when the bottom plate straightens, after which the shear steadily increases. In test 3, there is a sudden increase in shear after around 900 N, which is a difference that is not present in the other available data. The amount of shear in the model is closely matched with the shear in the physical panels, at least until the bottom plate straightens. Then, the shear in the model decreases, whereas the shear in the physical panels does not.

The erratic behaviour of the shear continues in the next graph in Figure 4.61, in which the shear is plotted for the bottom of the panel. In this case the model matches reality even better. The start of the model's graph is about the average of all the experiments' graphs. When the bottom plate straightens in part 1 of test 1, which is matched by the model, the shear of the model acts remarkably close to that of the test. After that, the shear continues to be quite close to test 3 and the first part of test 1.

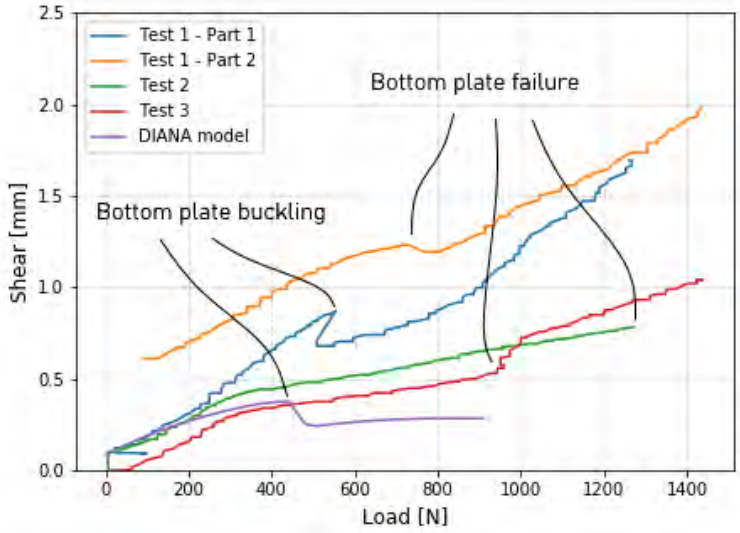

Figure 4.60: *Shear, i.e. movement of the glass relative to the frame, of the top of all 4 mm panels, as well as the model. The shear is plotted against the corner load.*

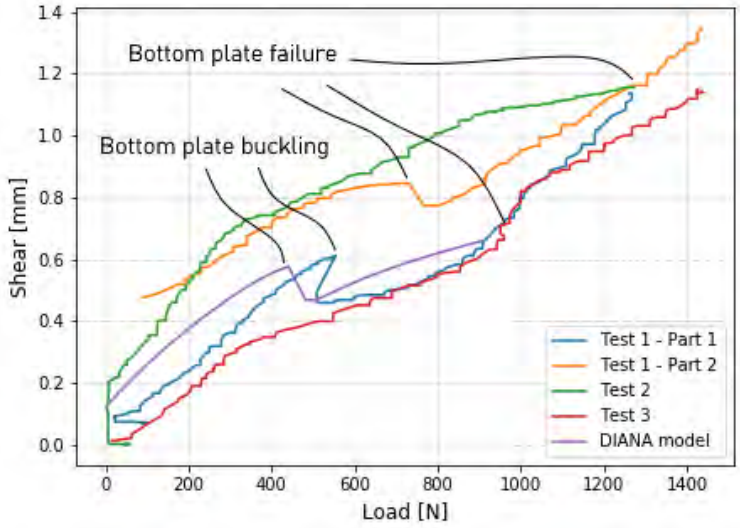

Figure 4.61: *Shear, i.e. movement of the glass relative to the frame, of the bottom of all 4 mm panels, as well as the model. The shear is plotted against the corner load.*

5

Discussion

In the discussion chapter, the methodology and results of the conducted research are discussed. This is split up into a part about finite element modelling, and a part about the experiments.

5.1 Finite element modelling

Computation power: The author had limited computation power throughout the research. Since all research had to be done at home due to the COVID-19 pandemic, all numerical simulations had to be done on consumer computers. These were easily powerful enough to handle finite element analyses, but once the models started getting complex, the simulations can take a full working day. This is because the full model consisted of about 180,000 elements. With 8 GB of RAM in 6 cores available on the PC that was used, this meant the full analysis would take 6 to 8 hours. When trying to fix an unfamiliar issue, this can quickly take a week or more. This hampered progress during the modelling stages, and caused several issues to go unfixed. Perhaps it would have helped to have closer contact with an expert in DIANA, for example by having one in the graduation committee. Having a FEA expert in the committee was helpful, but some DIANA-specific issues may have been solved sooner by having a dedicated person to ask for help.

Contact modelling: Due to the aforementioned issues with computation power, analysing the contact between the top and bottom plates of the panels had to be done in a less elegant way. The use of contact elements in an implicit solver like DIANA proved to be difficult to get right, and in the interest of time, the use of springs was chosen instead. With the use of springs, the contact was more difficult to define, as the right stiffness curve had to be found, which took time. The end result of the contact modelling was highly dependent on this stiffness curve, which makes it more sensitive to errors as well.

Boundary conditions: Between the finite element models and the experiments, the boundary conditions for loading and supports are not exactly the same. The outlines for the finite element model - including the boundary conditions - were created first. The set-up for the experiments was initially designed to recreate these boundary conditions, but, due to budget constraints had to be changed (see Section 5.2). The final design included a corner detail that may have affected the stiffness of the panels by slightly clamping the corners, even though it was attempted to avoid this. The boundary conditions of the supports were also not entirely the same, possibly leading to an overestimation of the sagging due to self-weight in the model. This issue was not investigated further, because the lack of computation power made it difficult to try different solutions, and fully modelling the corner details would have greatly increased computation time.

Quadratic elements: In the model build-up, it was noticed that the use of quadratic elements improved the accuracy of the intermediate stages in building the model by about 10%. However, analysing the complete model using quadratic elements was simply not feasible. The analysis would have taken literal days, while the occupied computer can hardly be used for anything else. Therefore, the use of linear elements was chosen. However, in tests with only self-weight, a difference of less than 3% was noticed between the results of the model with linear or quadratic elements, so this may not be a big issue.

5.2 Experiments

Experimental set-up design: The final version of the set-up used for the experiments was designed with space and budget constraints as the main outline. Therefore, the initial design, where the load was introduced from above, could not be used. Most importantly, this led to the load being introduced from below the panels, which required a heavy and cumbersome corner detail. The fact that this corner detail could slide off the corner if the loading cables came from directly below meant that the cables had to arrive at an angle. The horizontal component of the load that was introduced along with this was not enormous, as the angle was small, i.e. less than 12° maximum. This caused a maximum horizontal load of 100 N, so it likely did interfere with the shaping process. In case of the 1.1 mm panel, it likely caused premature failure of the bottom plate.

Stress measurements: Also because of budget constraints, a very limited amount of measurements could be done. The 3D DIC system could not be used on all tests, but a 2D DIC system was put together to mitigate that problem. Stress measurements were not performed, so this would be a possible improvement for further work. This would provide more insight into the panels' behaviour, and give a more complete comparison with the numerical model.

Statistical significance: Due to the limited amount of materials, only four test specimens could be made. Of those four, three were of one type, and one of another type. Changes needed to be made to the set-up after the first test, which meant that in the end there were only two tests that were directly comparable. Sample sizes in civil engineering research are often small, but to really increase the understanding of a new type of building product, more data has to be gathered.

2D DIC scale: For the software to be able to calculate the displacements in the 2D DIC, the scale needs to be set. In this research, the black-and-white dots were used for this purpose. However, the resolution of the camera was such that when setting the scale, some ambiguity existed on where the edges black-and-white were exactly. This may have led to minor (likely $< 5\%$), but unnecessary measurement errors. It would have been better to have a larger object with a known scale on the plane of the measured points.

6

Conclusions and recommendations

Through the use of a literature review, numerical modelling in the form of finite element analyses, and physical experiments, the behaviour of an cold-twisted IGU stiffened by a frame was investigated. Here, we draw conclusions from the results of the research, and propose recommendations for further research.

6.1 Conclusions

Main research question: how can the structural behaviour of a cold-twisted insulated glazing unit with a rigid frame be predicted? A finite element model was set up to predict the behaviour of the cold-bent panels. This model can fairly accurately (error within about 15%) describe the initial stiffness of the 4 mm panels that were tested. The model does sag too much under its self-weight, which is likely due to the modelling of the boundary conditions and load introduction. The buckling of the bottom plate also matches some of the experimental results, although those were not consistent with each other. After the plates start touching in the center, however, the model loses accuracy, and cannot be used anymore to predict the outcome of the experiment. In terms of shear in the silicone adhesive, the same applies. The model matches the experimental results in the beginning, but loses accuracy once the real panels start taking on more complex shapes. Only the 4 mm panels were modelled in the end, as the available computation power was not enough to model the 1.1 mm panel within a reasonable amount of time.

Spacers and adhesive: For the purpose of this research, GFRP spacers were chosen. Higher longitudinal stiffness was desired, to help the formation of a hypar, while low torsional stiffness was preferred, to minimise constraining of rotations at the edge. For obvious reasons, low weight, sustainability and high insulation values were preferred. GFRP has multiple of the aforementioned qualities, but the choice was made primarily because of its low weight. However, even with the relatively thin, and thus flexible, glass that was used, the GFRP spacers did not provide enough stiffness to the edges. Therefore, other materials should be considered again. Aluminium is a good candidate, because it is almost three times stiffer, while it is still relatively low-weight. Several options were looked at for bonding the spacers to the glass. DOWSIL 993 Structural Glazing Sealant was chosen for its combination of flexibility (approximate Young's modulus of 1.5 MPa) and strength (tensile strength of 0.95 MPa). During the modelling and experiment phases, it became clear that the edge spacers were not stiff enough. However, this was not due to the adhesive, although if a stiffer spacer is used in future developments, it needs to be evaluated if a higher strength adhesive is required.

Silicone modelling: To model silicone, a hyperelastic material model is the most accurate. Not only was this concluded from literature, but also from recreating several experiments. In DIANA, the Mooney-Rivlin model worked best for simulating the D993 silicone that was used in the experiments. In the mesh study that was performed, it was found that for the dimensions used, i.e. silicone joints of 6 mm thick and 24 mm wide, it was best to use 4 elements over the height of the silicone, and 3 over its width. This provided a good compromise between accuracy and computation time. Brick elements for rubber solids (element type HX25L)

were used to model the silicone, which were good for modelling the material behaviour, but are a limitation because they cannot be used for triangular shapes, which resulted in meshing issues.

Cavity pressure modelling: When modelling cavity pressure due to an external load, equilibrium needs to be found between the volume, the external load, and the internal pressure. To reach this equilibrium, a three-guess system was developed that can be used in with any type of IGU in any type of finite element software.

Contact: Contact between the top and bottom plates was observed in the experiments and subsequently modelled in the FE-model. With a cavity width of 42 mm in all panels, the plates made contact at a corner displacement of 50 to 60 mm in the 4 mm panels, and 40 to 50 mm in the 1.1 mm panel. Modelling contact in an implicit solver like DIANA turned out to quickly lead to convergence issues. A possible solution is to use interface elements such as springs, instead of contact elements, but one needs to be careful of its limitations, such as the inability to model friction.

Hypar with stiffened edges: From literature, it seemed like stiffening the edges of a glass plate was a good way of forming a hypar with more extreme curvatures. Forming a hypar in this way would stiffen up a glass with a relatively low thickness, either a single plate or an IGU. This would give a geometric stiffness to the glass, leading to a lower required thickness. To test this, two panel types with different glass thicknesses were built and formed in a way that was intended to create a hypar, both in a numerical model and in physical tests. However, due to the self-weight of the glass and the panels, the hypar was never formed. Instead, the glass was curved mostly in one direction.

Since the panels were designed with use in a curtain wall in mind, one might consider shaping them in vertical orientation to avoid gravity from interfering with the hypar shape. However, once a wind load would be applied, this would quickly be more than the load of the self-weight, which would likely lead to the buckling effect that was to be avoided. Therefore, however the panel is shaped, the low stiffness will remain problematic. This could be solved by using thicker glass, though still thinner than with a flat IGU, or possibly be using stiffer edge-spacers.

Hypars from thin glass: It seems unlikely that forming a hypar is a good way of using thin (< 2.1 mm) glass in building applications. The out-of-plane stiffness is so low, that it would need a high degree of curvature to gain any kind of geometric stiffness, by which time one of the corners has buckled. Even with stiffened edges, it is unlikely the necessary curvature can be achieved.

6.2 Recommendations

Hypars: This research showed that with glass sheets with a low thickness-to-size ratio, it is difficult to form a hyperbolic paraboloid. Even with stiffened edges, both the 4 mm panels and the 1.1 mm panels could not form a stable hypar. That is not to say that the use of hypars in façades is not worth pursuing. Sheets of glass with higher thickness-to-size ratios can still be cold-bent into a hypar. This will provide the glass with a geometric stiffness, leading to the possibility of weight loss. Future research could focus on the thickness ratio of the glass that would lead to the best results, i.e. thick enough to be possible to form a hypar, but not so thick that the energy input becomes to great, and adhesives will have trouble holding it. It is not recommended to use the sandwich panel IGU for anything other than a hypar, e.g. a single-curved shape. In a single-curved shape, the edge stiffness would be disadvantageous. Most of the panel would be kept mostly straight by the spacers, forcing the center of the glass to strongly curve to achieve the desired change in angle.

Joint design: In this thesis, the design of a joint for the frame was skipped. It was decided to focus on the behaviour of the glass during the bending process, as that was where the largest knowledge gap was. However, if this method of shaping glass is to make it to a building product, a joint needs to be designed to use in the corners. The joint would have the requirement of being a hinge during the shaping process, but a fixed connection when the glass has reached its final shape. Many interesting engineering challenges lie in the design of such a joint, so this would be a good way of adding to the current topic.

Case study: As a proof of concept, it would be interesting to see a case study done with hypar-shaped IGUs. A standard flat curtain wall with a steel or aluminium substructure could be designed or taken from an existing design. Then it would be replaced by an array of hypars. To see if bending the glass in this shape is actually beneficial, a full life-cycle analysis would have to be performed, where the main interest is the embodied carbon in the glass, and the greenhouse emissions during the fabrication and shaping processes. The results of such a study could lead to an expansion of architects' and engineers' toolboxes for designing building façades.

Sandwich panel: As mentioned in the conclusions, the GFRP spacers did not provide enough stiffness for the panel sizes that were used. Given the fact that it is not desirable to use much smaller panels, it may be good to examine other materials for the spacers. A stiff but light material such as aluminium would be preferred. The adhesive choice would also have to be re-evaluated in that case.

The contact between the plates is obviously problematic and needs to be addressed. Possibly the use of stiffer adhesives could provide a solution. Perhaps the spacers need to be bigger, or the limit of corner displacement must be kept low.

Climatic pressures also need to be investigated. The use of low flow-rate valves was proposed in this research, but it needs to be investigated if this is a viable option. Desiccation needs to be taken into account in such an analysis. For example, in a system with multiple IGUs, is it better for each IGU to have its own way of desiccation, or would a decentralised system where all IGUs are connected be better?

References

Audoly, B. (2005). Fragmentation of Rods by Cascading Cracks: Why Spaghetti Does Not Break in Half. *Physical review letters*, 95.

Bigoni, D. (2012). Nonlinear solid mechanics: bifurcation theory and material instability. *Cambridge University Press*.

Boyle, R. (1660). New Experiments Physico-Mechanicall, Touching the Spring of the Air, and its Effects (Made, for the Most Part, in a New Pneumatical Engine) Written by Way of Letter to the Right Honorable Charles Lord Vicount of Dungarvan, Eldest Son to the Earl of Corke.

Datsiou, K. (2018). Design and Performance of Cold Bent Glass (Doctoral dissertation). *University of Cambridge, Cambridge, United Kingdom*.

Datsiou, K.G. Overend, M. (2014). Behaviour of cold bent glass plates during the shaping process. *Engineered Transparency conference*, pages pp. 125–133.

Dockerty, S. (1967). Sheet forming apparatus. *Patent: US 3338696 A*.

Dos Santos, D., Carastan, D., Tavares, L., and Batalha, G. (2014). Polymeric Materials Characterization and Modeling. *Comprehensive Materials Processing*, 2: pp. 37–63.

Dow (2018a). Behavioral Data Sheet: DOWSIL^{TM} 993 Structural Glazing Sealant. *The Dow Chemical Company*.

Dow (2018b). Finite Element Analysis Calibration Exercise with DOWSIL^{TM} 993. *The Dow Chemical Company*.

Fedoseeva, Y. (2017). Cold bent gfrp-glass panels. *University of Cambridge*.

Feldmeier, F. (2003). Insulating units exposed to wind and weather–load sharing and internal loads. *Glass processing days*, pages pp. 633–636.

Galuppi, L. (2014). Buckling phenomena in double curved cold-bent glass. *International Journal of Non-Linear Mechanics*, 64: pp. 70–84.

Galuppi, L. (2019). Betti's Analytical Method for the load sharing in double glazed units. *Composite Structures*, 235.

Glasscon (2018). Structural Report 1193/2017.27.01 (Revision 3) on Glass Façades for Rothschild 48, Tel Aviv. *GLASSCON GmbH*.

Haines, D. and Wilson, W. (1979). Strain-energy density function for rubber-like materials. *Journal of the Mechanics and Physics of Solids*, 27: pp. 345–360.

Leslie, T. (2008). "As Large as the Situation of the Columns Would Allow": Building Cladding and Plate Glass in the Chicago Skyscraper, 1885-1905. *Technology and Culture*, 49: pp. 399–419.

Love, A. (1888). XVI. The Small Free Vibrations and Deformation of a Thin Elastic Shell. *Philosophical Transactions of the Royal Society of London*, 179: pp. 491–546.

Marinov, V. (2012). Optimisation of Curved Insulated Glass. *Unpublished manuscript.*

Martins, P., Natal Jorge, R., and Ferreira, A. (2006). A Comparative Study of Several Material Models for Prediction of Hyperelastic Properties: Application to Silicone-Rubber and Soft Tissues. *Strain*, 42.

Mooney, M. (1940). A Theory of Large Elastic Deformation. *Journal of Applied Physics*, 11: pp. 582–590.

Mott, P. and Roland, C. (2009). Limits to Poisson's ratio in isotropic materials. *Physical Review B*, 80.

Muhsin, N. and Hassan, M. (2010). Hyperelastic Constitutive Modeling of Rubber and Rubber-Like Materials under Finite Strain. *Eng. & Tech. Journal*, 28.

NEN 2608 (2014). Glass in Building - Requirements and determination method.

Nhamoinesu, S. (2015). Steel-Glass Composite Panels. *University of Cambridge.*

Pfaender, H. (1996). *Schott Guide to Glass.* Springer, Dordrecht.

Pilkington, L. (1969). The float glass process. *The Royal Society: Series A, Mathematical and Physical Sciences, London.*

Quaglini, V. (2020). Cold bending of vertical glass plates: Wind loads and geometrical instabilities. *Engineering Structures*, 220.

Rivlin, R. (1948). Large elastic deformations of isotropic materials IV. further developments of the general theory. *British Rubber Producers' Research Association*, 241: pp. 379–397.

Staaks, D. (2003). Koud torderen van glaspanelen in blobs (unpublished master's thesis). *Delft University of Technology, Delft, The Netherlands.*

Van der Linden, A. (2018). Building Physics. *ThiemeMeulenhoff.*

Walker, J. (2004). *Physics, 2nd Edition.* New Jersey: Pearson Education.

Young, R. (2019). Freeform buildings: The design of a cold bent glass panel system. *University of Cambridge.*

Zaccaria, M. and Gillon, X. (2019). Scaling Thin Glass Use to the Architectural World. *Glass Performance Days.*

Appendices

A

GFRP stiffness verification

The supplier of the glass fibre reinforced polymer (GFRP) square hollow profiles did not provide sheets on the technical specifications and properties of the material. They did mention they would provide the exact same profiles as the ones used in the experiments by Young (2019). Since in that report the material properties are given, they are known. However, because the information was not acquired directly from the manufacturer, four point bending tests (FPBTs) were performed with samples of leftover profiles. Because of the constant moment in the center region of a sample in a FPBT, it is preferred to use a FPBT instead of a three point bending test for tests with brittle materials. The intention of these tests was not to break the samples, but the FPBT was still chosen, as the constant moment in the center region would still be a could indication for the stiffness of the material.

The most important part of the verification is the check of the lengthwise elastic stiffness. Firstly because it has a large effect on the stiffness of the panel, so therefore it is important to get the stiffness right in the model. In addition to that, there can be significant variations in the amount of glass fibres put into the profile, which affect the lengthwise stiffness, but not so much the torsional or shear stiffness.

To verify the stiffness properties, first a numerical simulation of the FPBT was done using FEA, and then these were checked with physical experiments. 350 mm specimens were cut of unused pieces of the profiles. For the FPBT, standard dimensions were used: the supports were 220 mm apart, and the loading points were 110 mm apart. The test specimens would be loaded with a little under 10 kN (total load), resulting in a maximum measured displacement of 2 mm.

It was modelled in two ways, both as a one-dimensional beam, and as a three-dimensional object consisting of two-dimensional sheets. For both, the cross-section was slightly simplified as 30×30 mm, top and bottom walls of 2.8 mm thick, and side walls of 3.5 mm, which is the average thickness of the ribbed sides. The 1D beam was given an isotropic stiffness of 26 GPa, i.e. the lengthwise Young's modulus. The 3D model was given the full properties mentioned earlier, in Paragraph 3.2.2:

- $E_1 = 26$ GPa
- $E_2 = E_3 = 8.5$ GPa
- $\nu_{12} = 0.075$
- $\nu_{23} = 0.23$
- $\nu_{13} = 0.38$
- $G = 3$ GPa

The supports were modelled as a pin and a roller, and the load was defined as a prescribed vertical displacement of 2 mm, which would later be the maximum displacement in the physical experiments. Since the deformations would be relatively small and not complex, a linear mesh and a linear analysis were used. The models, displacement fields and reaction forces can be seen in Figures A.1 (1D) and A.2 (3D).

The same FPBT was performed as a physical experiment. 10 specimens were placed in a ZwickRoell Z010 with a load cell of 10 kN. They were all loaded close to the maximum capacity of the machine, resulting in a maximum displacement of around 2 mm. The results can be seen in Figures A.4 and A.5.

In Figure A.4a we can see that both models overestimate the stiffness of the profile. However, this is unlikely to be because of the properties of the profile, as according to these results, it would be 50% less stiff than the specifications. Since this is very unlikely, and both models show this factor 2 in stiffness, the loads in the model are halved. The resulting load-displacement curves are shown in Figure A.4b. In this, we can see that the 1D model is 100% accurate in the linear phase, and overestimates the stiffness by a maximum of 5% at the end. This is logical, because the GFRP is assumed to be isotropic in this model, which means the stiffness is overestimated once the displacement becomes larger and shear deformation starts to take place. The 3D model underestimates the stiffness by about 25%. This is likely because the loads and supports are defined as lines, causing stress concentrations.

In Figure A.5 we see the results of all ten specimens plotted together. This is to show the spread in the results, which is around a 7% difference at maximum, which is to be expected for GFRP.

From these results we can conclude that the stiffness of the GFRP profiles is either the same as the manufacturer has specified, or, in case of the uncorrected results, the stiffness is almost exactly half of what the manufacturer has specified. Given the fact that the latter is very unlikely, we can say that the GFRP has the correct stiffness.

(a) *The FE model with loads and supports shown. Pin and roller supports are used, with two point loads on top. The point loads are defined as a prescribed displacements of 2 mm.*

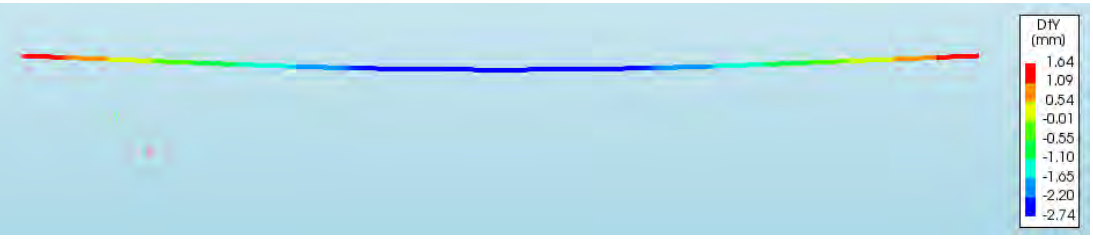

(b) *Vertical displacement plot of the model. Scale factor = 1. The colour scale runs from -2.74 mm (blue) to +1.64 mm (red).*

(c) *Vertical reaction forces as a result of the prescribed displacement. Scale factor = 1. The colour scale runs from -9341 N (blue) to +9341 N (red).*

Figure A.1: *Four point bending tests with square hollow GFRP profiles to verify their stiffness, modelled as a 1D beam in DIANA.*

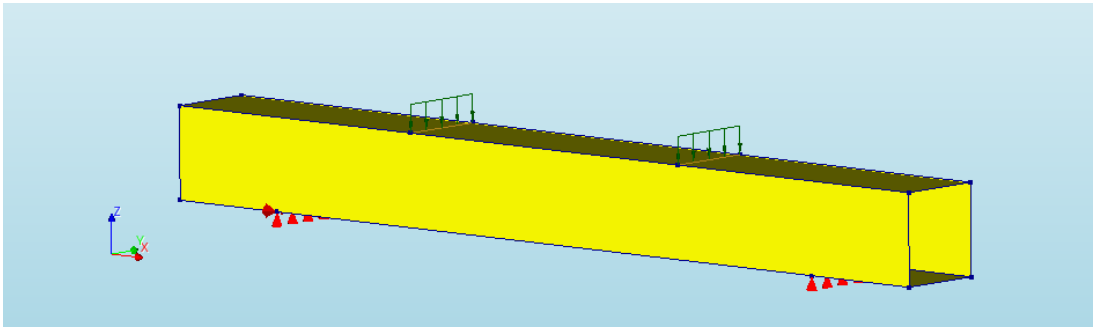

(a) *The FE model with loads and supports shown. Pin and roller supports are used, with two point loads on top. Pin and roller supports are used, with two line loads on top.*

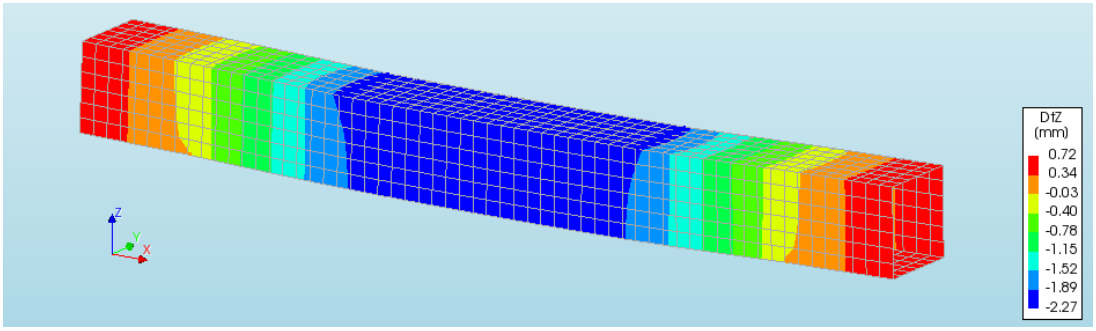

(b) *Contour plot of the vertical displacements. Scale factor = 1. The colour scale runs from -2.27 mm (blue) to +0.72 mm (red).*

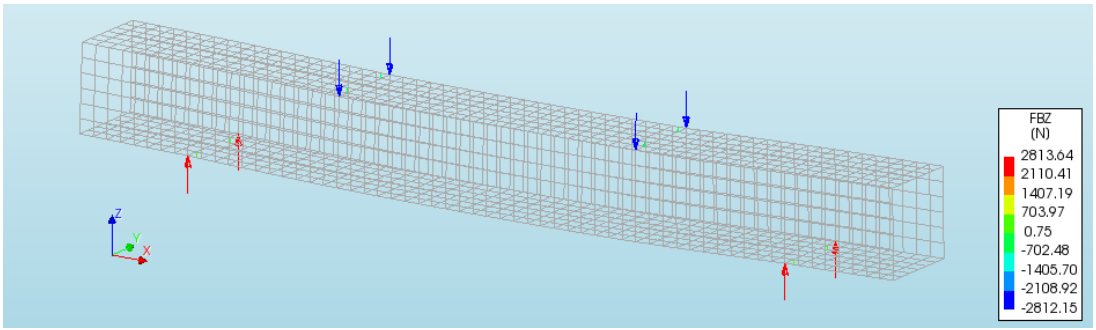

(c) *Vertical reaction forces as a result of the prescribed displacement. Note that most of the force is taken up at the location of the vertical walls of the profile. Scale factor = 1. The colour scale runs from -2812 N (blue) to +2813 N (red).*

Figure A.2: *Four point bending tests with square hollow GFRP profiles to verify their stiffness, modelled by using 2D flat shell elements to create a full 3D model in DIANA.*

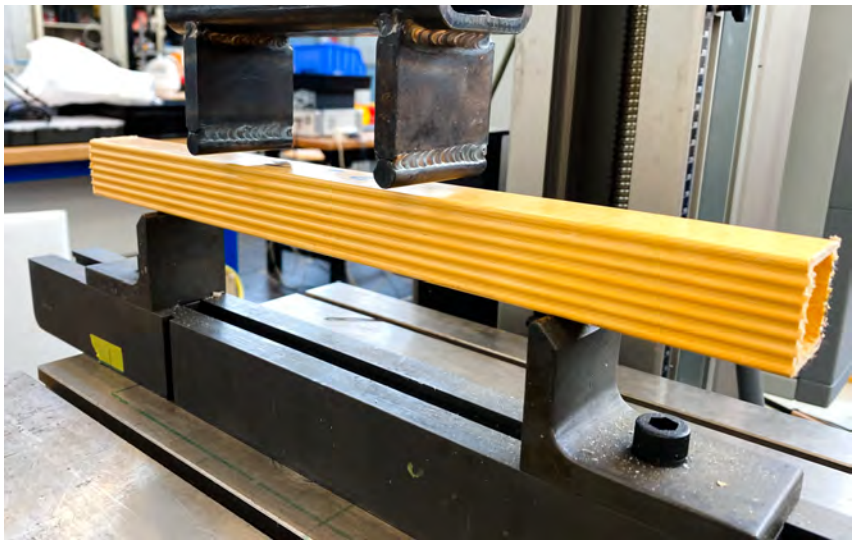

Figure A.3: *Set-up of the four point bending test. The had the cross-section shown in Figure 4.17, and were approximately 350 mm long. The supports were placed 220 mm apart, and the load points were placed 110 mm apart, so each load point was 55 mm from the closest support.*

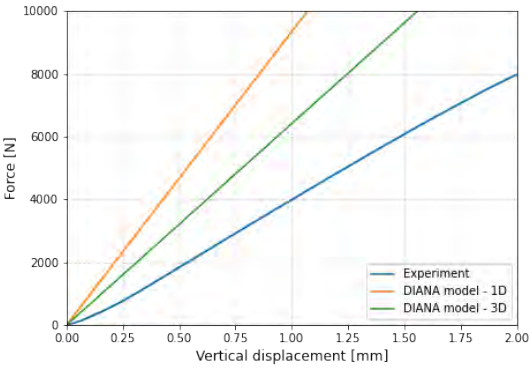

(a) *Total vertical force of the FE models and the experiments plotted against the vertical displacement.*

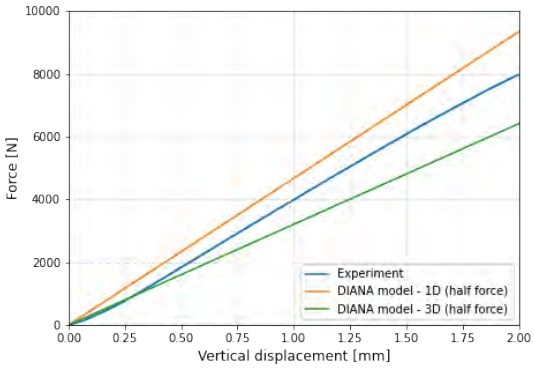

(b) *Half the vertical force of the FE models and the total vertical force of the experiments plotted against the vertical displacement.*

Figure A.4: *Experimental results compared to the results of the finite element models. Force is plotted on the vertical axis, vertical displacement is plotted on the horizontal axis.*

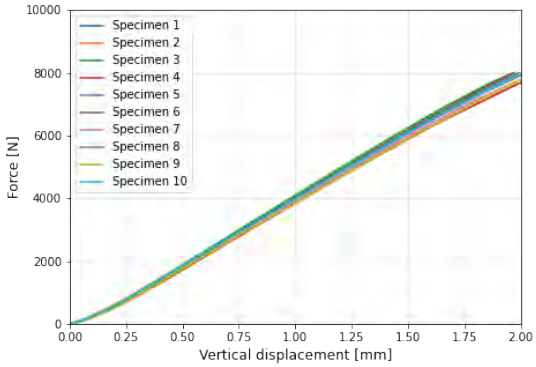

Figure A.5: *Total force vs vertical displacement of all 10 10 specimens of the four point bending test.*

B

FE model shear calculation

It was mentioned in Section that the shear in the DIANA model was not a possible direct output. Therefore, it had to be calculated. In Figure B.1, the geometry that is used to calculate the shear is shown. This is a representation of the glass and the top of the frame, which start out in the reference x-z coordinate system. The panel then translates and rotates into the coordinate system x'-z'. Rotation around the x and y axes are assumed to be negligible.

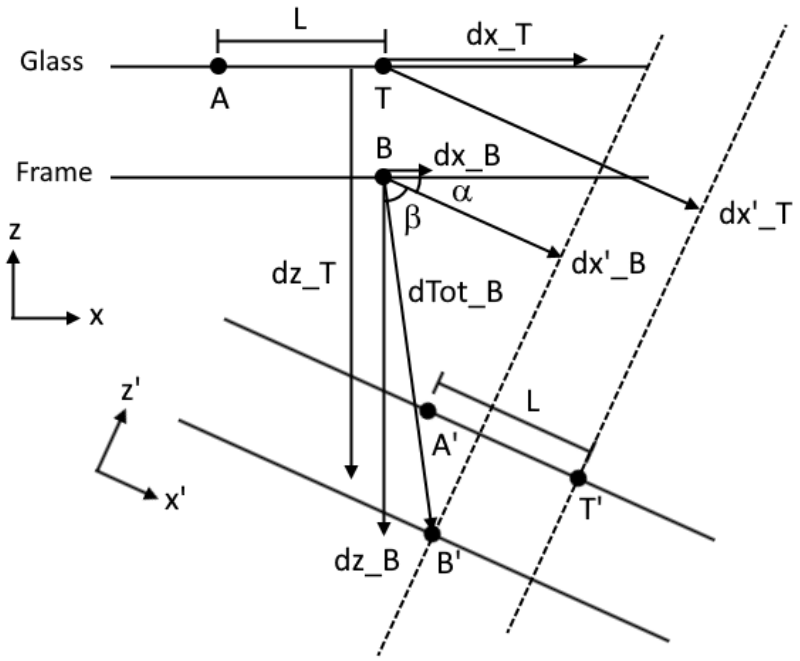

Figure B.1: *Geometry needed for the calculation of the shear between the glass and the frame.*

The desired output is a length in millimeters that represents the relative movement of the glass to the frame. Therefore, we need to use the displacements of a point on the glass and a point on the frame (T for 'top' and B for 'bottom' in the figure) to determine their relative displacements. An additional point 'A' is defined in order to have a length that does not change - or the change is negligible because of the in-plane stiffness of the glass - in order to calculate corner α. This is can be represented with:

$$L = E'_x - T'_x = E_x - T_x = dz_T - dz_E \tag{B.1}$$

We can use this to calculate α, which we assume to be the same for the glass and the frame:

$$sin(\alpha) = \frac{E'_z - T'_z}{E'_x - T'_x} = \frac{dz_T - dz_E}{E_x - T_x} \tag{B.2}$$

$$\alpha = arcsin(\frac{dz_T - dz_E}{E_x - T_x})$$

To get dx' and dz', we need β for both points:

$$\beta_{T/B} + \alpha = arccos(\frac{dx_{T/B}}{dTot_{T/B}}) \tag{B.3}$$

$$\beta_{T/B} = arccos(\frac{dx_{T/B}}{dTot_{T/B}}) - \alpha$$

Where:

$$dTot_{T/B} = \sqrt{dx_{T/B}^2 + dz_{T/B}^2} \tag{B.4}$$

Then we set up the basic formula for $dx'_{T/B}$:

$$dx'_{T/B} = cos(\beta_{T/B}) \cdot dTot_{T/B} \tag{B.5}$$

We then substitute Equations B and B.4 into Equation B.6:

$$dx'_{T/B} = cos(arccos(\frac{dx_{T/B}}{dTot_{T/B}}) - \alpha) \cdot \sqrt{dx_{T/B}^2 + dz_{T/B}^2} \tag{B.6}$$

With this final equation, we can calculate dx' for T and B, and the difference between the two displacements is the shear that can be compared with the experimental results.

C

Additional pictures

In this appendix, some additional photos are shown of the assembly and testing of the panels.

Figure C.1: *The first panel partly dry-assembled.*

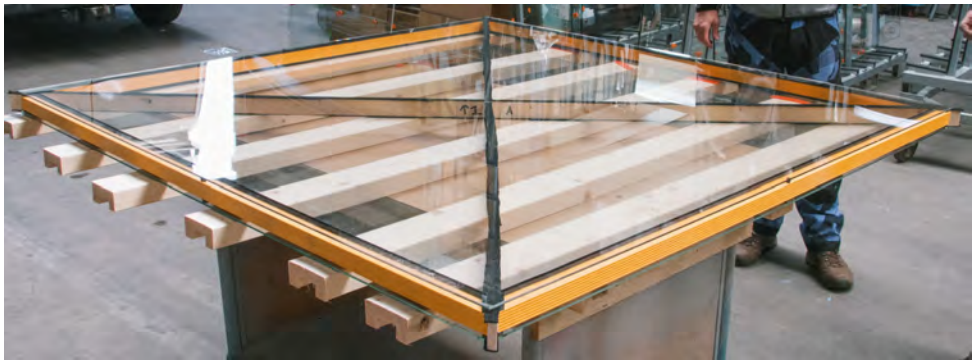

Figure C.2: *The first panel fully dry-assembled*

Figure C.3: *D993 silicone being applied*

Figure C.4: *The machine used for the silicone application.*

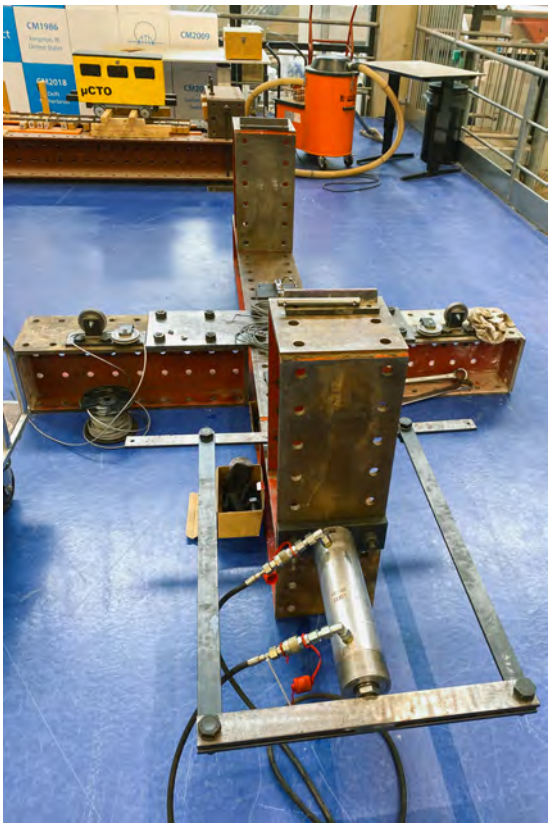

Figure C.5: *The set-up partly assembled, the support blocks would later be replaced with taller ones.*

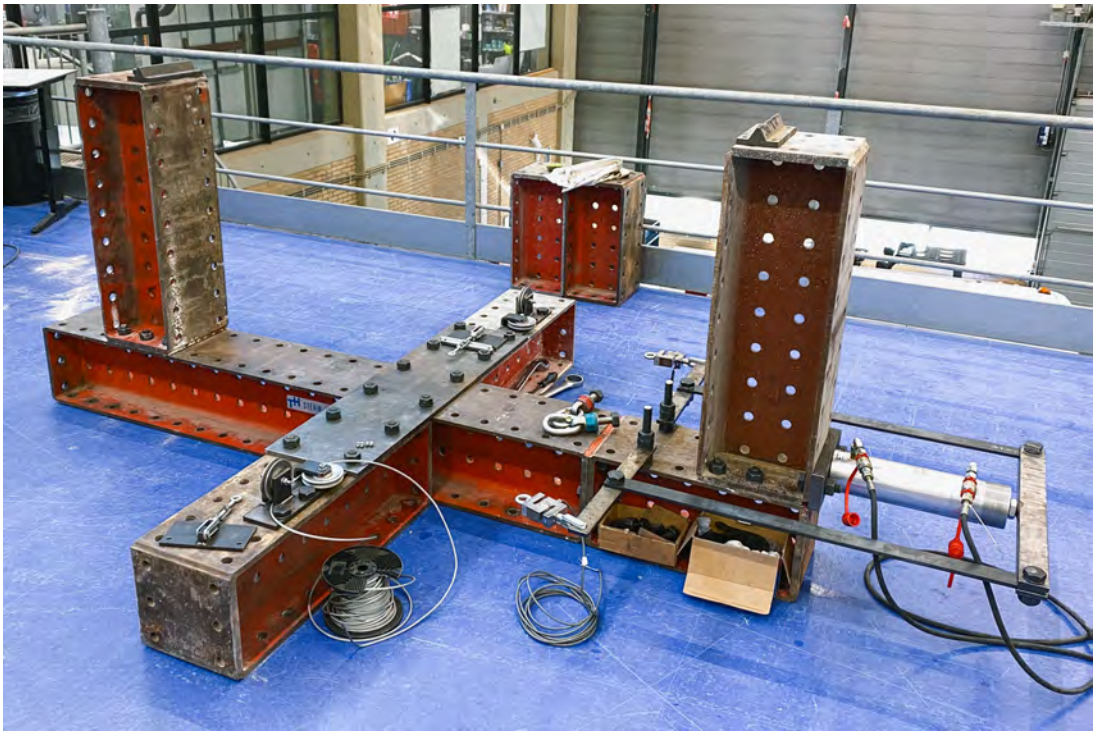

Figure C.6: *The set-up partly assembled, with the taller support blocks in place.*

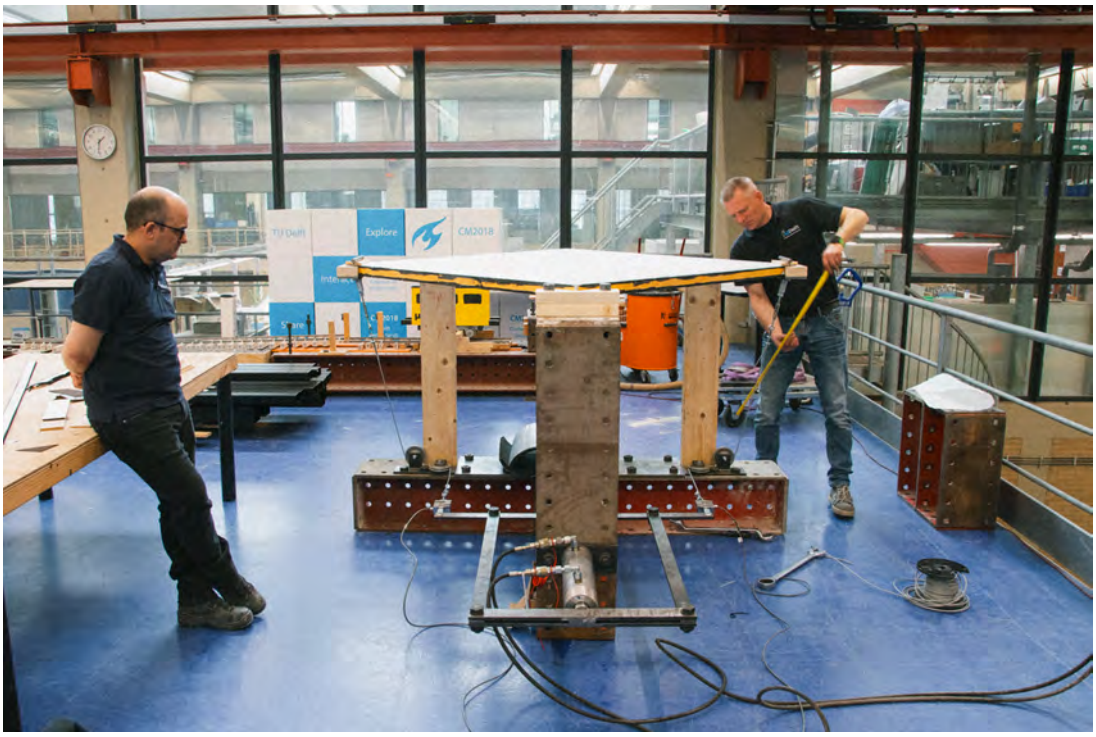

Figure C.7: *The finished set-up with one of the panels in place.*

Figure C.8: *The set-up and its surroundings, showing the relative lack of space around it. Image shot on 35 mm black-and-white film.*

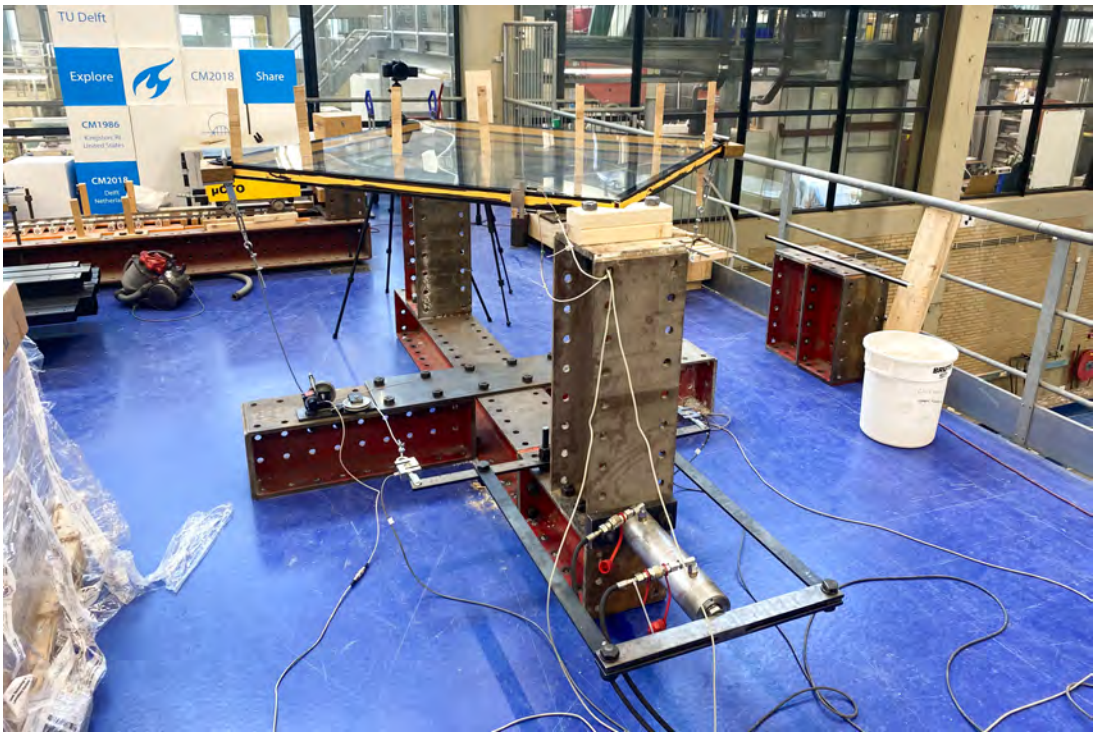

Figure C.9: *The set-up with 2D DIC, not the camera and the wooden strips on the glass.*

Figure C.10: *Setting up the 2D DIC cameras, one for the top plate, and one for the bottom. Image shot on 35 mm black-and-white film.*

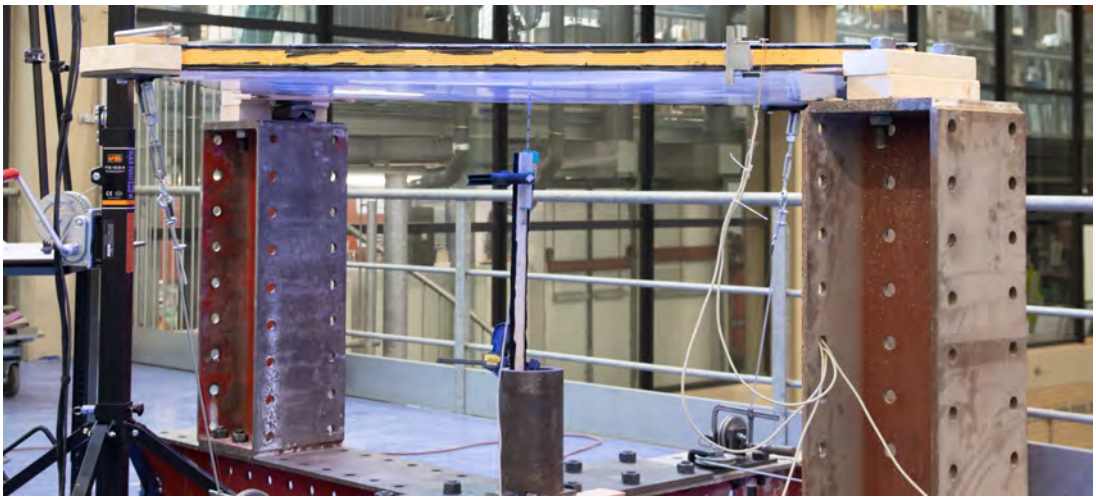

Figure C.11: *The start of the first test, with the temporary supports removed, but no load applied.*

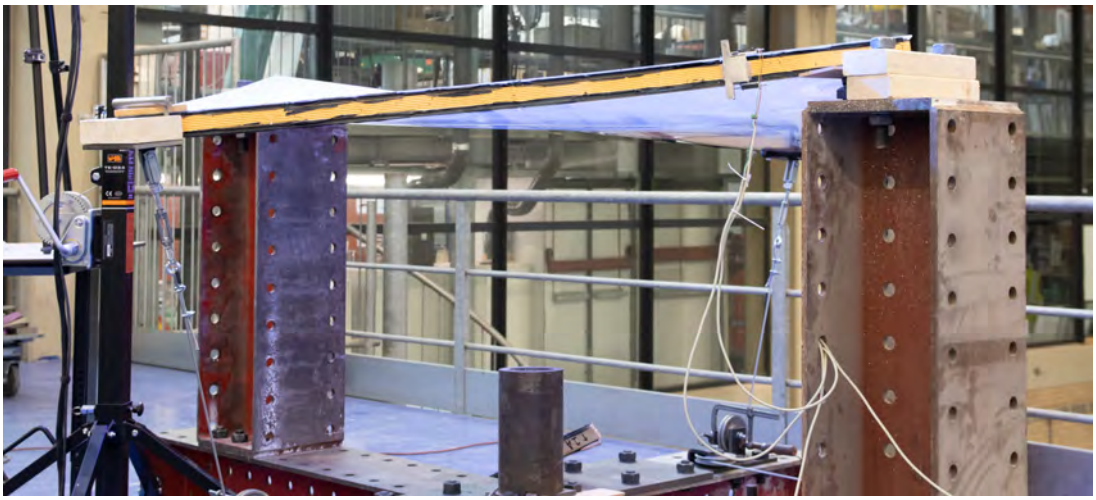

Figure C.12: *The first test, last frame before failure of the bottom plate.*

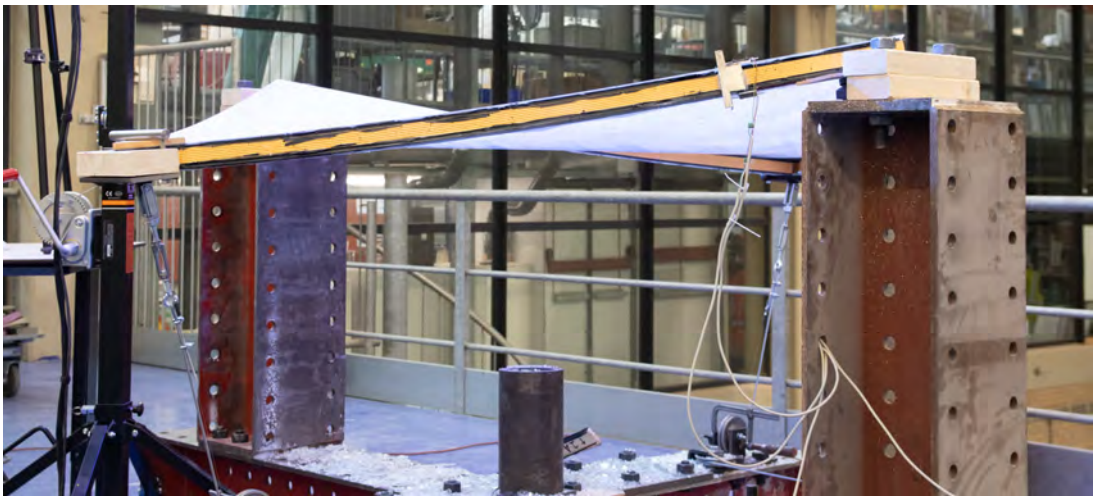

Figure C.13: *The first test, last frame before failure of the top plate.*

Figure C.14: *The glass spaghetti-like rods resulting from the fracture of the top plate of the 1.1 mm panel.*

Figure C.15: *The glass spaghetti-like rods resulting from the fracture of the top plate of the 1.1 mm panel, along with the larger shards of the bottom panel.*

D

Volume and pressure calculation

In this appendix, the Python functions that are used to calculate the internal cavity volume, and subsequently the pressure, are presented. Comments are placed at crucial points to help understand how the functions work.

```
import numpy as np
import scipy.spatial

def read_data(csv_name):
    #Function to read in a results file from DIANA
    #fh, fb are width of the spacer, in this case the spacer is the same along all edges, so fh=fb
    #h, b are the outer dimensions of the panel, in this case h=b
    alldata = np.loadtxt(csv_name, delimiter=',', skiprows=3, usecols=(6,7,8,9,10,11))
    xyfilter_bottom = [(alldata[:,0]>=fb) & (alldata[:,0]<=(b-fb))
             & (alldata[:,1]>=fh) & (alldata[:,1]<=(h-fh))
             & (alldata[:,2]==-0.14)]
    xyfilter_top = [(alldata[:,0]>=fb) & (alldata[:,0]<=(b-fb))
             & (alldata[:,1]>=fh) & (alldata[:,1]<=(h-fh))
             & (alldata[:,2]==-0.1)]

    bottom = alldata[xyfilter_bottom]
    top = alldata[xyfilter_top]

    bottom_start_coords = bottom[:,:3]
    top_start_coords = top[:,:3]

    bottom_deformations = bottom[:,3:]
    top_deformations = top[:,3:]

    bottom_def_coords = bottom_start_coords + bottom_deformationstop_def_coords = top_start_coords + top_deformations

    #return the coordinates of the panel in undeformed and deformed state
    return bottom_start_coords, top_start_coords,
    bottom_def_coords, top_def_coords

#!!! IMPORTANT ASSUMPTION FOR THE FOLLOWING FUNCTIONS: THE ENTIRE FRAME IS BELOW (NEGATIVE Z) THE XY-PLANE, ALSO AFTER SHAPING AND LOADING
def triangulated_volume(xyz):
    #this function will always return a positive volume, whether it is above or below the xy-plane
    #the function calculates the volume between an inserted plane (xyz-coordinates) and the xy-plane
    d = scipy.spatial.Delaunay(xyz[:,:2]) #function to triangulate an array of points using Delaunay triangulation
    tri = xyz[d.vertices]

    #define two vectors (a and b) that define the triangle
    #use two vectors to calculate the cross product, which gives the projected area * 2,
    #divide by 2 to get the area of the triangle
    a = tri[:,0,:2] - tri[:,1,:2]
    b = tri[:,0,:2] - tri[:,2,:2]
```

```
43      proj_area = np.cross(a, b) / 2.0
44
45      zavg = tri[:,:,2].sum(axis=1) / 3.0 #calculates the average z value of the
        triangle vertices
46      vol = zavg * np.abs(proj_area) #multiplies the projected area with average z
        -value to get the volume
47      return np.abs(vol.sum())
48
49  def internal_volume(xyz_bottom, xyz_top):
50      #calculates the internal volume of the glass pane, by subtracting the volume
         from the top pane from the volume below the bottom pane.
51      #The "bottom pane" is the pane farthest from the xy-plane, the "top pane" is
         the one closest to the xy-plane
52      int_vol = triangulated_volume(xyz_bottom) - triangulated_volume(xyz_top)
53      return int_vol
54
55  def pressure_difference(vol_before, vol_after, pres_before):
56      #This function calculates the pressure difference due to a volume change.
57      #The pressure difference should be put on as a load on the model.
58      #Atmospheric pressure causes zero load on the model, only over- or
        underpressure causes load.
59      #pres_dif positive: new pressure is higher than previous pressure -> add
        positive (+) pressure inside the cavity
60      #pres_dif negative: new pressure is lower than previous pressure -> add
        negative (-) pressure inside the cavity
61      V1 = vol_before
62      V2 = vol_after
63      P1 = pres_before
64      #Boyle's law: P1*V1 = P2*V2, or: P1V1/P2V2 = k
65      P2 = (P1*V1)/V2
66      pres_dif = P2 - P1
67      return pres_dif, P1, P2
```

E

Insulation factor (NEN2608:2014)

As mentioned in Section 3.4, NEN 2608 (2014) prescribes a method for calculating the cavity pressure of an IGU under wind load. This method is shown here. The following input is required:

- a = shortest edge length [mm];
- b = longest edge length [mm];
- s = cavity width [mm];
- $t_{blad;1;ser}$ = thickness plane 1 [mm];
- $t_{blad;2;ser}$ = thickness plane 2 [mm];
- p = wind pressure [kN/m^2]

Note that the units do not match, because millimetres in the length inputs and metres in the pressure input are mixed. However, this is not a problem, because with the parameters in [mm], scale factors are calculated, which are then multiplied with the wind pressure p. It does not matter whether the units of the lengths and pressure match. As long as all the length inputs have the same unit, the final calculated cavity pressure will have the same unit as the wind pressure input. The procedure to calculate the cavity pressure is as follows:

$$z_1 = 181.8 \times \left(\frac{a}{b}\right)^2 \times \left(0.00406 + 0.00896 \times \left(1 - e^{\left(-1.123 \times \left(\frac{b}{a} - 1\right)^{1.097}\right)}\right)\right) \tag{E.1}$$

$$\chi = \frac{z_1}{16} \times \left(0.4198 + 0.22 \times e^{\left(-6.8 \times \left(\frac{a}{b}\right)^{1.33}\right)}\right) \times \left(\frac{b}{a}\right)^2 \tag{E.2}$$

$$a' = 28.9 \times \left(\frac{s \times t^3_{blad;1;ser} \times t^3_{blad;1;ser}}{(t^3_{blad;1;ser} + t^3_{blad;1;ser}) \times \chi}\right)^{0.25} \tag{E.3}$$

$$\phi = \frac{1}{1 + \left(\frac{a}{a'}\right)^4} \tag{E.4}$$

$$P_E = (1 - \phi) \times \frac{t^3_{blad;2;ser}}{t^3_{blad;1;ser} + t^3_{blad;2;ser}} \times p \tag{E.5}$$

Where P_E is the final cavity pressure in [kN/m^2].